8-11-2012

Molecular Dynamics Simulations of Neat Vinyl Ester and Vapor-Grown Carbon Nanofiber/Vinyl Ester Resin Composites

Changwoon Jang

Recommended Citation
Jang, Changwoon, "Molecular Dynamics Simulations of Neat Vinyl Ester and Vapor-Grown Carbon Nanofiber/Vinyl Ester Resin Composites" (2012). *Theses and Dissertations*. 3186.
https://scholarsjunction.msstate.edu/td/3186

Molecular dynamics simulations of neat vinyl ester and vapor-grown carbon nanofiber/vinyl ester resin composites

By

Changwoon Jang

A Dissertation
Submitted to the Faculty of
Mississippi State University
in Partial Fulfillment of the Requirements
for the Degree of Doctor of Philosophy
in Aerospace Engineering
in the Department of Aerospace Engineering

Mississippi State, Mississippi

August 2012

Molecular dynamics simulations of neat vinyl ester and vapor-grown
carbon nanofiber/vinyl ester resin composites

By

Changwoon Jang

Approved:

Thomas E. Lacy Associate Professor of Aerospace Engineering (Co-Director of Dissertation)	Steven R. Gwaltney Associate Professor of Chemistry (Co-Director of Dissertation)
Charles U. Pittman Jr. Professor of Chemistry (Committee Member)	Hossein Toghiani Associate Professor of Chemical Engineering (Committee Member)
Rani Warsi Sullivan Associate Professor of Aerospace Engineering (Committee Member)	J. Mark Janus Associate Professor of Aerospace Engineering (Graduate Coordinator)
Sarah A Rajala Dean of the College of Engineering	

Name: Changwoon Jang

Date of Degree: August 11, 2012

Institution: Mississippi State University

Major Field: Aerospace Engineering

Major Professor: Thomas E. Lacy

Title of Study: Molecular dynamics simulations of neat vinyl ester and vapor-grown carbon nanofiber/vinyl ester resin composites

Pages in Study: 136

Candidate for Degree of Doctor of Philosophy

Molecular dynamics (MD) simulations have been performed to investigate the system equilibrium through the atomic/molecular interactions of a liquid vinyl ester (VE) thermoset resin with the idealized surfaces of both pristine vapor-grown carbon nanofibers (VGCNFs) and oxidized VGCNFs. The VE resin has a mole ratio of styrene to bisphenol-A-diglycidyl dimethacrylate VE monomers consistent with a commercially available 33 wt% styrene VE resin (Derakane 441-400). The VGCNF-VE resin interactions may influence the distribution of the liquid VE monomers in the system and the formation of an interphase region. Such an interphase may possess a different mole ratio of VE resin monomers at the vicinity of the VGCNF surfaces compared to the rest of the system after resin curing. Bulk nano-reinforced material properties are highly dependent on the interphase features because of the high surface area to volume ratio of nano-reinforcements. For example, higher length scale micromechanical calculations suggest that the volume fraction and properties of the interphase can have a profound effect on bulk material properties. Interphase formation, microstructure, geometries, and

properties in VGCNF-reinforced polymeric composites have not been well characterized experimentally, largely due to the small size of typical nano-reinforcements and interphases. Therefore, MD simulations offer an alternative means to probe the nano-sized formation of the interphase and to determine its properties, without having to perform fine-scale experiments. A robust crosslinking algorithm for VE resin was then developed as a key element of this research. VE resins are crosslinked via free radical copolymerization account for regioselectivity and monomer reactivity ratios. After the VE crosslinked network was created, the constitutive properties of the resin were calculated. This algorithm will be used to crosslink equilibrated VE resin systems containing both pristine and oxidized VGCNFs. An understanding of formation and kinematics of a crosslinked network obtained via MD simulations can facilitate nanomaterials design and can reduce the amount of nanocomposite experiments required. VGCNF pull-out simulations will then be performed to determine the interfacial shear strength between VGCNFs and the matrix. Interphase formation, thickness and interfacial shear strength can directly feed into higher length scale micromechanical models within a global multiscale analysis framework.

DEDICATION

Dedicated to my wife and sons, Hyejin An, Hyundo Jang and Junyoung Jang.

ACKNOWLEDGEMENTS

I would like to gratefully and sincerely thank Dr. Thomas E. Lacy as a mentor and chair of the PhD advisory committee for his guidance, understanding, patience, and most importantly, his friendship during my graduate studies at Mississippi State University. For the given opportunity to develop my academic professionalism, I thank him for everything he has done for me. He encouraged me to not only grow as a senior graduate student but also as an independent thinker.

I would also like to thank Dr. Charles Jr., Pittman for his assistance and guidance in providing me a great deal of chemistry background related to my research. His detailed and objective assessments of the research have greatly advanced this works.

I would also like to thank Dr. Steven R. Gwaltney for his specific knowledge of molecular dynamics simulations. His chemical and computational backgrounds have served to improve the quality of the papers.

I would also like to thank Dr. Hossein Toghiani and Dr. Rani Warsi Sullivan for their service in my educational process and for their assistance in critiquing this work.

I would also like to thank Dr. Sasan Nouranian for sharing his expertise on polymer chemistry with me in the early stages of the MD simulations of vinyl ester resins on a pristine carbon surface. I would like to acknowledge my colleagues, Trent Ricks, Glenn Torres, and James Yu for incorporating their expertise to aid my research.

TABLE OF CONTENTS

Page

CHAPTER

LIST OF TABLES

TABLE Page

LIST OF FIGURES

CHAPTER 1

INTRODUCTION

1.1 Nano-Reinforced Polymer Composites

Composite materials are materials comprised of two or more different constituent phases (i.e., matrix and reinforcements) [Gibson 2012]. There are numorous natural composites such as wood, bones, teeth, and plant leaves, etc. The earliest man-made composites were bricks combined with straw and mud used in building construction. Now polymer nano-composite materials have been widely used in aerospace and automotive applications [Hussain *et al*., 2006] due to their enhanced material properties, light weight and extreme temperature resistance [Buryachenko *et al*., 2005; Fisher *et al*., 2002; Gates *et al*., 2005; Liu and Brinson 2006, Odegard *et al*., 2001; Odegard *et al*., 2005]. A significant enhancement in the thermal conductivity was reported in a conventional carbon fiber/phenolic resin composite mixed with highly crystalline multiwalled carbon nanotubes [Kim *et al*., 2007].

Nano-reinforced polymeric composites are an alternative to conventionally reinforced polymers. Nano-fillers or nano-reinforcements such as layered silicate, graphite nanoflakes, carbon nanotubes (CNTs), carbon nanofibers (CNFs), etc are commonly dispersed in polymer matrices. Polymer nano-composites can exhibit remarkably improved material properties since nano-reinforcements have very high surface area to volume ratios [Al-Saleh and Sundararaj 2009; Chatterjee and Isalm 2008; Eitan *et al*., 2006; Kang *et al*., 2006; Li *et al*., 2007; Luo and Daniel 2003; Sun *et al*., 2009; Zheng *et al*., 2009]. The interfacial area between the matrix and nano-reinforcement is typically an order of magnitude greater than for traditional composite materials. The nano-reinforced/polymeric material bulk properties are significantly affected by this interfacial area.

It is experimentally difficult to predict the interfacial properties, morphology, and dynamics of the interphase region between a nano-reinforcement and polymer matrix because of the atomic scale size and behavior of those constituents. Therefore, it is difficult to tailor and design nano-composite bulk properties to meet macroscale requirements. There are some available experimental techniques and computational methods, however, to assess nanoscale features of these matrials.Transmission Electron Microscopy (TEM) has been employed to suggest the existence of a nanofiller-matrix interphase region with distinct electronic densities from the bulk matrix [Lafdi *et al*., 2007]. Scanning Electron Microscopy (SEM) has been widely used to characterize nanofiber-matrix adhesion on fracture surfaces [Lafdi *et al*., 2007]. However, such techniques cannot be used to assess thermal, electrical and mechanical properties of the interfacial region, dynamic properties such as particle diffusion coefficients, or system equilibration during composite curing. Computational techniques, such as Monte Carlo (MC), and Molecular Dynamics (MD) modeling, have been employed to simulate nano-composite properties and features.

1.2 Molecular Dynamics Simulations

MD simulations may be used to describe atomic particle motions as a function of time. MD allows characterization of atomistic motions, but also short time scale dynamics ranging from femtoseconds (fs) to hundreds of nanoseconds (ns). One aim of an MD simulation is to predict macroscopic behavior resulting from microscopic interactions, which can then be used to interpret macroscale experimental results. Therefore, MD can be used to assess material behaviors occurring at lower length scales that cannot be extrapolated from experimental data.

The MD simulations can be connected to the statistical mechanics through the ergodic hypothesis. An observable macroscopic (thermodynamic) property is obtained from the ensemble average in the statistical mechanics which is equal the time average in MD simulations. There are two assumptions to satisfy ergodic hypothesis for finite MD simulations; the system is at equilibrium and the finite MD simulations are long enough to cover all of phase space.

1.2.1 MD Simulation Overview

A framework for conducting MD simulations is described below.

1. A proper model structure consisting of N particles is created.

2. A geometry optimization or energy minimization simulation is performed to adjust the coordinates of the atoms and to remove improper contacts so that the energy of the structure is brought to a stationary point.

3. A statistical ensemble, i.e., NVT, NPT, and NVE, is selected to run the dynamics simulations. Here, N is the number of atoms, V is a system volume, T is a constant

temperature, P is a constant pressure, and E is energy. During the dynamic simulations, all atom trajectories were saved in a history file.

4. When the system has reached equilibrium, post processing (data analysis) is performed.

MD simulations are carried out using specific force fields which describe the potential energy of a system of particles.

1.2.2 COMPASS Force Field (Potential Energy Functions)

The Condensed-Phase Optimized Molecular Potentials for Atomistic Simulation Studies (COMPASS) is a powerful potential energy function enabling accurate and simultaneous predictions for gas-phase and condensed-phase properties of organic and inorganic materials [Sun 1998]. The functional form of the COMPASS force field is shown below,

$$E_{total} = \sum_{b} [K_2(b-b_0)^2 + K_3(b-b_0)^3 + K_4(b-b_0)^4] + \tag{1.1}$$

$$\sum_{\theta} [H_2(\theta-\theta_0)^2 + H_3(\theta-\theta_0)^3 + H_4(\theta-\theta_0)^4] + \tag{1.2}$$

$$\sum_{\phi} [V_1(1-\cos\phi_0) + V_2(1-\cos 2\phi_0) + V_3(1-3\cos\phi_0)] + \tag{1.3}$$

$$\sum_{\chi} [K_\chi \chi^2] + \tag{1.4}$$

$$\sum_{b.b'} [F_{bb'}(b-b_0)(b'-b_0')] + \tag{1.5}$$

$$\sum_{\theta.\theta'} [F_{\theta\theta'}(\theta-\theta_0)(\theta'-\theta_0')] + \tag{1.6}$$

$$\sum_{b,\theta}[F_{b\theta}(b-b_0)(\theta'-\theta'_0)]+ \tag{1.7}$$

$$\sum_{b,\phi}[F_{b\phi}(b-b_0)[V_1\cos\phi+V_2\cos 2\phi+V_3\cos 3\phi]+ \tag{1.8}$$

$$\sum_{b',\phi}[F_{b'\phi}(b'-b'_0)[V_1\cos\phi+V_2\cos 2\phi+V_3\cos 3\phi]+ \tag{1.9}$$

$$\sum_{\theta,\phi}[F_{\theta\phi}(\theta-\theta_0)[V_1\cos\phi+V_2\cos 2\phi+V_3\cos 3\phi]+ \tag{1.10}$$

$$\sum_{\theta,\theta',\phi}K_{\theta\theta'\phi}(\theta-\theta_0)(\theta'-\theta'_0)\cos\phi+ \tag{1.11}$$

$$\sum_{i>j}\frac{q_i q_j}{\varepsilon r_{ij}}+ \tag{1.12}$$

$$\sum_{i>j}[\frac{A_{ij}}{r_{ij}^9}-\frac{B_{ij}}{r_{ij}^6}] \tag{1.13}$$

The potential function is classified by two groups containing valence energy terms (Eq. 1.1 – 1.11), including diagonal and off-diagonal cross couplings, and nonbonded interaction energy terms (Eq. 1.12 – 1.13). The first four diagonal energy terms (Eq. 1.1 – 1.4) consist of bond stretching (*b*), angle bending (θ), torsions (ϕ) (rotational motions around bonds which have rotational barriers) and out-of-plane bending (χ) coordinate terms listed in order. In these equations, *b* is the bond length, b_0 is the reference value of the bond length, θ is the bond angle, θ_0 is the reference value of the bond angle, ϕ is the torsional angle, and χ is an out-of-plane coordinate. The next seven off-diagonal energy terms (Eq. 1.5 – 1.11) indicate the cross coupling terms (bond-bond, angle-angle, bond-angle, bond-torsion, angle-torsion, etc). These cross coupling terms are dependent on the conformation changes and are used to predict vibrational frequencies and structural variations. The last two nonbonded terms (Eq. 1.12, 1.13), which include the Coulombic interaction and the van der Waals (vdW) interaction, are used for interactions between the pairs of atoms. In the vdW term, the 9th power Lennard-Jones (LJ-9-6) function is used in the repulsion region instead of the common LJ-12-9 function. The force field parameters are derived from using *ab initio* quantum mechanics calculations, such as density functional theory (DFT) which are more direct than empirical methods [Maple *et al.*, 1998]. The system dependent parameters (K, H, V, F) calculated by DFT are validated by experimental data from gas-phase measurements (electron diffraction) with a set of models. The parameters were also validated using MD simulations with most organic and inorganic materials [Sun, 1998].

1.2.3 Statistical Ensembles

In MD simulations, microcanonical (NVE), canonical (NVT), and isothermal-isobaric (NPT) statistical ensembles should be used to establish boundary conditions for the molecular system [Frenkel and Smit 2002]. The system in an NVE simulation is isolated from changes in the number of particles (N), system volume (V), and energy (E). An NVE ensemble is obtained by solving Newton's 2nd law without any temperature and pressure control. The total energy is conserved, but energy fluctuations and drift exist because of rounding and truncation errors during the integration process. In NVT simulations, the number of particles (N), system volume (V) and temperature (T) are held fixed by controlling the temperature. In NPT simulations, the number of particles (N), pressure (P) and temperature (T) are conserved. NPT allows control over both the temperature and pressure.

1.2.4 Limitations of Molecular Dynamics Simulations

Some limitations associated with MD simulations are summarized as follows: 1) The *motion of atoms* in MD is described by only *classical* mechanics. MD simulations are based on solving *classical Newton's* equation of motion for *N* interacting atoms in a system,

$$m_i \frac{\partial^2 r_i}{\partial t^2} = F_i, \quad i = 1 \ldots N \tag{1.14}$$

The force is determined by taking the partial derivatives of a potential energy function $V(r_1, r_2, \ldots, r_N)$ with respect to the associated generalized displacement, r_i,

$$F_i = -\frac{\partial}{\partial r_i} V(r_1, r_2 \ldots, r_N) \tag{1.15}$$

In principle, quantum mechanics accurately describes the properties of molecular systems, but solving the Schrödinger equation of a complex system is computationally expensive. 2) *Force fields* (potential energy functions) are approximate. The force fields are empirically parameterized based on quantum calculations and experimental observations. 3) The *atomic charges* are *not* changed by environment. 4) *Lennard-Jones* interactions (non-bonded interactions) are *truncated* by using cutoff distances. 5) *Periodic Boundary conditions* must be used.

1.3 Motivation and Objectives

The formation and properties of interphase regions of the matrix between bulk matrix and reinforcement surfaces is an area where little is known. We postulated that MD simulations might provide an approach to this topic. First, when a liquid resin containing different monomers contacts a reinforcement surface, such as the surface of a carbon nanofiber, the molar composition near the surface could be different than that of the bulk. Work was underway preparing vinyl ester/VGCNF composites using the commercial vinyl ester, Derakane 441-400, as part of Sasan Nouranian's PhD dissertation research [Nouranian, 2011; cf. Chapter 5]. He provided the molecular structure of this resin and proposed the use of three specific monomers to use to perform MD modeling of Derakane 441-400 in the presence of VGCNF surfaces. This liquid monomer composition was equilibrated at graphene surfaces to give the monomer distributions versus distances from those surfaces. This, in turn, was used later as the basis for interphase formation. The early work was discussed with Dr. Sasan Nouranian based on his expertise in polymer chemistry.

Establishment of structure-property relationships for polymers, polymer composites, and polymer nano-composites, which account for relevant irreversible processes manifested at fundamentally different spatial and temporal scales, is increasingly becoming a focal point in materials modeling and simulation efforts [Lacy 2011]. Development of a coherent integrated multiscale analysis framework is crucial for determining the effect of microstructural features in polymers and nanoscale reinforcements in polymer nano-composites on micro-, meso-, and macroscale material behavior. This is particularly true when describing lower length scale phenomena not amenable to direct observation or physical measurements. The efficient transfer of scale-specific model data in computations performed at successively higher or lower length scales is one key challenge in multiscale composites modeling. Specification and validation of an appropriate "handshake" protocol linking calculations performed at disparate spatial and temporal scales has posed a serious obstacle in multiscale material model development for polymer nano-composites. These difficulties are mainly due to the complex nature of these materials and poor knowledge about the key mechanisms influencing the material behavior at different time and length scales. Establishment of a robust multiscale framework for polymer composite design and analysis requires seamless integration between high fidelity scale-specific models [Lacy, 2011].

The main goals of this MD project are 1) to understand the Derakane 441-400 epoxy vinyl ester resin [Ashland Chemical Co. 2011] monomer interactions (prior to curing) with both pristine VGCNFs and oxidized VGCNFs, 2) to determine the monomer ratios in the crosslinked network near the VGCNFs surfaces after curing and 3) to develop a new crosslinking algorithm accounting for regioselectivity (head-to-tail chain propagation) and relative reactivity ratios. Finally, this algorithm will be employed to cure VE and then properties of the cured resin will be producted. MD simulations of 33 wt% styrene VE resin nano-composite systems were performed with pristine VGCNFs. This work is distinct from other MD simulations in that a relatively large system containing 17,055 atoms with a relatively large simulation time (~13 ns). The interactions of the different liquid resin monomers with the nanofiber surface plus monomer-monomer interactions compete with all monomer-monomer solution interactions when monomers are not near the surface. This leads to an equilibrium arrangement of the molecules in the system, which determines the gradients in the final monomer distributions in the vicinity of the nanofiber surface. Other similar simulations were performed where the surface is a model oxidized VGCNFs to assess the liquid monomer distribution for comparison to pristine VGCNFs.

Other simulations were performed to assess the neat crosslinked VE properties. Understanding micro-structures and properties of neat crosslinked VE is critical for assessing pristine or oxidized VGCNF/VE systems. The VE curing reaction using MD used key aspects of free radical copolymerization to include the correct (head-to-tail) regioselectivity, determination of the appropriate reaction distances, account for the monomer relative reactivity ratios, and growing radical site concentrations. These criteria were integrated into an algorithm that crosslinks the system in a manner similar to the real VE resin curing process. Although several crosslinking algorithms have been proposed for epoxy resins [Varshney *et al*., 2008; Wu and Xu 2006; Frankland *et al*., 2003; Lin and Khare 2009], no such algorithm exists curing via free radical chain polymerization of different monomers. Thus, VE resins cure, so including the realistic chemistry for the VE crosslinking reaction using MD is a key contribution of this work.

Once the method for crosslinking neat VE resin is developed, it will be applied to VGCNF/VE systems. After creating the VGCNF/VE cured micro-structures, the effective interphase, interface, and other properties of interest can be determined using MD VGCNFs pullout simulations similar to those performed using CNTs [Gou *et al*., 2004]. MD-based estimates for composite interphase properties and interfacial shear strengths may be validated using novel experimental results from the literature [Manoharan *et al*., 2009; Ozkan *et al*., 2010]. Calculated interphase formation, thickness and interfacial shear strength data can directly feed into higher length scale micromechanical models within a global multiscale analysis framework.

1.4 References

Ashland Chemical Co., “Derakane 441-400 Vinyl Ester Resin Property Data Sheet.” http://www.ashland.com, 2011.

Al-Saleh, M. H., and Sundararaj, U., “A Review of Vapor Grown Carbon Nanofiber/Polymer Conductive Composites,” *Carbon*, 47, 2009, 2-22.

Buryachenko, V. A., Roy, A., Lafdi, K., Anderson , K. L., and Chellapilla, S., “Multi-Scale Mechanics of Nanocomposites Including Interface: Experimental and Numerical Investigation,” *Composites Science and Technology*, 65, 2005, 2435-2465.

Chatterjee, A., and Islam, M. S., “Fabrication and Characterization of TiO_2-Epoxy Nanocomposite,” *Material Science and Engineering A*, 487, 2008, 574-585.

Eitan, A., Fisher, F. T., Andrews, R., Brinson, L. C., and Schadler, L. S., “Reinforcement Mechanisms in MWCNT-filler Polycarbonate,” *Composite Science and Technology*, 66, 2006, 1159-1170.

Fisher, T. T., Nanomechanics and the Viscoelastic Behavior of Carbon Nanotube-Reinforce Polymers, Thesis of Mechanical Engineering, PhD thesis, 2002, Northwestern University.

Frenkel, D., and Smit B., “Unerstanding Molecular Simulation from Algorithms to Applications,” 2nd Ed., Academic Press, 2002, 139-163.

Gates, T. S., Odegard, G. M., Frankland, S. J. V., and Clancy, T. C., “Computational Materials: Multi-Scale Modeling and Simulation of Nanostructured Materials,” *Composites Science and Technology*, 65, 2005, 2416-2434.

Gibson, R. F., “Principles of Composite Material Mechanics,” 3rd Ed., Taylor & Francis, 2012, 1-40.

Hussain, F., hojjati, M., Okamoto, M., and Gorga, R. F., “Review Article: Polymer-Matrix Nanocomposites, Processing, Manufacturing, and Application: An Overview,” *Journal of Composite Materials*, 40(17), 2006, 1511-1575.

Kang, I., Heung, Y. Y., Kim, J. H., Lee, J. W., Gollapudi, R., Subramaniam, S., Narasimgadevara, S., Hurd, D., Kirikera, G. R., Shanov, V., Schulz, M. J., Shi, D., Boerio, J., Ma, S., and Ruggles-Wre, M., “Introduction to Carbon Nanotubes and Nanofiber Smart Materials,” *Composite: Part B*, 37, 2006, 382-394.

Kim, Y. A., Kamio, S., Tajiri, T., Hayashi, T., Song, S. M., Endo, M., Terrones, M., and Dresshlhaus, M. S., "Enhanced Thermal Conductivity of Carbon fiber/Phenolic Resin Composites by the Introduction of Carbon Nanotubes," *Applied Physics Letters*, 90, 2007, 093125-093137.

Lacy, T. E., Gwaltney, S. R., Toghiani, H., Jang. C., Nouranian, S., and Yu, J., "Some Key Issues in Multi-Scale Modeling of Thermoset Nanocomposites/Composites," In S. M. Arnold, T. Wong (Eds), "Tools, Models, Databases, and Simulation Tools Developed and Needed to Realize the Vision of Integrated Computational Materials Engineering," Materials Park, OH: ASM International.

Lafdi, K., Fox, W., Matzek, M., and Yildiz, E., "Effect of Carbon Nanofiber-Matrix Adhesion on Polymeric Nanocomposite Properties-Part II," *Journal of Nanomaterials*, 2008, doi:10.1155/2008/310126.

Li, J., Vaisman, L., Marom, G., and Kim, J., "Br Treated Graphite Nanoplatelets for Improved Electrical Conductivity of Polymer Composites," *Carbon*, 45, 2007, 744-750.

Lin, P.-H., and Khare, R., "Molecular Simulation of Cross-linked Epoxy and Epoxy-POSS Nanocomposite", *Macromolecules*, 42(12), 2009, 4319-4327.

Liu, H., and Brinson, L. C., "A Hybrid Numerical-Analytical Method for Modeling the Viscoelastic Properties of Polymer Nanocomposites." *Journal of Applied Mechanics*, 73, 2006, pp. 758-768.

Luo, J. J., and Daniel, I. M., "Characterization and Modeling of Mechanical Behavior of Polymer/clay Nanocomposites," *Composites Science and Technology*, 63(11), 2003, 1607-1616.

Maple, J. R., Dinur, U., Hagler, A. T. "Derivation of force fields for molecular mechanics and dynamics from ab initio energy surfaces," *Proceedings of the National Academy Sciences*, 1998;85,5350.

Manoharan, M. P., Sharma, A. V., Haque, M. A., Bakis, C. E., and Wang, K. W., "The Interfacial Strength of Carbon Nanofiber Epoxy Composite using Single Fiber Pullout Experiments," *Nanotechnolgy*, 20, 2009, 1-5.

Nouranian, S., "Vapor-grown carbon nanofiber/vinyl ester nanocomposites: Designed experimental study of mechanical properties and molecular dynamics simulations," Starkville MS USA, Mississippi State University, PhD dissertation, 2011.

Odegard, G.M., Gates, T. S., Nicholson, L. M., and Wise, K. E., "Equivalent-Continuum Modeling of Nano-structured Materials," NASA/TM 210863, 2001, 1-30.

Odegard, G. M., Clancy, T. C., and Gates, T. S., “Modeling of the Mechanical Properties of Nanoparticle/Polymer Composites,” *Polymer*, 46, 2005, 553-562.

Ozkan, T., Naraghi, M., and Chasiotis, I., “Mechanical Properties of Composite Materials,” Carbon, 48, 2012, 239-244.

Sun H. “COMPASS: An ab initio force-field optimized for condensed-phase applications: overview with details on alkane and benzene compounds., *The Journal of Physical Chemistry B*, 1998, 102(38), 7338-7364.

Sun, L., Gibson, R. F., Gordaninejad, F., and Suhr, J., “Energy Absorption Capability of Nanocomposites: A Review,” *Composite Science and Technology*, 69, 2009, 2392-2409.

Varshney, V., Patnaik, S. S., Roy, A. K., and Farmer, B. L., “A molecular dynamics study of epoxy-based networks: Cross-linking procedure and prediction of molecular and material properties”, *Macromolecules*, 2008, 41, 6837-6842.

Zheng, C., Fan, Z., Wei, T., and Luo, G., “Temperature Dependence of the Conductivity Behavior of Graphite Nanoplatelets-filled Epoxy Resin Composites,” *Journal of Applied Polymer Science*, 2009, 113, 1515-1519.

CHAPTER 2

MOLECULAR DYNAMICS SIMULATIONS OF VINYL ESTER RESIN MONOMER INTERACTIONS WITH A PRISTINE VAPOR-GROWN CARBON NANOFIBER AND THEIR IMPLICATIONS FOR COMPOSITE INTERPHASE FORMATION

2.1 Abstract

A molecular dynamics simulation study was performed to investigate the role of liquid vinyl ester (VE) resin monomer interactions with the surface of pristine vapor-grown carbon nanofibers (VGCNFs). These interactions may influence the formation of an interphase region during resin curing. A liquid resin having a mole ratio of styrene to bisphenol-A-diglycidyl dimethacrylate VE monomers consistent with a commercially available 33 wt% styrene VE resin was placed in contact with both sides of two pristine graphene sheets overlapped like shingles to represent the outer surface of a pristine VGCNF. The relative monomer concentrations were calculated in a direction away from the graphene sheets. At equilibrium, the styrene/VE monomer ratio was higher in a 5 Å thick region adjacent to the nanofiber surface than in the remaining liquid volume. The elevated concentration of styrene near the nanofiber surface suggests that a styrene-rich interphase region, with a lower crosslink density than the bulk matrix, could be formed upon curing. Furthermore, styrene accumulation in the immediate vicinity of the nanofiber surface might, after curing, improve the nanofiber-matrix interfacial adhesion

compared to the case where the monomers were uniformly distributed throughout the matrix.

2.2 Introduction

Carbon is the element at the heart of organic chemistry, while also central to an array of remarkable materials including diamond [Bruchell 1999], fullerenes [Bruchell 1999, Kroto *et al*., 1985], graphite [Burchell 1999], graphene [Novoselov *et al*., 2004], nanotubes [Burchell 1999, Iijima 1991], continuous and chopped carbon fibers [Donnet *et al*., 1998, Peebles 1995, Yosomiya *et al*., 1985] and carbon nanofibers [Burchell 1999, Endo *et al*., 2001, Tibbetts *et al*., 2007]. Carbon fibers [Donnet *et al*., 1998, Peebles 1995] used to fabricate composites with exceptional specific properties are comprised of graphite, which consists of regularly stacked sequences of graphene. Recently, vapor-grown carbon nanofibers (VGCNFs) [Burchell 1999, Tibbetts *et al*., 2007] and carbon nanotubes have become a further focus for reinforcing composites. However, in order to successfully mate carbon reinforcements with matrix materials to achieve high performance composites, the carbon surfaces must be made compatible with these matrices. Pristine carbon surfaces of all types do not adhere strongly to typical organic polymer matrices [Tang and Kardos 1997]. This paper investigates what might happen when the pristine surface of a VGCNF encounters a typical liquid vinyl ester (VE) resin prior to curing. Interface structure and adhesive strength are seminal issues always encountered when using carbon materials as reinforcements in composites [Yosomiya *et al*., 1989].

VGCNFs are commercial nanoreinforcements, which have been studied in thermoplastic and thermosetting polymer matrices [Tibbetts *et al*., 2007]. The micro- and nano-scale interactions between nanofibers and polymer molecules at the interface can result in an “interphase” region [Jancar 2009], i.e., a third distinct phase surrounding each nanofiber with different properties than those of the bulk polymer [Jancar 2008, Vaia and Giannelis 2001]. The nature of nanofiber-polymer molecular interactions in both thermoplastics and thermosetting matrices can be either attractive or repulsive, depending primarily on the chemistry of the matrix material and nanoreinforcement and the arrangement of molecules in the proximity of the interface at the molecular scale.

The immobilization of chain segments of thermoplastic polymers on the nanofiber surface due to attractive carbon surface-polymer interactions can affect the shape, direction, and morphology of crystalline lamellae that make up the interphase [Jancar 2008, Qiao and Brinson 2009]. In general, retarded or accelerated polymer chain motions, as defined by the local nanofiber-polymer interactions, lead to different levels of crystallinity, chain entanglement density, charge distribution, free volume, and other physical and mechanical properties. The properties can be markedly different from the bulk polymer [Qiao and Brinson 2009, Schadler *et al*., 2007]. Interphase formation is both material and temperature dependent, resulting in interphase regions of different thicknesses.

Although a basic understanding exists regarding interphase creation mechanisms in thermoplastics, far less is known about the interphase region in thermosets. The interactions between liquid monomers of thermosetting resins and nanofiber surfaces, prior to crosslinking, could lead to different interfacial mole ratios of these monomers compared to those of the bulk resin. After curing, the resulting crosslinked network may therefore have a different crosslink structure in the interphase region. Hence, gradients in mechanical properties may develop [Schadler *et al*., 2007].

Interphase structure and properties should be considered when developing realistic mechanical models of nanoreinforced composites [Montazeri and Naghdabadi 2010]. Moreover, given the high surface area to volume ratio of nanoreinforcements, the interphase volume fraction may be significant compared to that of the nanoreinforcements.

Experimental studies of interphase formation in nanoreinforced composites is very difficult, so molecular dynamics (MD) simulations offer an alternative means to probe interphase formation and properties. Many interfacial MD studies have been published for clay [Sikdar *et al*., 2006, Sikdar *et al*., 2008], silica [Baller *et al*., 2009], and carbon nanotube [Chowdhury and Okabe 2007, Coleman *et al*., 2006, Frankland *et al*., 2002, Gou *et al*., 2004, Gou *et al*., 2005, Liao and Li 2001, Putz *et al*., 2007] composites, but reports of similar efforts for VGCNF systems are scarce. Gou *et al*., [Gou *et al*., 2007] studied interactions between a single epoxy bisphenol-A type molecule and either pristine or functionalized (nitric acid oxidized) VGCNFs using MD simulations. An increased tendency for the aromatic ring of the epoxy molecule to align on the surface of the pristine VGCNF was found in comparison to functionalized VGCNFs. However, Gou *et al*.,'s simulations had only a single resin molecule in a vacuum interacting with the nanofiber surface. Totally overlooked was the seminal importance of epoxy molecules interacting in the liquid phase with other monomers and how this competes with the interactions at the nanofiber surface. Furthermore, Gou *et al*., simulated a nanofiber with an unrealistically small diameter [Gou *et al*., 2007]. Thus, the basal plane of the outer graphene sheet was curved and severely strained. It did not resemble real VGCNFs with far larger diameters (70-200 nm)[a]. One must clearly distinguish between a small diameter, tightly curved single-walled carbon nanotube and a comparatively large diameter VGCNF.

VE resins are used in many composites [Harper 2002, McConnell 2010]. These resins are less expensive than epoxies and possess good mechanical properties. When formulated with radical initiators, they can be infused as low viscosity resins into fiber or other reinforcing preforms at ambient conditions and then cured. The co-monomer styrene is usually employed to lower viscosity. Styrene copolymerizes with the VE monomers, acting as an extender between dimethacrylate monomers based on the diglycidyl ether of bisphenol-A [Cook *et al*., 1997]. The formation and characteristics of an interphase in VGCNF/VE composites and mechanisms leading to its creation are not understood. They have never been studied using MD simulations. However, the interphase formation in both unsized and sized long carbon fibers with oxidized surface functions (AS4 fibers) in VE resins has been experimentally studied by Xu [Xu 2010].

The main contribution of the present work is to provide an understanding of the VE liquid resin monomer interactions (prior to curing) with a pristine VGCNF during processing. MD simulations of a 33 wt% styrene VE resin composite system, containing

---

[a] Pyrograf Products (an Affiliate of Applied Sciences, Inc.) http://pyrografproducts.com/Merchant5/merchant.mvc?Screen=cp_nanofiber (date accessed: January 12, 2011).

the correct resin monomer mole ratios, were performed. Unique to this work is the simulation of a relatively large system containing 17,055 atoms with a large number of time steps (total simulation time of ~ 13 ns). The concentrations of the three monomers in the proximity of the nanofiber surface differed from the bulk resin, suggesting that the creation of an interphase region during resin crosslinking could occur.

2.3 Molecular Models

2.3.1 Models of Vinyl Ester Monomers

The vinyl ester resin used in the simulation was commercially available Derakane 441-400 epoxy vinyl ester resin [Ashland Chemical Co. 2011]. This resin was previously used in an experimental study on the dynamic mechanical properties of VGCNF/VE composites [Nouranian *et al*., 2010]. It is a mixture of VE dimethacrylates with an average molecular weight of 690 g/mol [Li 1998] and also contains 33 wt% styrene. Derakane 441-400 has an average of 1.62 bisphenol-A groups ($n = 1.62$, where n is the number of bisphenol-A groups) in the dimethacrylate backbone [Li 1998]. Figure 2.1 shows the general chemical formula of the VE dimethacrylate and the models created for $n = 1$ and $n = 2$. For simplicity, these two dimethacrylate monomers are designated VE1 and VE2 corresponding to $n = 1$ and $n = 2$, respectively.

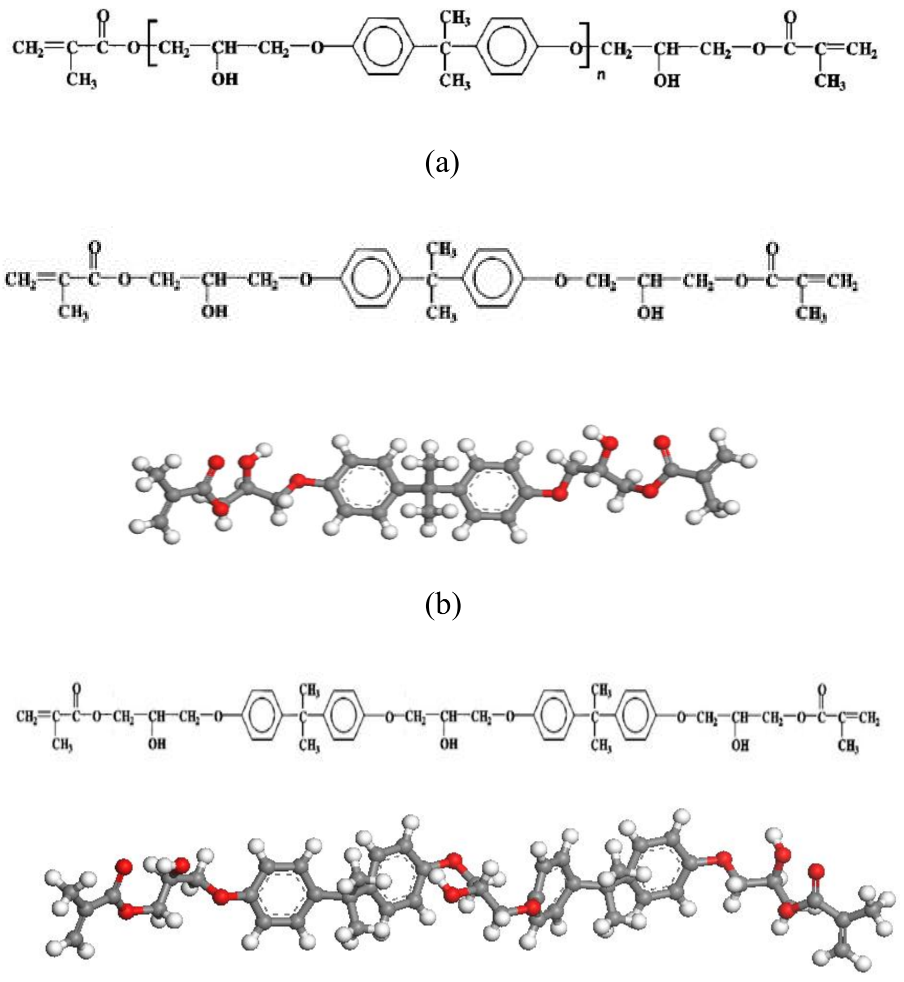

(a)

(b)

(c)

Figure 2.1 Bisphenol-A-based dimethacrylate monomers of the vinyl ester resin: (a) General formula ($n = 1.62$ for Derakane 441-400). (b) Chemical formula and model created for $n = 1$. (c) Chemical formula and model created for $n = 2$.

A mixture of VE1 and VE2 was used in the simulations at a VE1/VE2 mole ratio of 37/61. This corresponds to the average value of $n = 1.62$ present in Derakane 441-400. The chemical formula and model for styrene are shown in Figure 2.2.

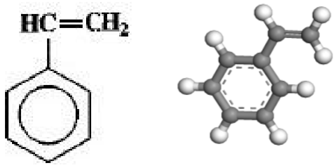

Figure 2.2 Chemical structure and the model created for styrene.

2.3.2 Model of the Carbon Nanofiber Surface

VGCNFs typically have a stacked-cone (Dixie cup) structure (Figures 2.3a and 2.3b) [Maruyama and Alam 2002]. In this work, the surface of a VGCNF was idealized using two overlapping flat graphene sheets stacked on top of each other in a shingled form to resemble the overlapping region of stacked nanocones along the outer surface of a VGCNF. This structure is shown in Figure 2.3c. The nanocone structure used previously by Gou *et al.*, [Gou *et al.*, 2007] was avoided because it employed an artificially small radius leading to a highly curved π-electron structure. This would distort its interaction with the three monomers. The VGCNF diameters range from 70 to 200 nm (700-2000 Å), which are large in comparison with typical MD simulation cell dimensions (~ 125-350 nm^3). The simulation cell used in this work was 60×50×60 $Å^3$ (180 nm^3) in size. Hence, the surface of a VGCNF, which appears essentially flat at the scale of a styrene or vinyl ester molecule, can be approximated using graphene sheets. This is clearly illustrated in Figure 2.3c for a 6 nm wide section on a nanofiber cone's surface.

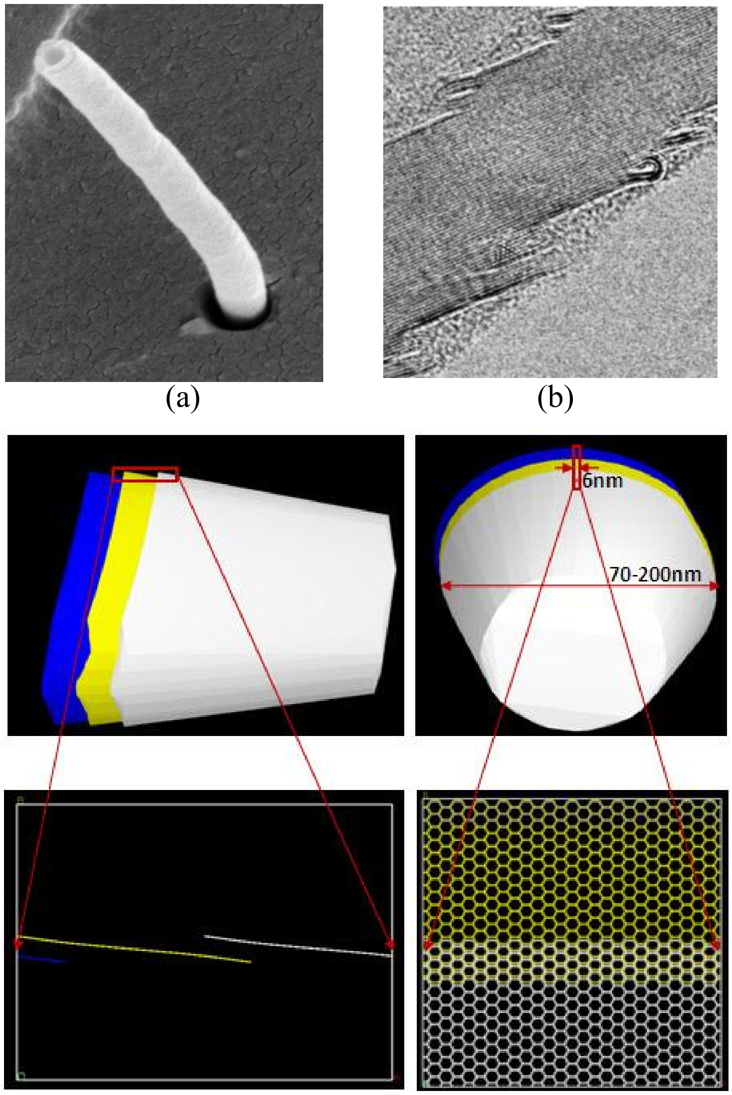

(a) (b)

(c)

Figure 2.3 (a) View of a single carbon nanofiber. (b) Cross section of the stacked nanocone structure of VGCNF with shingled graphene sheets (adapted from [Uchida *et al*., 2006]). (c) A schematic of overlapping graphene sheets along the outer edge of VGCNF stacked nanocones.

2.4 MD Simulation Details

2.4.1 The MD simulation Cell

All simulations were performed using Accelrys® Materials Studio® V5.0 software. A cell of size 60×50×60 $Å^3$ was created and two parallel graphene sheets were stacked in the middle of the simulation cell to form a shingle. Shingling is necessary if the stacked-cone VGCNF morphology is to be simulated. The distance between the cone edges (represented as the edge plane where the overlap takes place) varies somewhat in real VGCNFs based on high-resolution transmission electron microscopy (TEM) studies [Uchida *et al*., 2006]. The model employed in the present work represents the case where a cone edge is encountered once every 30 Å along the nanofiber. This is an estimate from the TEM examinations [Uchida *et al*., 2006]. Furthermore, the shingled structure better represents real VGCNFs because it exposes the liquid monomers to both edges and basal graphitic planes.

The sheets are roughly perpendicular to the y-direction or (0 1 0) plane and parallel to the x- (1 0 0) and z-directions (0 0 1) (Figure 2.4). 3D periodic boundary conditions were used. The sheets have an inter-planar spacing of 3.5 Å, which is close to the value of 3.4 Å reported by Zhu *et al*., [Zhu *et al*., 2005] for fishbone-type carbon nanofibers. The sheets have a slight angle relative to the basal (xz) plane of the cell to allow for a shingled graphene sheet structure to be constructed in the x-direction (Figure 2.4). The distance between the shingle steps is about 30 Å. In a real carbon nanofiber, the typical distance between the shingle steps is about 10-20 nm [Uchida *et al*., 2006]. To prevent distortion and separation of the graphene sheets and their inter-planar distances during dynamics simulations, their atomic coordinates were fixed. This is justified because multiple layers of rigid stacked cones in real VGCNFs prevent graphene sheet distortions.

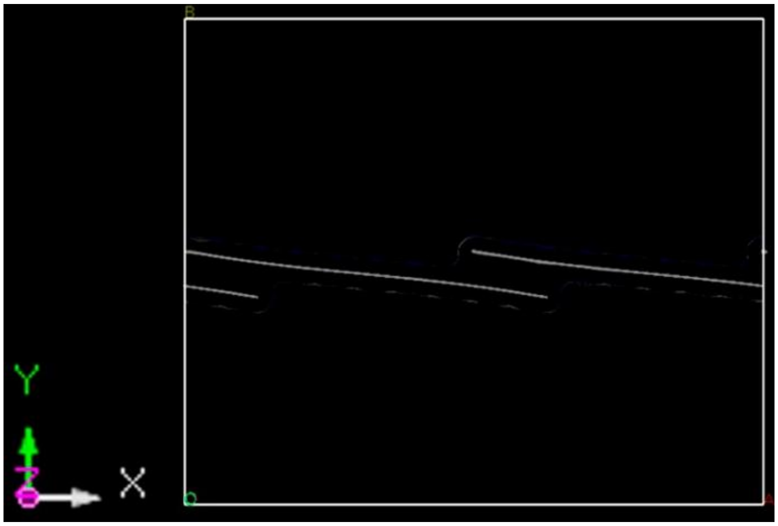

Figure 2.4 View of stacked (periodic) graphene sheets resembling the surface of carbon nanofiber.

VE resin monomers (VE1, VE2, and styrene) were initially randomly packed around the graphene sheets using the iso-surface feature in the Amorphous Cell® module of Materials Studio® to yield a final simulation cell density of 1.18 g/cm^3 (Figure 2.5). This density value was previously measured experimentally, as part of this study, for a cured VGCNF/VE composite with 1 wt% VGCNFs. The iso-surface was removed after monomer packing to permit monomer-nanofiber surface interactions. The total number of monomer molecules used and their weight fractions are given in Table 2.1.

Table 2.1 Total number and weight fractions of vinyl ester resin monomers

Resin monomer[a]	Number of molecules	Mass (u)	Weight %
VE1[b]	37	512.599	18.8
VE2[c]	61	796.954	48.2
Styrene	320	104.152	33.0

[a] Vinyl ester resin (Derakane 441-400) with n = 1.62 (n is the number of bisphenol-A groups in the dimethacrylate's backbone).
[b] The dimethacrylate with n = 1.
[c] The dimethacrylate with n = 2.

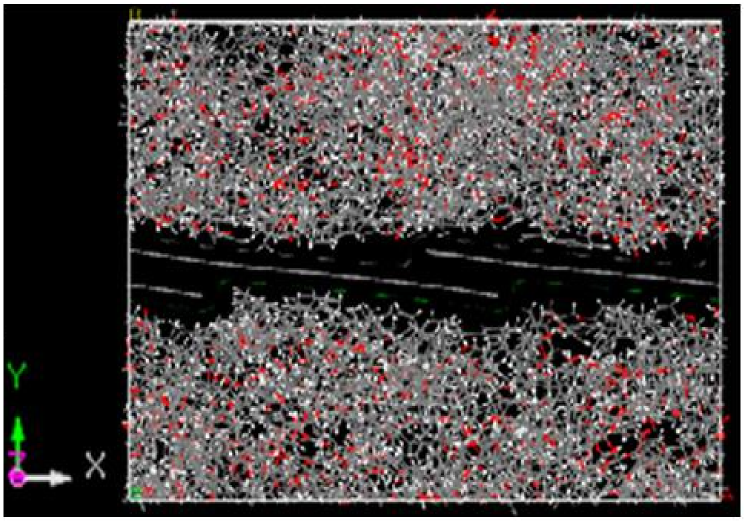

Figure 2.5 The periodic simulation cell packed with resin monomers.

2.4.2 Dynamics Simulations

The Condensed-Phase Optimized Molecular Potentials for Atomistic Simulation Studies (COMPASS) force field developed by Sun [Sun 1998] was used for this study. This force field is widely used for organic and inorganic systems. A geometry optimization was carried out for 10,000 iterations using the conjugate gradient method to partially relax the molecular structures and minimize the total energy of the system. Then the MD simulation was started using an NVT ensemble (constant number of atoms, N; constant volume, V; and constant temperature, T) at 10 K with a time step of 0.5 fs. An NVT ensemble was selected here for technical reasons. Since position constraints were placed on the graphene sheets, the box scaling which occurs during constant pressure (NPT) simulations would have led to unrealistic distortions of the sheets.

The simulation was run for 1 ps at 10 K. Then the temperature was increased to 50 K and then further up to 600 K in increments of 50 K. At each intermediate temperature, the dynamics simulation was run for 1 ps, except at 300 K where it was run for 100 ps. At 600 K, the simulation was run for a total time of 4 ns with a time step of 0.5 fs.

Next, the temperature was increased to 1000 K using 50 K increments and 1 ps dynamics simulation runs at intermediate temperatures. The dynamics simulations were run to obtain equilibrium monomer distributions in the simulation cell. This was achieved through successive simulations at elevated temperatures. It was found that high simulation temperatures were required to reach equilibrium monomer distributions within a reasonable simulation time. Since equilibrium was not achieved at 600 K, the temperature was further increased to 1000 K.

The system was then cooled to 300 K in two different ways: 1) 10 K decrements (designated as C1), and 2) 50 K decrements (C2), both with 1 ps dynamics simulation runs at intermediate temperatures. After cooling, the dynamics simulation was continued for 5 ns at 300 K to ensure system equilibration. A summary of the simulation parameters is given in Table 2.2. In Figure 2.6, two snapshots of the simulation are shown: one after the geometry optimization step and the other after running the simulation for a total simulation time of ~ 13 ns (following cooling procedure C1). Complete wetting of the graphene surface by monomers at the end of the simulations can be seen in contrast to the initial randomly packed structure. The closest distance between atoms on opposite sides of the graphene sheets is ~7 Å (Figure 2.6). Since this distance is a bit shorter than the cut off distance for van der Waals interactions (9.5 Å), some cross sheet interactions may occur between monomers near opposite surfaces of the sheets, which are unphysical. Any potential effects of these interactions will be studied in future work.

Table 2.2 Summary of the molecular dynamics simulation parameters

Total number of atoms	17055
Ensemble	NVT
Thermostat (temperature control)	Anderson
van der Waals (vdW) cutoff distance	9.5Å

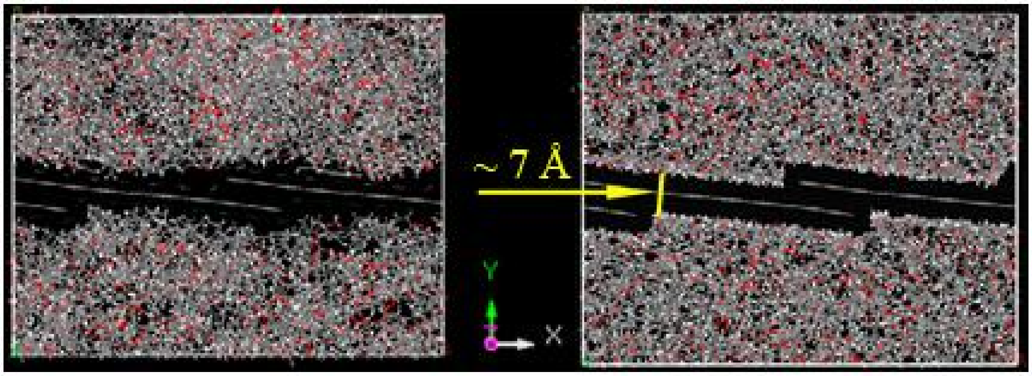

Figure 2.6 Snapshots of the initial frame after geometry optimization (left) and final frame after dynamics simulation (right) for a total simulation time of ~ 13 ns (following cooling procedure C1).

2.5 Results and Discussion

To analyze the distribution of liquid resin monomers at the nanofiber-resin interface and in the direction roughly perpendicular to the graphene sheets, concentration profiles were generated for different monomers in the y-direction (Figures 2.4 and 2.5), or perpendicular to the (0 1 0) plane, using the Forcite® analysis tool of Materials Studio®. The concentration profile is the relative concentration of a given monomer as a function of the distance from the origin of the simulation cell (here in the y-direction). It is generated for 3D periodic structures by determining the density of atoms or a set of atoms comprising a molecule within evenly spaced slabs (subvolumes) parallel to the axes of the simulation cell or any other direction of choice.

The dimensionless relative concentration (C) of a specific monomer's atoms contained in a given slab in the liquid resin is defined as:

(2.1)

where N_{slab} is the number of monomer atoms in the slab, V_{slab} is the slab volume, N_{tot} is volume in the simulation cell.[b] A relative concentration of 1.0 within any liquid resin volume region of the cell (e.g., a slab) means that the ratio of the three monomers in that slab is the same as the average ratio throughout the liquid resin (e.g., the original mole ratio of the three monomers at the experimental density). A value of 2.0 indicates that twice the number of atoms from a specific monomer is in that slab compared to the case where all the monomers are distributed homogeneously across the liquid resin volume. In this study, the simulation cell was divided into 50 slabs (1 Å thick) parallel to the xz-plane, and the monomer concentration profiles were generated for each of the three monomer molecules.

The interactions of each of these three resin monomers with the nanofiber surface and other neighboring monomers are different than the monomer-monomer interactions in regions removed from the surface. The initial randomly located monomers will try to reach a minimum energy, imparting a diffusion-controlled process, which moves towards equilibrium. A state of equilibrium must be reached before post-processing of the acquired data. A definition of equilibrium in MD simulations should be established, since unfeasibly long simulation times may be needed to reach true equilibrium. The time-averaged monomer concentration profiles at 1000 K were used in this study as the basis for checking the equilibrium status of the system and determining when to start the cooling process. The relative monomer concentrations were determined every 50 ps and then time-averaged over each successive 1 and 2 ns intervals for the total simulation time of 4 ns performed at 1000 K.

---

[b] Materials Studio® User's Manual, Accelrys, Inc., San Diego, CA.

Some time-averaged concentration profiles for styrene are shown in Figure 2.7. The domain, 22 Å < y < 25 Å, denotes the vertical distance between the edges of the overlapping graphene sheets in the simulation cell, where the relative concentration goes to zero. Similar concentration profiles were generated for VE1 and VE2 and these are presented in the appendix A (Figures 2.A.1 and 2.A.2). The spatial and temporal evolutions of the concentration profiles were monitored, and the profiles were compared with each other to ensure that a suitable equilibrium had been reached before cooling the system to 300 K. Comparing the different time-averaged concentration profiles in Figure 2.7 reveals that there is consistency in the successive time-averaged profiles. Therefore, it was concluded that the system approached equilibrium at 1000 K after about 4 ns of simulation. So, a simulation time of 4 ns at 600 K and another 4 ns at 1000 K ensured that the monomers have equilibrated before cooling the system.

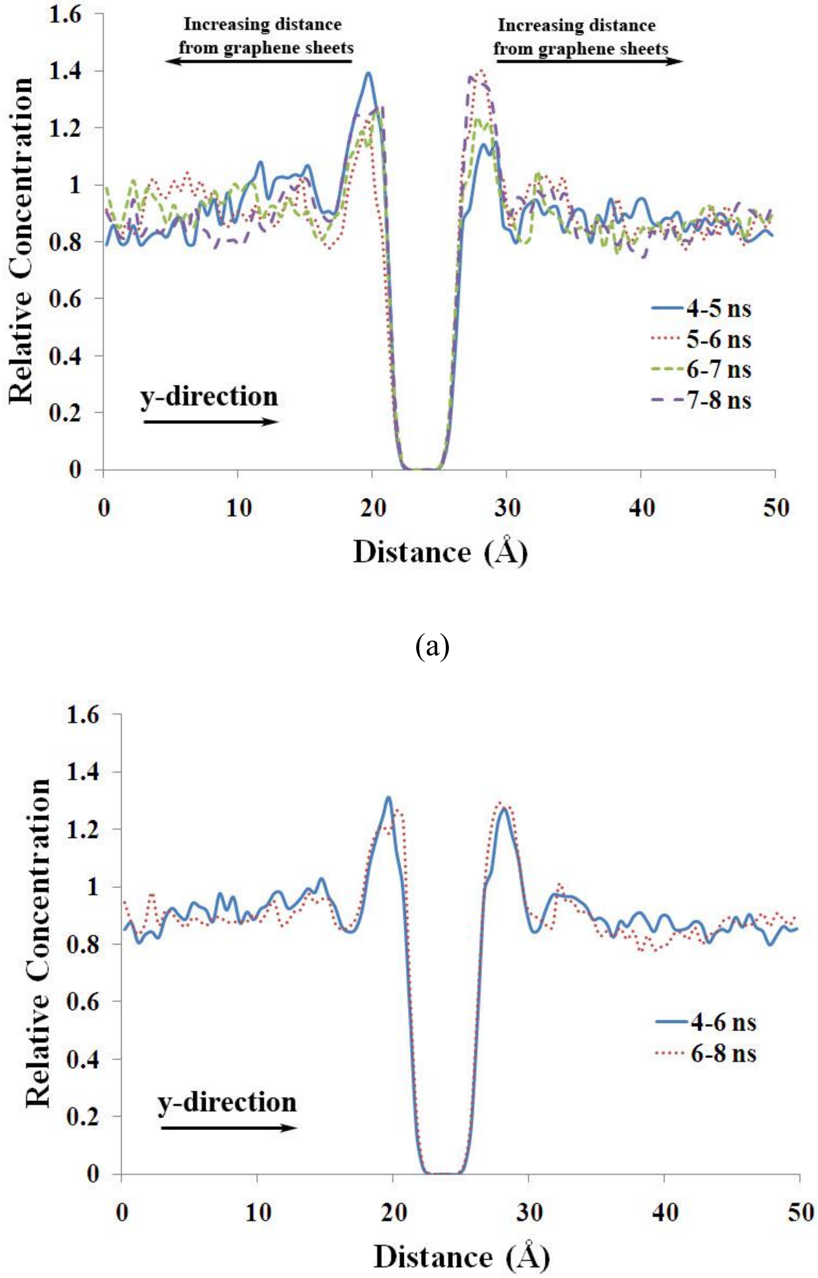

(a)

(b)

Figure 2.7 Styrene concentration profiles, time-averaged over each successive 1 ns (a) and 2 ns (b) time intervals at 1000 K.

Upon cooling, the equilibrium of the system was verified. Two cooling procedures were followed to investigate the effect of cooling on the concentration profiles and the re-equilibration process. After the system was cooled to 300 K, the time-averaged concentration profiles for styrene (cooled by both the C1 and C2 procedures defined earlier) were compared (Figure 2.8). No major differences were observed between the two cooling procedures. The averages were calculated for both C1 and C2 over each 1 ns time interval within a total simulation time of 5 ns. The time-averaged concentration profiles closely matched each other, indicating that equilibrium had been reestablished at the lower temperature. The VE1 and VE2 concentration profiles for C1 and C2 cooling procedures are given in Appendix A (Figures 2.A.3 and 2.A.4).

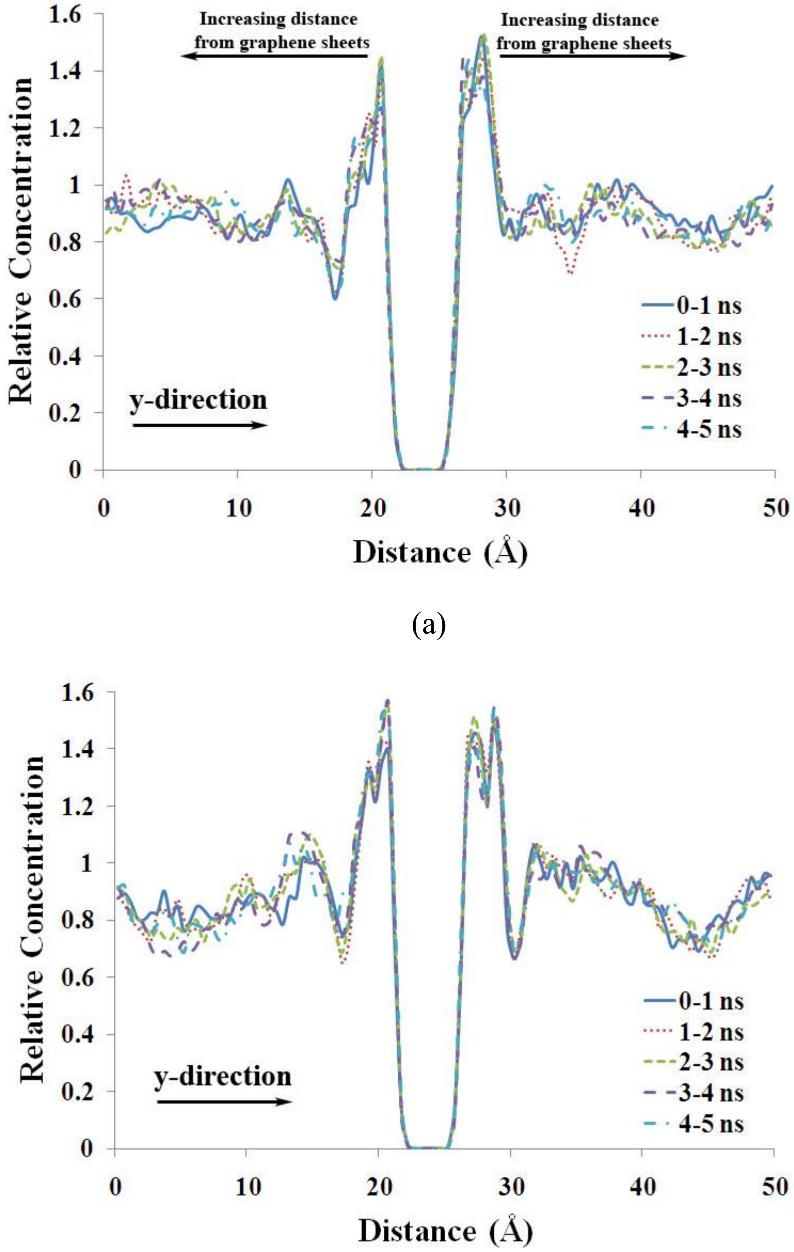

(a)

(b)

Figure 2.8 Styrene concentration profiles, time-averaged over each successive 1 ns time interval at 300 K (total simulation time of 5 ns) for simulations following cooling procedures C1 (a) and C2 (b).

The monomer concentration profiles obtained through simulations following cooling procedures C1 and C2 were averaged over both simulations and over the total simulation time of 5 ns at 300 K to get a better estimate of the monomer distributions in the simulation cell. These simulation and time-averaged concentration profiles are shown in Figure 2.9.

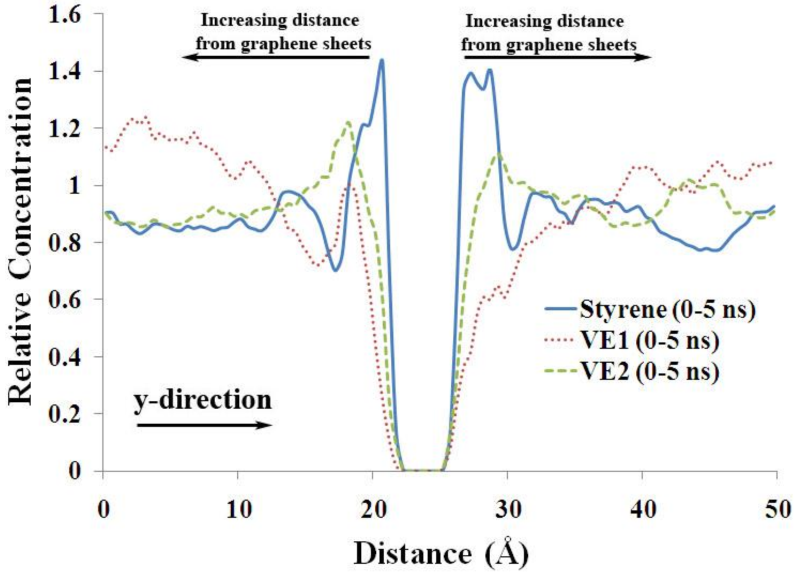

Figure 2.9 Concentration profiles of styrene, VE1, and VE2 averaged over the two simulations, which employed cooling procedures C1 and C2, respectively, and over 5 ns at 300 K for each simulation.

To obtain a more realistic estimate of the monomer distributions perpendicular to the nanofiber surface, the relative concentrations were averaged over both sides of the overlapping graphene sheets as shown in Figure 2.10. In a real VGCNF/VE composite, the resin monomers can only wet the *outer* nanofiber surface (here, one side of the graphene sheet assembly). In the figure, the graphene sheets lie in the region corresponding to y > 22 Å. The surface relative concentrations of styrene and VE2 are higher than in the bulk resin, while the VE1 relative concentration adjacent to the surface is lower. It should be emphasized again that the effects of unphysical cross-sheet interactions between monomers (as discussed in 2.2) would tend to be stronger between polar VE/VE than nonpolar styrene/styrene molecules. This would occur because the magnitude of polar interactions is inversely proportional to the third power of their separation distance, while nonpolar interactions decrease with the sixth power of separation distance. Thus, the relative concentration of styrene at the surface would likely be a little higher than what was observed here if these cross-sheet interactions had not existed. On this basis, our predicted enhancement of the relative styrene concentration at the nanofiber surface is a conservative value.

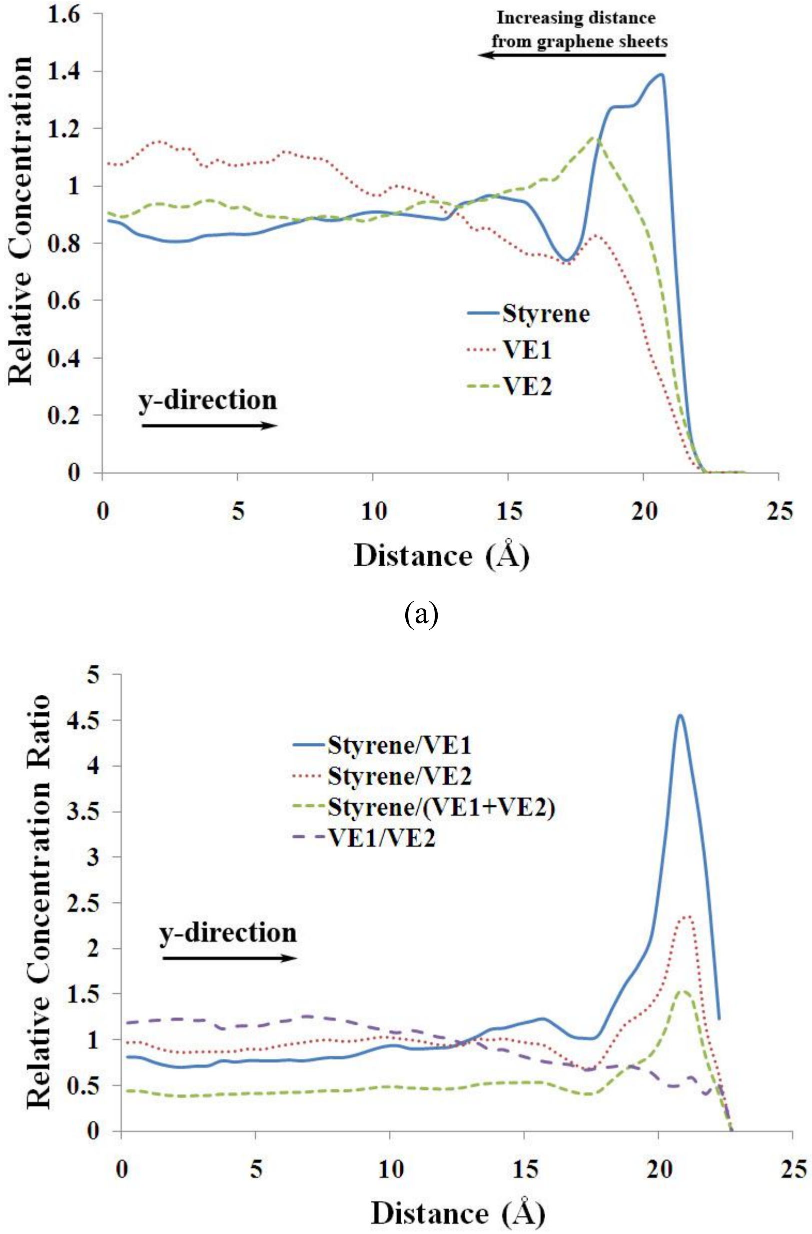

(a)

(b)

Figure 2.10 Concentration profiles of styrene, VE1, and VE2 (a) and monomer relative concentration ratios (b), where simulations were averaged after following cooling procedures C1 and C2 over the total simulation times of 5 ns at 300 K for each procedure (results are averaged over both sides of the graphene sheets).

The final simulated monomer distributions represent the amount of each monomer at each plane roughly parallel to the nanofiber surface. This is better depicted by calculating the relative monomer concentration ratios (equivalent to relative mole ratios) available versus distance from the nanofiber surface (Figure 2.10b). It is clearly evident in Figure 2.10b that the styrene/VE1 relative concentration ratio starts to increase about 10 Å away from the graphene surface and reaches a peak relative concentration ratio that is 4.5 times that of the bulk value near the surface.

The styrene/VE2 relative concentration ratio shows a peak of 2.5 near the surface (Figure 2.10). Thus, the relative concentration ratio of styrene to the sum of both VE monomers is higher near the nanofiber surface, while the VE1/VE2 ratio is a relative minimum. These simulations predict that styrene migration will occur, producing a higher styrene concentration within an approximately 5 Å thick region adjacent to the nanofiber surface. The near-surface concentration of VE1 decreases significantly, while that of VE2 is less depleted. The interaction of styrene molecules with the graphene surface plus the remaining surrounding molecules is more favorable than the interactions of styrene with surrounding molecules in the original bulk liquid resin.

The major changes in the relative monomer concentration ratios occur in the 5 Å thick region surrounding the graphene sheets extending further out to about 10 Å. This may have significant consequences for composites made by curing a VE resin with dispersed nanofibers. If the VE matrix produced by free radical-initiated curing incorporates the monomers in their relative concentration ratios found in the 5-10 Å liquid region adjacent to the graphene surfaces prior to curing, the resulting matrix in that region will differ substantially from that of the bulk matrix structure. The resulting matrix would then contain more styrene at the nanofiber/matrix surface, with a corresponding increase in the distance between the crosslinks. The local increase in the VE2/VE1 ratio near the interface would also increase the distance between the crosslinks. Both effects would generate a thin interphase region with low modulus. If this region averaged 10 Å or even 20 Å (e.g., 1 or 2 nm), it would be small relative typical VGCNF diameters (70-200 nm). Thus, it would represent a small volume fraction and the mechanical properties of this region would likely have a negligible effect on the composite homogenized elastic moduli. However, since styrene interacts favorably with the graphene surface, a thin soft matrix layer near the surface might exhibit a higher interfacial shear strength than a more highly crosslinked matrix region with a smaller styrene content.

The size of the computational repeating cell used will lead to an underestimation of the styrene concentration adjacent to the graphene surface. This occurs because, as styrene migrates towards the surface, its bulk concentration decreases within the unit cell, with a compensating increase in the bulk concentration of VE2 and especially VE1. In a real composite, the volume of the bulk liquid resin relative to the volume near the nanofiber surface is far larger than that represented in these simulations. Thus, in real composites, the bulk concentration of styrene will be essentially unchanged after equilibrium is reached. Therefore, the driving forces for the migration of styrene away from the surface during equilibration will be smaller than those represented here. This will also bias the simulation to give a conservative estimate of the styrene build-up in the volume very close to the nanofiber surface. The relative monomer distributions at the end of the simulation are shown in Figure 2.11. These snapshots were obtained following the cooling procedure C2 at a total simulation time of ~ 13 ns at a temperature of 300 K.

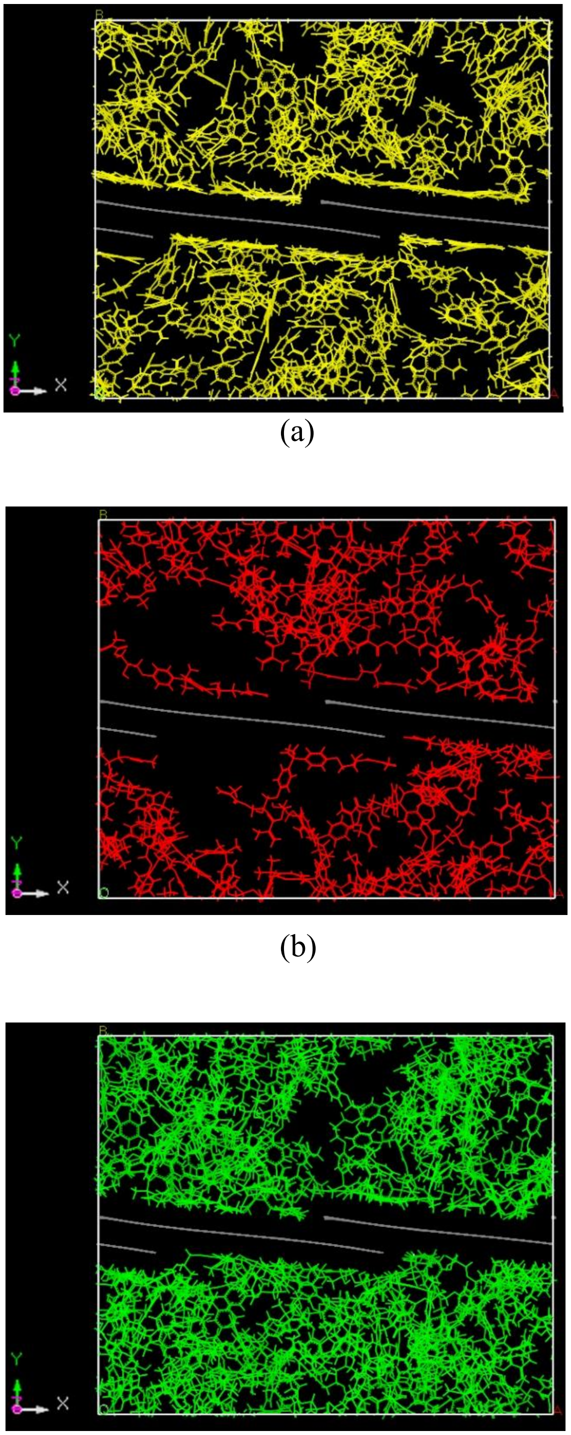

Figure 2.11 The distribution and arrangement of styrene molecules (a), VE1 molecules (b), and VE2 molecules (c) around the graphene sheets.

The phenyl rings of the styrene strongly align at the interface, parallel to the faces of the graphene sheets (Figure 2.11a). This optimizes π-π stacking and lowers the total energy. This interaction appears more favorable than the interactions of styrene with other monomers in the liquid resin and is a driving force for the build-up of the styrene-rich layer on the nanofiber surface. VE2 molecules are very large and extend over long distances in the simulation cell. A VE2 molecule has four aromatic rings versus only two for VE1. These rings are bonded to the tetrahedral –$C(CH_3)_2$- function, which sterically hinders their ability to lay flat against the graphene sheets (Figure 2.11c). Thus, each ring can only achieve a portion of the π-π stacking interaction that styrene achieves. However, with four aromatic rings in its structure, each VE2 molecule can achieve a larger favorable interaction with graphene surfaces. Apparently, this results in higher VE2 versus VE1 concentration near the surface. Of course, these explanations are tentative because the sum of all the interactions of each type of monomer in the bulk must be compared to the sum of all the interactions of each type of monomer at or near the nanofiber surface.

2.6 Conclusions

Molecular dynamics simulations were performed to study the interactions between vinyl ester (VE) resin monomers (bisphenol-A-glycidyl dimethacrylates) and styrene with the surface of a pristine vapor-grown carbon nanofiber (VGCNF). The monomer concentration profiles were determined at equilibrium to investigate the monomer distributions versus the distance from the nanofiber surface. The styrene/VE monomer ratios were found to be substantially higher within 5 Å of the nanofiber-resin surface compared to their bulk ratios. These modified monomer relative concentration ratios near the nanofiber surface may result in a thin (5-10 Å thick) interphase region of a few molecular layers if they are retained within the matrix structure during curing. The accumulation of styrene in the immediate vicinity of the nanofiber surface and the increased VE2/VE1 ratio is anticipated to yield a locally more compliant matrix with a lower crosslink density.

The pronounced accumulation of styrene, with its phenyl rings lying parallel to the graphene sheets due to π-π stacking interactions, suggests that a lightly crosslinked interphase with a large number of styrene-graphene interactions could result in improved nanofiber-matrix interfacial shear strengths compared to a more highly crosslinked matrix with bulk monomer composition. This study is one of the few investigations of liquid monomer-nanofiber interactions that directly address the interphase formation in VE matrix nanoreinforced composites.

2.7 Acknowledgement

This work was sponsored by the U. S. Department of Energy under contract DE-FC26-06NT42755. We wish to acknowledge William Joost, Department of Energy's technology area development manager, and the Center for Advanced Vehicular Systems (CAVS) at Mississippi State University for their support.

2.8 Appendix A. Supplementary Data

In this appendix, supplementary concentration profiles are provided for VE1 and VE2 monomers pertaining to simulations run at 1000 K and 300 K.

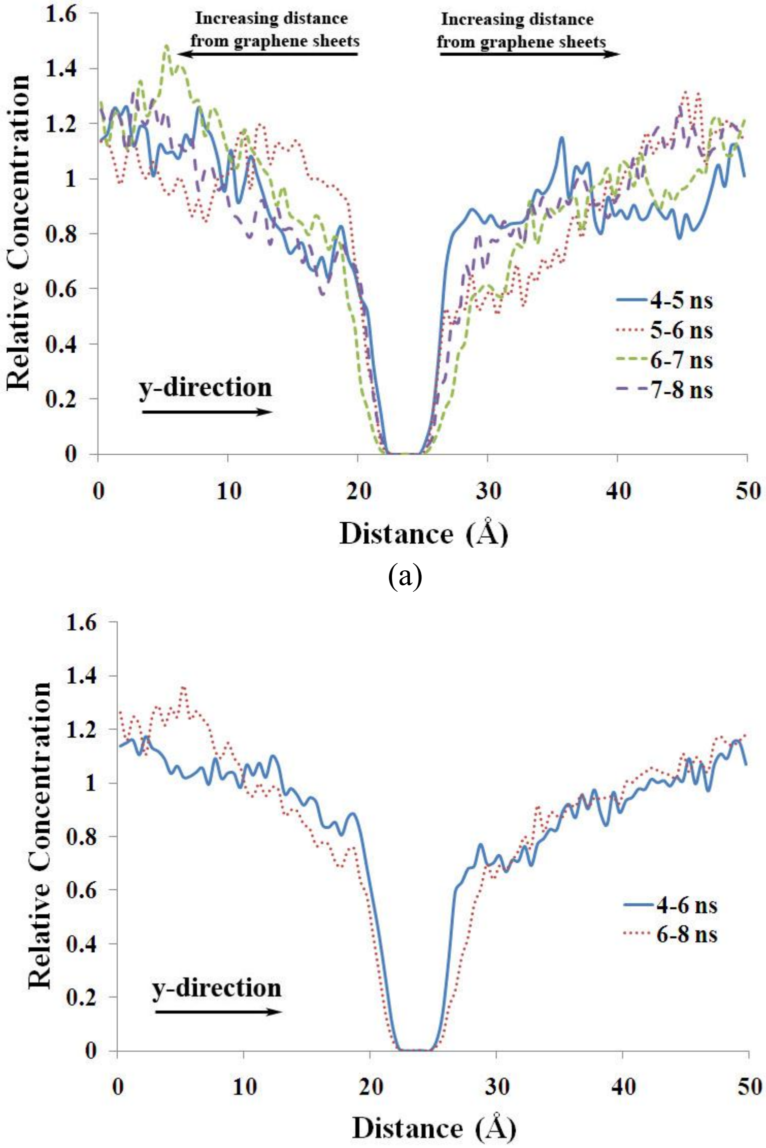

(a)

(b)

Figure 2.12 Concentration profiles of VE1, time-averaged over each successive 1 ns (a) and 2 ns (b) time intervals at 1000 K.

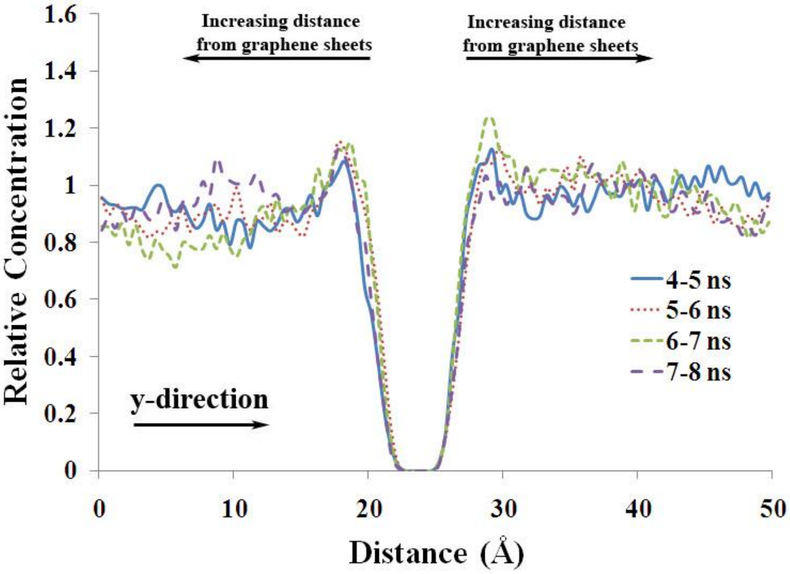

(a)

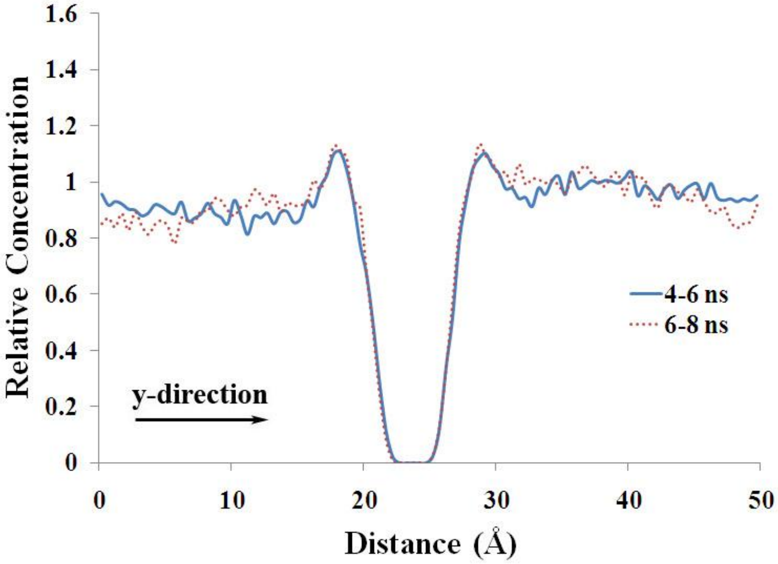

(b)

Figure 2.13 Concentration profiles of VE2, time-averaged over each successive 1 ns (a) and 2 ns (b) time intervals at 1000 K.

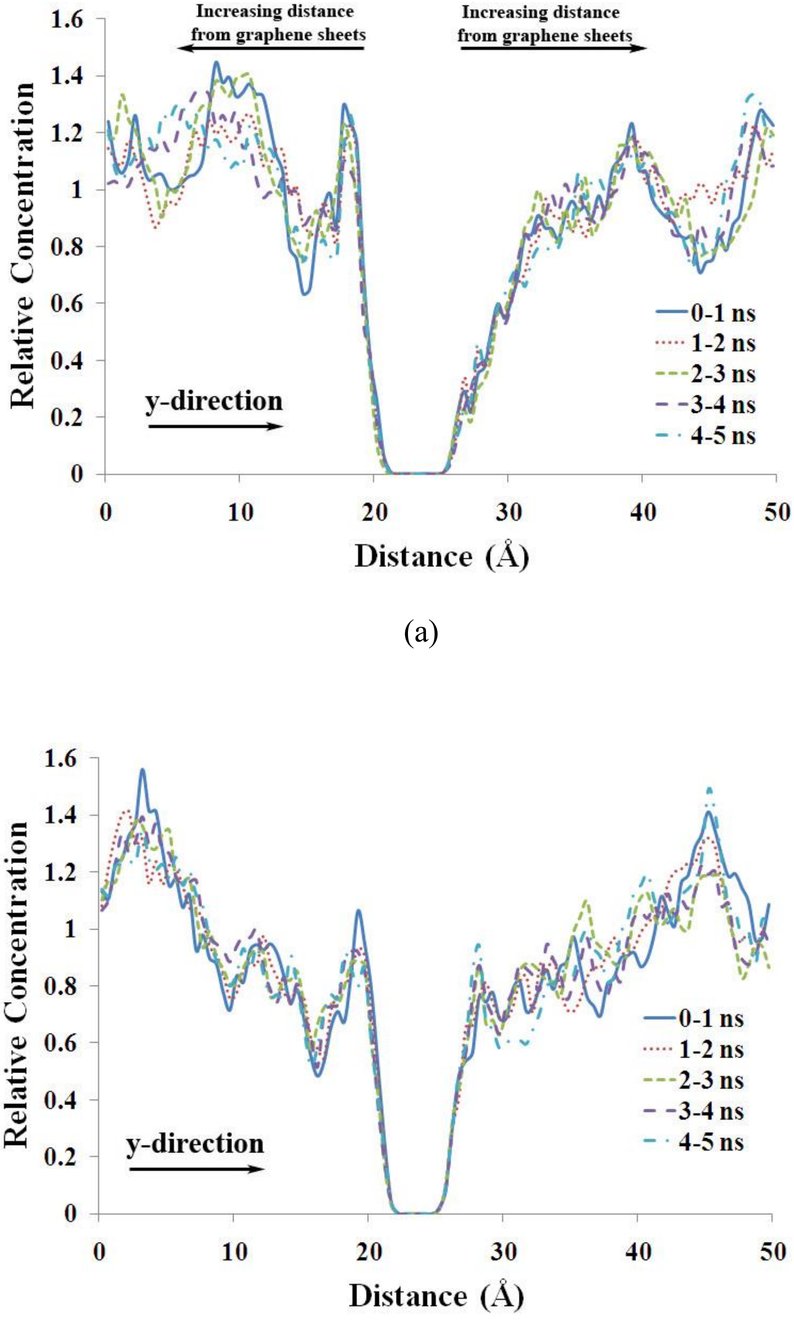

(a)

(b)

Figure 2.14 Concentration profiles of VE1 time-averaged over each successive 1 ns time interval at 300 K (total simulation time of 5 ns) for simulations following cooling procedure C1 (a) and C2 (b).

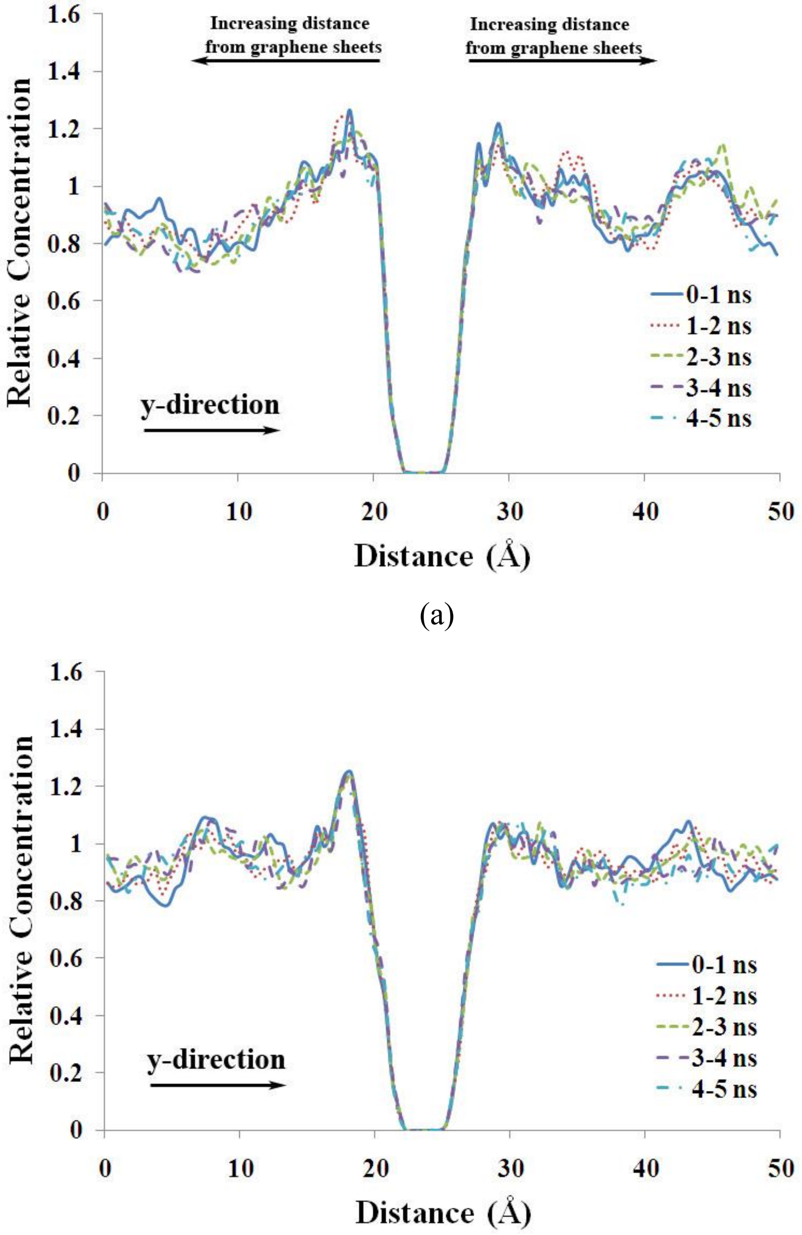

(a)

(b)

Figure 2.15 Concentration profiles of VE2 time-averaged over each successive 1 ns time interval at 300 K (total simulation time of 5 ns) for simulations following cooling procedure C1 (a) and C2 (b).

2.9 References

Ashland Chemical Co., “Derakane 441-400 Vinyl Ester Resin Property Data Sheet.” http://www.ashland.com, 2011.

Baller, J., Becker, N., Ziehmer, M., Thomassey, M., Zielinski, B., Müller, U., *et al*., “Interactions between silica nanoparticles and an epoxy resin before and during network formation,” *Polymer,* 2009, 50(14), 3211-3219.

Burchell, T. D., “Carbon materials for advanced technologies,” 1999, Oxford, UK: Perfamon (Elsevier Science LTD.).

Chowdhury, S. C., and Okabe, T., “Computer simulation of carbon nanotube pull-out from polymer by molecular dynamics method,” *Composites A,* 2007, 38, 747-754.

Coleman, J. N., Cadek, M., Ryan, K. P., Fonseca, A., Nagy, J. B., Blau, W. J., *et al*., “Reinforcement of polymers with carbon nanotubes: the role of an ordered polymer interfacial region, experiment and modeling,” *Polymer,* 2006, 47, 8556-8561.

Cook, D. W., Simon, G. P., Burchill, P. J., Lau, M., and Fitch, T. J., “Curing kinetics and thermal properties of vinyl ester resins,’ *Journal of Applied Polymer Science,* 1997, 64(4), 769-781.

Donnet, J-B., Rebouillat, S. R., Wang, T. K., and Peng, J. C. M., “Carbon fibers,” 3rd ed. New York: Marcel Dekker; 1998.

Endo, M., Kim, Y. A., Hayashi, T., Nishimura, K., Matusita, T., Miyashita, K., and Dresselhaus, M. S., “Vapor-grown carbon fibers (VGCFs): Basic properties and their battery applications,” *Carbon,* 2001, 39(9), 1287-1297.

Frankland, S. J. V., Caglar, A., Brenner, D. W., and Griebel, M., “Molecular simulation of the influence of chemical cross-links on the shear strength of carbon nanotube-polymer interfaces,” *The Journal of Physical Chemistry B,* 2002, 106, 3046-3048.

Gou, J., Minaei, B., Wang, B., Liang, Z., and Zhang, C., “Computational and experimental study of interfacial bonding of single-walled nanotube reinforced composites,” *Computational Materials Science,* 2004, 31, 225-236.

Gou, J., Liang, Z., Zhang, C., and Wang, B., “Computational analysis of effect of single-walled carbon nanotube rope on molecular interaction and load transfer of nanocomposites,” *Composites B*, 2005, 36, 524-533.

Gou, J., Anumakonda, K., and Khan, A., "Molecular dynamics simulation of interactions between functionalized carbon nanofibers and polymer resins," *International Journal of Nanoscience*, 2007, 6(6), 443-452.

Harper, C. A., "Handbook of plastics, elastomers, and composites," 4th ed. New York: McGraw-Hill; 2002: 598-599.

Iijima, S., "Helical microtubules of graphitic carbon," *Nature*, 1991, 354, 56-58.

Jancar, J., "Review of the role of the interphase in the control of composite performance on micro- and nano-length scales," *Journal of Materials Science,* 2008, 43, 6747-6757.

Jancar, J., "Interphase phenomena in polymer micro- and nanocomposites. In: Karger-Kocsis J, Fakirov S, editors. Nano- and micro-mechanics of polymer blends and composites," Cincinnati; Hanser Publications; 2009, 241-266.

Kroto, H. W., Heath, J. R., O'Brien, S. C., Curl, R. F., and Smalley, R. E., "C_{60}: Buckminsterfullerene," *Nature*, 1985, 318, 162-163.

Li, H., "Synthesis, characterization, and properties of vinyl ester matrix resins," Blacksburg VA USA, Virginia Polytechnic Institute and State Univ, PhD dissertation, 1998.

Liao, K., and Li, S., "Interfacial characteristics of a carbon nanotube-polystyrene composite System," *Applied Physics Letters*, 2001, 79(25), 4225-4227.

Maruyama, B., and Alam, K., "Carbon nanotubes and nanofibers in composite materials," SAMPE Journal 2002, 38(3), 59–70.

McConnell, V. P., "Vinyl esters get radical in composite markets," Reinforced Plastics November/December 2010, 34-38.

Montazeri, A., and Naghdabadi, R., "Investigation of the interphase effects on the mechanical behavior of carbon nanotube polymer composites by multiscale modeling," *Journal of Applied Polymer Science,* 2010, 117(1), 361-367.

Nouranian, S., Toghiani, H., Lacy, T. E., Pittman, Jr C. U., and Dubien, J., "Dynamic mechanical analysis and optimization of vapor-grown carbon nanofiber/vinyl ester nanocomposites using design of experiments," *Journal of Composite Materials,* 2010, DOI: 10.1177/0021998310385027.

Novoselov, K. S., Geim, A. K., Morozov, S. V., Jiang, D., Zhang, Y., Dubonos, S. V., et al., "Electric field effect in atomically thin carbon films," *Science*, 2004, 306, 666-669.

Peebles, L. H., “Carbon fibers. Formation, structure and properties,” Boca Raton: CRC Press; 1995.

Putz, K., Krishnamoorti, R., and Green, P. F., “The role of interfacial interactions in the dynamic mechanical response of functionalized SWNT-PS nanocomposites,” *Polymer,* 2007, 48, 3540-3545.

Qiao, R., and Brinson, L. C., “Gradient interphases in polymer nanocomposites,” Technical paper, ASME 2009 International Mechanical Engineering Congress and Exposition. Lake Buena Vista (Florida. USA): 2009, 883-884.

Schadler, L. S., Brinson, L. C., and Sawyer, W. G., “Polymer nanocomposites: a small part of the story,” *Nanocomposite Materials,* 2007, 50-58.

Sikdar, D., Katti, D. R., Katti, K. S., and Bhowmik, R., “Insight into molecular interactions between constituents in polymer clay nanocomposites,” *Polymer,* 2006, 47, 5196-5205.

Sikdar, D., Katti, D. R., and Katti, K. S., “The role of interfacial interactions on the crystallinity and nanomechanical properties of clay-polymer nanocomposites: a molecular dynamics study,” *Journal of Applied Polymer Science,* 2008, 107, 3137-3148.

Sun, H., “COMPASS: an ab initio force-field optimized for condensed-phase applications: overview with details on alkane and benzene compounds,” *Journal of Physical Chemistry B,* 1998, 102(38), 7338-7364.

Tang, L-G., and Kardos, J. L., “A review of methods for improving the interfacial adhesion between carbon fiber and polymer matrix,” *Polymer Composite,* 1997, 18(1), 100-113.

Tibbetts, G. G., Lake, M. L., Strong, K. L., and Rice, B. P., “A review of the fabrication and properties of vapor-grown carbon nanofiber/polymer composites,” *Composite Science and Technology,* 2007, 67(7-8), 1709-1718.

Uchida, T., Anderson, D. P., Minus, M. L., and Kumar, S., “Morphology and modulus of vapor grown carbon nano fibers,” *Journal of Materials Science,* 2006, 41, 5851-5856.

Vaia, R. A., and Giannelis, E. P., “Polymer nanocomposites: status and opportunities,” *Materials Research Society Bulletin,* 2001, 26(5), 394-401.

Xu, L., “Interfacial engineering of the interphase between carbon fibers and vinyl ester resin,” East Lansing MI USA, Michigan State Univ, PhD dissertation, 2003.

Yosomiya, R., Morimoto, K., Nakajima, A., Ikada, Y., and Suzuki, T., "Adhesion and bonding in Composites," New York: Marcel Dekker; 1989.

Zhu, Y. A., Sui, Z. J., Zhao, T. J., Dai, Y. C., Cheng, Z. M., *et al*., "Modeling of fishbone-type carbon nanofibers: a theoretical study," *Carbon*, 2005, 43, 1694-1699.

CHAPTER 3

MOLECULAR DYNAMICS SIMULATIONS OF OXIDIZED VAPOR-GROWN CARBON NANOFIBER SURFACE INTERACTIONS WITH VINYL ESTER RESIN MONOMERS

3.1 Abstract

Surface oxidation effects on the liquid vinyl ester (VE) monomer distributions near two oxidized vapor-grown carbon nanofiber (VGCNF) surfaces were studied using molecular dynamics simulations. Two overlapping graphene sheets containing oxygenated functions represented the oxidized VGCNF surfaces. Two liquid VE bisphenol-A dimethacrylates (designated VE1 and VE2, respectively) and styrene constituted the resin. Temporally and spatially averaged relative monomer concentrations, calculated in a direction away from the oxidized graphene surfaces, showed increased styrene and VE1 concentrations. Monomer molar ratios found within a 10 Å thick region adjacent to the oxidized graphene sheets were substantially different from those of the bulk resin. Curing should result in the formation of a very thin interphase region of different composition. The crosslink structure of such an interphase will be distinct from that of an unoxidized VGCNF surface. The enhanced VE1 concentration near this oxidized surface should give a higher crosslink density, leading to a stiffer interphase than that adjacent to unoxidized VGCNF surfaces. VGCNF-matrix

adhesion may also be modified by the different interphase monomer molar ratios. These studies may facilitate multiscale material design by providing insight into carbon nanofiber-matrix interactions leading to improved macroscale composite properties.

3.2 Introduction

Nanoreinforced polymer composites are increasingly being used in structural and multifunctional applications [Hussain *et al.*, 2006]. Significant mechanical property improvements have been realized by incorporating small amounts of low cost vapor-grown carbon nanofibers (VGCNFs) [Carneiro *et al.*, 1998, Chávez-Medellín *et al.*, 2010, Choi *et al.*, 2005, Choi *et al.*, 2006, Faraz *et al.*, 2010, Lee *et al.*, 2010, Nouranian *et al.*, 2010, Ren *et al.*, 2008, Zhou *et al.*, 2007] due to their superb mechanical properties [Tibbetts *et al.*, 2007]. VGCNFs have diameters in the range of 70-200 nm and lengths of 50-200 microns.[a] VGCNFs have been used to reinforce different polymer matrices, but large-scale nanofiber entanglements, dispersion difficulties, and poor interfacial adhesion limit their effectiveness. Poor adhesion decreases load transfer between the matrix and the nanofiber. Hence, attempts have been made to oxidize or otherwise treat nanofiber surfaces to generate surface functional groups, which enhance interfacial adhesion and aid VGCNF de-agglomeration and dispersion in the matrix [Lakshminarayanan *et al.*, 2004, Li *et al.*, 2005, Rasheed *et al.*, 2006].

---

[a] Pyrograf Products (an Affiliate of Applied Sciences, Inc.) http://pyrografproducts.com/Merchant5/merchant.mvc?Screen=cp_nanofiber (date accessed: June 9, 2011).

Oxidizing VGCNFs introduces hydroxyl, carbonyl, carboxylic acid, anhydride and other surface functional groups [Klein *et al*., 2008, Lakshminarayanan *et al*., 2004]. These functions interact with the resin constituents through hydrogen bonding and dipole-dipole attractions. This promotes better wetting and improves nanofiber-matrix contact. Favorable interactions may result in selective adsorption of liquid resin monomers on the carbon nanofiber surfaces [Drzal 1986, Palmese 1992]. As a consequence, local monomer molar ratios at the nanofiber surface may differ from those of the bulk liquid resin. Monomers crosslink during curing, so the final composition of the crosslinked matrix in the immediate vicinity of the nanofiber-matrix interface could differ from those of the bulk matrix. This results in an “interphase” region with distinct physical and mechanical properties [Jancar 2008, Jancar 2009, Schadler *et al*., 2007, Vaia and Giannelis 2001]. The existence of an interphase in polymer matrices reinforced with nano-inclusions may have a profound impact on effective composite properties given the high surface-area-to-volume ratio associated with many nanoreinforcements [Ciprari *et al*., 2006, Jancar 2008, Ramanathan *et al*., 2005, Ramanathan *et al*., 2008, Saber-Samandari and Afaghi Khatibi 2006].

The authors recently studied the equilibrium distribution of monomers in a liquid vinyl ester (VE) resin [Ashland Chemical Co. 2011] near a *pristine* (unoxidized) VGCNF surface using molecular dynamics (MD) simulations [Nouranian *et al*., 2011]. The pristine VGCNF surface was idealized using overlapping graphene sheets in direct contact with a VE resin composed of three monomer constituents: styrene and two VE dimethacrylates with one and two bisphenol-A groups (n) in their backbones, designated as VE1 (n =1) and VE2 (n =2), respectively. A combination of high temperature (600 K, 1000 K) and room temperature (300 K) simulations were used to establish the initial and final equilibrium distributions of the three liquid resin monomers in a direction away from the graphene sheets in the simulation cell. A styrene-rich layer was formed in a ~5 Å thick region surrounding the graphene sheets [Nouranian *et al*., 2011]. This implied that a relatively compliant interphase region of lower crosslink density may form in the resulting composite upon resin curing.

In the current study, the interactions between the same VE resin monomer composition and an *oxidized* VGCNF surface were investigated using the methodology outlined in [Nouranian *et al*., 2011]. The interfacial interactions between oxidized VGCNFs and the VE resin will influence both the formation and properties of the interphase upon curing, as well as the matrix-to-nanofiber adhesion. Knowledge of the interphase and interfacial properties is crucial for multiscale composite materials design and modeling, because the interphase volume fraction may be quite significant and the monomer composition of the resin in direct contact with the surface will dominate matrix-reinforcement adhesion. Characterization of liquid resin concentration profiles in the near surface regions and their implications for interphase formation in reinforced thermoset composites have never been investigated using MD simulations. This work in combination with the previous study [Nouranian *et al*., 2011] represents the first attempts to do so. In principle, this methodology could be applied to any liquid resin composed of two or more monomers and any solid surface.

3.3 Molecular Models

3.3.1 Models of Vinyl Ester Monomers

Commercial Derakane 441-400 VE resin [Ashland Chemical Co. 2011] with 33 wt% styrene served as the model resin in this study [Ciprari *et al*., 2006, Nouranian *et al*., 2010]. It has an average of $n = 1.62$ bisphenol-A groups in the dimethacrylate backbone and an average molecular weight of 690 g/mol [Li 1998]. The general chemical formula of the VE dimethacrylate monomer and the specific structures for the VE dimethacrylates, VE1 and VE2, are shown together with styrene in Figure 3.1. The Derakane 441-400 VE resin composition was a solution of VE1, VE2 and styrene monomers at a VE1/VE2 mole ratio of 35/61, which yielded the average value of $n = 1.62$.

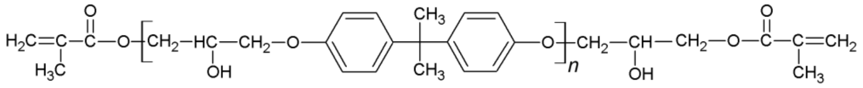

(a) Derakane 441-400 (n = 1.62)

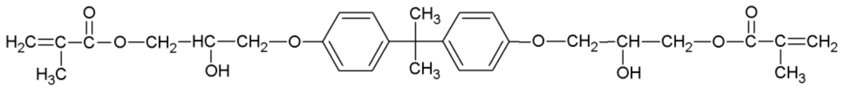

(b) VE1 (n = 1)

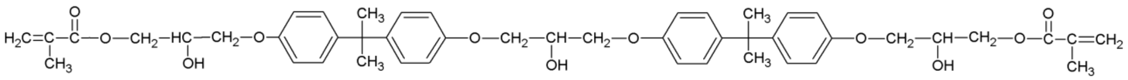

(c) VE2 (n = 2)

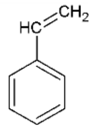

(d) Styrene

Figure 3.1 Vinyl ester resin based on Bisphenol-A dimethacrylates: (a) General formula based on Derakane 441-400, (b) chemical structure of VE1 (*n* =1), (c) chemical structure of VE2 (*n* = 2), and (d) styrene.

3.3.2 Model of the Oxidized VGCNF Surface

VGCNFs are hollow structures composed of conical graphene sheets arranged in stacked-cup morphology. This is shown in Figures 3.2a and 3.2c. For MD simulation purposes, the surface of a VGCNF was idealized using two overlapping flat graphene sheets tilted slightly to represent the edge region of the cone in the known VGCNF stacked-cup microstructure (Figures 3.2b and 3.2c) [Nouranian *et al.*, 2011]. Flat graphene sheets were used in the MD simulation because the repeating unit cell size used was 6×5×6 nm^3. Thus, the 5×6 nm^2 region shown on the curved, 70-200 nm diameter nanofiber surface is very close to being planar (Figures 3.2c and 3.2d) [Nouranian *et al.*, 2011]. Representative oxygen-containing functional groups were manually introduced in a randomly distributed fashion on the basal plane of the graphene sheets as shown in Figure 3.2b. This is just one example of an oxidized VGCNF surface. The ratio of the types of oxygenated surface functional groups could change as the degree of surface oxidation changes. In Figure 3.2d, a low level of oxidation damage to the graphene sheet's basal plane is shown as circled openings (holes) in the sheet. These occur when oxidation breaks carbon-carbon bonds during the formation of carboxylic acid, quinoid carbonyl or phenolic hydroxyl groups, and thereby destroys the continuous hexagonal ring structure.

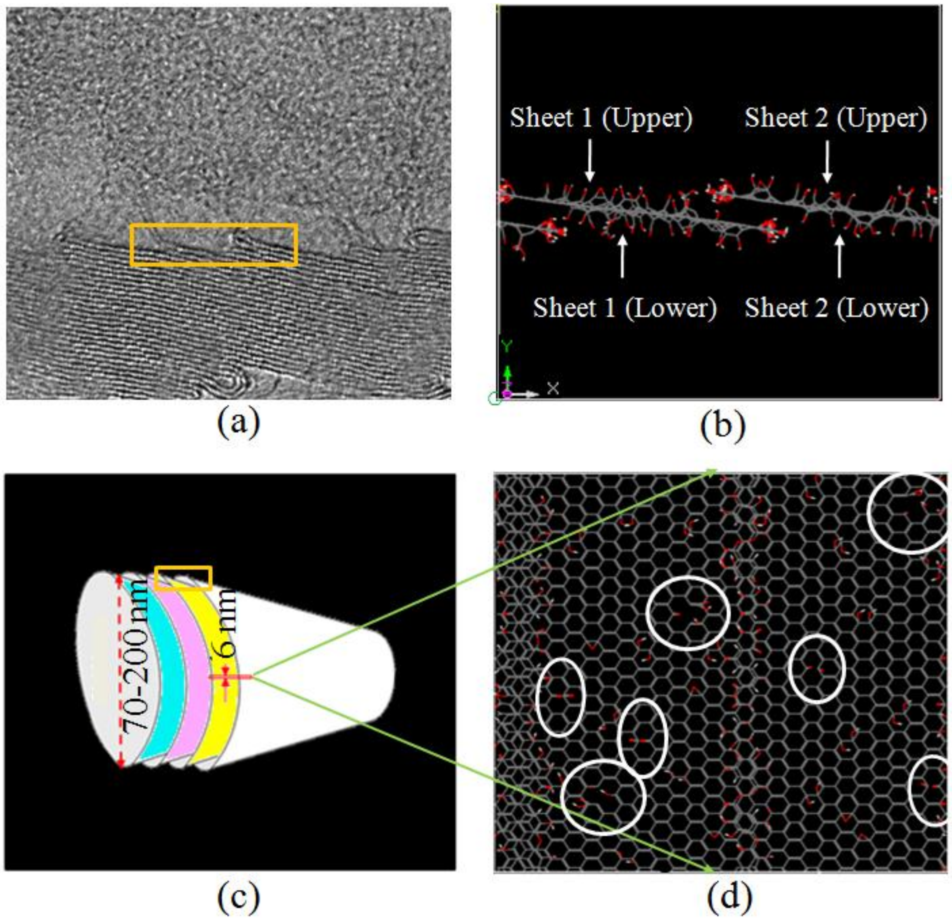

Figure 3.2 (a) Overlapping graphene sheets representing the edge portion of a real VGCNF with the stacked-cup morphology (adapted from [Endo *et al*., 2003]). (b) View of the MD simulation cell with designated oxidized graphene sheets arranged like shingles. (c) Schematic of the stacked-cup nanofiber morphology with actual versus MD scale dimensions. (d) Graphene surface with holes caused by oxidation damage (circled portions).

Representative oxidized functional groups were manually introduced along both upper and lower basal planes (surfaces). Furthermore, the lateral planes (edges) of the graphene sheets were similarly oxidized to represent the lateral plane surface regions of experimentally functionalized VGCNFs. The concentration of the functional groups generated along the edges was far higher than in the basal planes, consistent with the actual rate of oxidation at these locations [Lakshminarayanan *et al*., 2004]. The functional groups introduced along the edges included phenolic hydroxyl, lactone, quinone, hydroquinone, and anhydride functions (Figures 3.3 and 3.4). Hydroxyl, epoxide, quinoid carbonyl, and carboxylic acid functions were added to the basal plane of the graphene sheets as shown in Figure 3.5, where the highlighted rings represent surface holes caused by oxidation damage to the graphene sheets. The presence of these functional groups was previously confirmed by Lakshminarayanan *et al.,* [Lakshminarayanan *et al*., 2004] for nitric acid-oxidized VGCNFs and by Gao *et al.,* [Gao *et al*., 2009] for the surface of graphite oxide. Both graphene basal surfaces (Figure 3.2b) had oxygen functional groups added because, as will be described later, the liquid resin in the MD simulation cell was present on both sides of the graphene sheets.

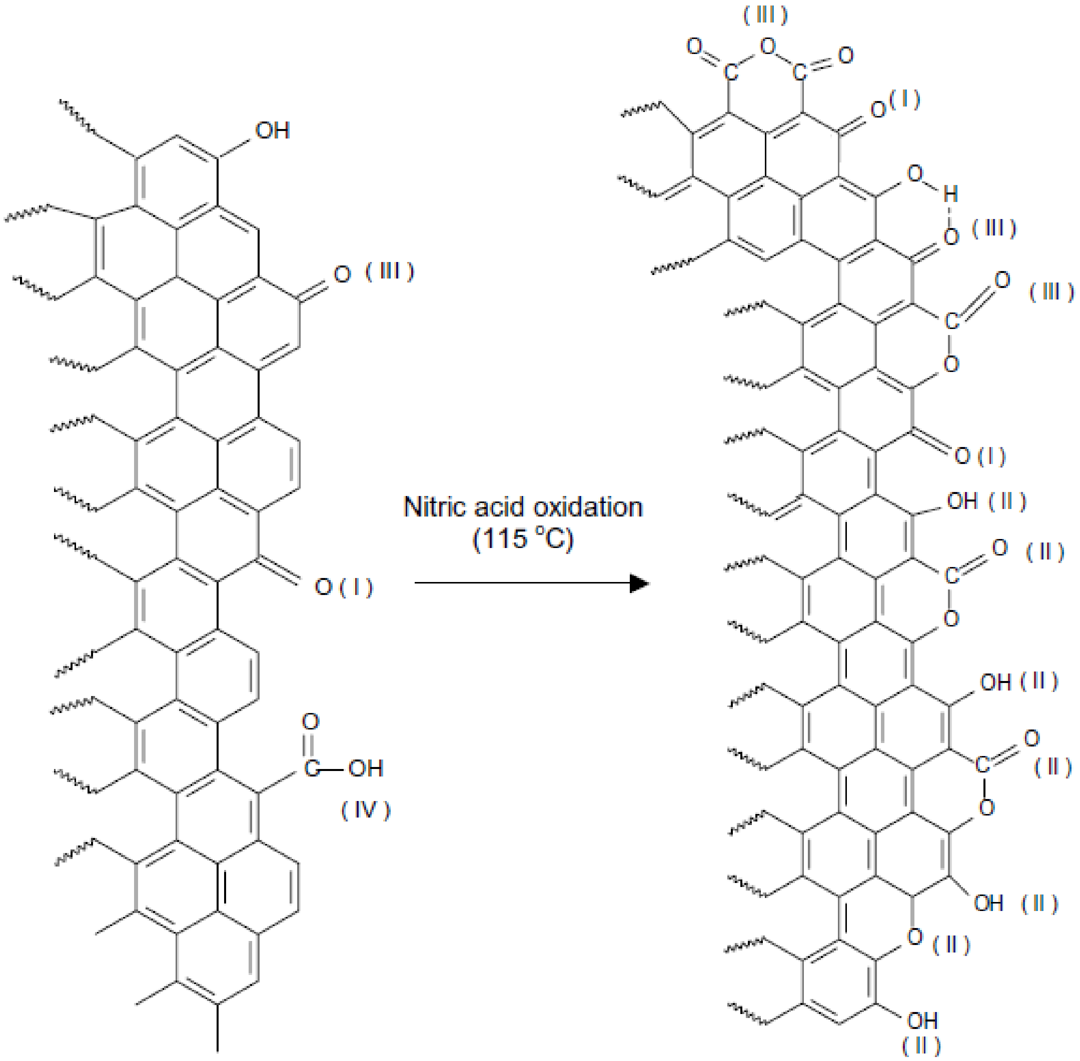

Unoxidized edge of VGCNF

Oxidized edge of VGCNF

Figure 3.3 Schematic representation of the edge chemistry of pristine and oxidized VGCNFs (adapted from [Lakshminarayanan *et al*., 2004]).

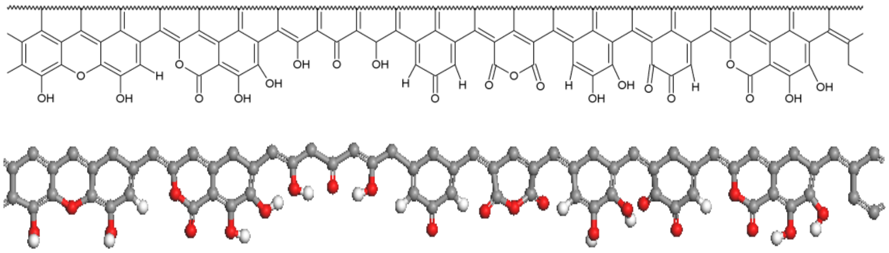

Figure 3.4 Schematic representation and the respective molecular model of the oxidized graphene edge showing the oxygen-containing functional groups.

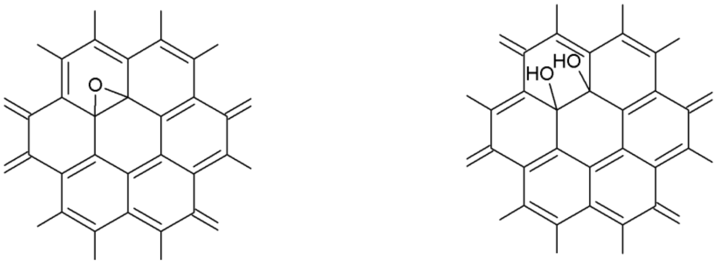

Epoxide

Hydroxyl

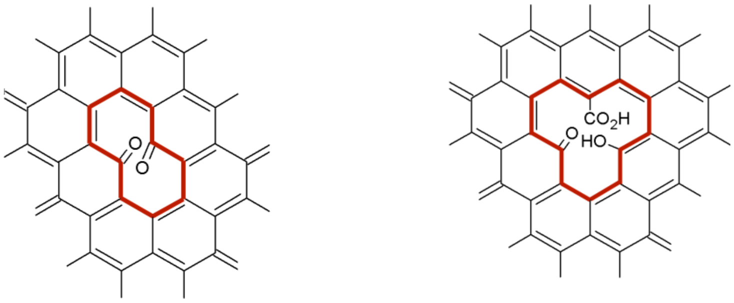

Quinoid carbonyl

Carboxylic acid

Figure 3.5 Surface functional groups introduced on the overlapping graphene sheets represented for sections of the graphene and holes caused by oxidation damage to the graphene sheets (bold regions).

The contact surfaces between the two overlapping graphene sheets (sheets 1 and 2 in Figure 3.2b) were not functionalized, since in real VGCNFs, the contact area between the stacked nanocones remains unoxidized. This conclusion is drawn from an experimental study [Lakshminarayanan *et al*., 2004] where VGCNFs were progressively oxidized in refluxing concentrated nitric acid for periods exceeding 24h without measureable weight loss. Temporal X-Ray Photoelectron Spectroscopy (XPS) studies showed that after initial surface oxidation, no further oxidation occurred for VGCNFs. This contrasts with polyacrylonitrile (PAN)-based continuous fibers which lose weight continuously as carbon is converted to CO_2. If subsurface oxidation could take place, one would expect VGCNFs to progressively oxidize and lose weight. VGCNFs can give ether-type functions below the surface layers at defects sites [Ros *et al*., 2002].

The surface density of the oxygen atoms on a basal plane is defined as the number of oxygen atoms per unit surface area of the sheet. The oxygen densities were 1.88/nm^2 and 1.77/ nm^2 on sheets 1 and 2 (Figure 3.2b), respectively. The average surface oxygen density on the two surfaces was 1.83/nm^2. The total number of functional groups and the ratio of oxygen (O) to carbon (C) on the graphene sheet basal planes are shown in Table 3.1. The number of functional groups and ratios O/C = 0.019-0.020 used in this study were chosen to correspond to a low/modest level of basal plane surface oxidation. For example, XPS data for surface-oxidized VGCNFs has shown an O/C ratio of 0.16 after 24h of oxidation in refluxing HNO_3 [Lakshminarayanan *et al*., 2004]. This implies that the oxygen density selected for this work represents a very mild oxidation treatment.

Table 3.1 The total number of functional groups on the graphene surfaces and their oxygen (O) to carbon (C) ratios.

	Number of functional groups					
	Epoxide	**Hydroxyl**	**Aromatic Ketone**	**Carboxylic Acid**	**O/C Ratio**	**Total O/C Ratio**
Sheet 1 Upper	2	11	3	1	0.02	0.02
Sheet 1 Lower	1	11	3	1	0.02	
Sheet 2 Upper	2	10	3	1	0.019	0.019
Sheet 2 Lower	1	9	3	1	0.019	

3.4 MD Simulation Details

3.4.1 The Simulation Cell

MD simulations were performed using Accelrys® Materials Studio® V5.0 software.[b] A cell of size 60×50×60 Å^3 was created and overlapping graphene sheets were positioned in the middle of the simulation cell [Nouranian *et al.*, 2011] with an inter-

---

[b] Accelrys, Inc. http://accelrys.com/products/materials-studio/

(date accessed: June 9, 2011)

planar distance of 3.5 Å as shown in Figure 3.6. This distance is close to the value of 3.4 Å reported by Zhu *et al.,* [Zhu *et al*., 2005] for fishbone-type carbon nanofibers. The sheets were oriented at a small angle (~9°) relative to the xz-plane of the unit cell (Figure 3.6a). Three dimensional (3D) periodic boundary conditions were employed. Initially, the oxidized graphene sheet structure was relaxed in a geometry optimization step. This resulted in an out-of-plane positioning of some graphene surface carbon atoms with their attached functional groups (inset in Figure 3.6a) since oxidation converted some graphene carbons from sp^2 (planar) to sp^3 (tetrahedral) hybridization. This occurs during epoxide formation and subsequent ring-openings to hydroxyl groups. Introducing carboxylic acid, quinoid carbonyls or internal phenolic functions generates "holes" in the 2-D hexagonal graphene sheet basal planes (Figure 3.2d and Figure 3.5). Next, the coordinates of the unoxidized graphene carbon atoms (not the attached functional groups) were fixed to prevent graphene sheet distortion and separation, as well as to maintain the correct inter-planar distances. VE resin monomers (styrene, VE1 and VE2) were randomly packed around the oxidized graphene sheets to fill the cell, yielding a final simulation cell density of 1.18 g/cm^3 (Figure 3.6b). This density corresponds to an experimental value determined previously [Nouranian *et al*., 2011]. The total number of atoms (resin plus the graphene sheets) was 17,141. Resin monomers, the number of each monomer molecule in the cell, molecular masses, and weight percentages are given in Table 3.2.

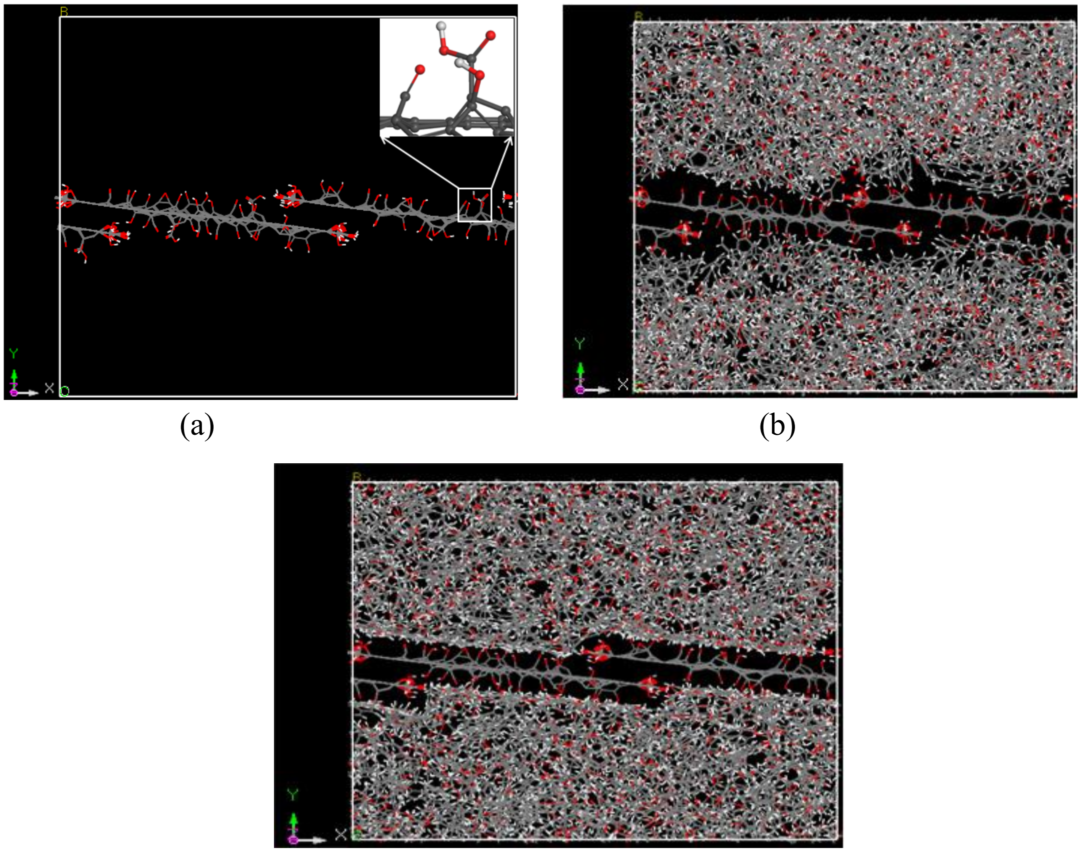

(a)

(b)

(c)

Figure 3.6 (a) View of stacked oxidized graphene sheets as an idealized model for the surface of an oxidized VGCNF. (b) The periodic simulation cell randomly packed with liquid VE resin monomers. (c) Final frame after ~15 ns of dynamics simulation.

Table 3.2 Resin composition in the simulation cell.

Resin[a] monomer	**Number of molecules**	**Molecular mass (au)**	**wt%**
VE1[b]	35	512.599	18.1
VE2[c]	61	796.954	49.0
Styrene	314	104.152	32.9

[a] This vinyl ester resin was based on Derakane 441-400 with $n = 1.62$ (n is the number of bisphenol-A groups in the dimethacrylate's backbone).
[b] The dimethacrylate with $n = 1$.
[c] The dimethacrylate with $n = 2$.

3.4.2 Dynamics Simulations

The Condensed-Phase Optimized Molecular Potentials for Atomistic Simulation Studies (COMPASS) force field was used in this study [Sun 1998]. This force field is widely used for inorganic and organic materials [Bunte and Sun 2000, McQuaid *et al.*, 2004, Rigby *et al.*, 1997, Zhao *et al.*, 2007]. The system was first partially relaxed using the Conjugate Gradient method (the Polak-Ribiere algorithm) for 10,000 iterations. MD simulations were then performed with an NVT ensemble (constant number of atoms, N; constant volume, V; and constant temperature, T). An NPT ensemble (constant pressure, P) was not used since position constraints were placed on the graphene sheets. Use of an NPT ensemble in the simulations would have led to unrealistic out-of-plane sheet distortions. Temperature was controlled by the Anderson thermostat.

A schematic of the simulation steps is shown is Figure 3.7. The simulation started at a temperature of 10 K and was run for 1 ps with a time step of 0.5 fs. This time step was used throughout all subsequent simulations. Next, the temperature was increased to

50 K, and then to 1000 K in 50 K increments. The dynamic simulations were run for 1 ps at all intermediate temperatures up to 1000 K except at 300 and 600 K, where it was run for 100 ps. The dynamics simulation was carried out at 1000 K for 10 ns to achieve system equilibration. Next, the system was cooled to 300 K using two distinct cooling protocols: 1) 10 K decrements (designated as C1) and 2) 50 K decrements (C2). In both cooling procedures, 1 ps dynamics simulations were run at each intermediate temperature. After cooling, the system was re-equilibrated at 300 K through 5 ns of dynamics simulation.

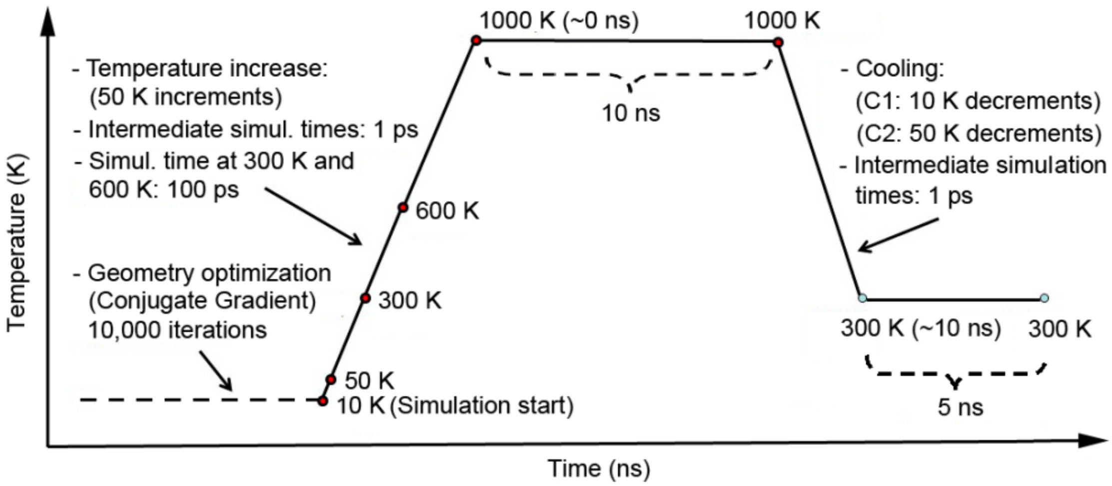

Figure 3.7 Schematic of the simulation steps.

The nearest distance between the atoms on the opposite sides of the graphene sheets is ~7 Å. This is less than the 9.5 Å van der Waals cut-off distance used in the simulations. Therefore, some monomer-monomer, monomer-functional group, and functional group-functional group interactions may occur through the graphene sheets.

These could slightly influence the calculated VE1, VE2, and styrene molar ratios adjacent to the oxidized graphene surface. Polar and nonpolar interactions are inversely proportional to the third and sixth powers of the separation distance between the groups, respectively. Therefore, VE1 and VE2 molecules are affected more by the interactions through the graphene sheets than styrene [Nouranian *et al*., 2011]. This effect, though minor, will be probed in future work. Figure 3.6c shows the final snapshot of the simulation after a total simulation time of ~15 ns following the C1 cooling procedure (10 K decrements). As can be seen in this figure, monomers completely wet the graphene surface.

3.5 Results and Discussion

The monomer distribution as a function of distance from the graphene sheets was analyzed by dividing the simulation cell into fifty 1 Å thick slabs lying parallel to the *xz* plane (Figure 3.6). Then, the dimensionless relative concentration of a monomer's atoms within a given liquid slab or sub-volume was used to define the molar ratio distribution of resin monomers at the carbon nanofiber-resin interface and in the direction roughly perpendicular to the graphene sheets (*y*-direction in Figure 3.6) [Nouranian *et al*., 2011]. The relative concentration expresses the molar ratios of styrene, VE1 and VE2 in a given slab volume divided by that same molar ratio present in the entire liquid resin. This relative concentration was defined as:

—— —— (3.1)

where C is the relative concentration, N_{slab} is the number of monomer atoms in the slab volume, V_{slab} is the slab volume, N_{tot} is the total number of monomer atoms in the liquid resin, and V_{tot} is the total liquid resin volume in the simulation cell. Thus, a relative concentration of 1.0 within any slab means that the ratio of the three monomers (styrene, VE1, and VE2) in that slab is identical to the molar ratio of these three monomers within the total liquid resin volume in the simulation cell.

The monomer equilibrium distribution was reached during successive MD simulations. The equilibration typically requires long simulation times at lower temperatures. Therefore, the temperature was increased to 1000 K to accelerate the equilibration process in this study (Figure 3.7). The simulations at 1000 K were run for 10 ns and time-averaged monomer concentration profiles at this temperature were used to establish system equilibration. The relative monomer concentrations were determined after each 50 ps of MD simulation and averaged over each successive 2 ns time interval to eliminate the normal data fluctuations about the equilibrium relative concentrations [Nouranian *et al.*, 2011]. Figure 3.8a shows the time-averaged styrene concentration profiles at 1000 K during the last 4 ns of the 10 ns simulation (Figure 3.7), after the monomer distributions had equilibrated. The relative monomer concentrations go to zero in the domain 22 Å < y < 25 Å, where the graphene sheets lie. The two time-averaged concentration profiles are essentially the same, showing the system has reached equilibrium, since no appreciable change in the relative concentrations is evident apart from inherent MD fluctuations [Nouranian *et al.*, 2011]. Note that the styrene concentration profile is nearly symmetric about the mid-plane of the simulation cell (Figure 3.8a). Since resin monomers only wet the outermost graphene layer of a real carbon nanofiber, the relative styrene concentration profiles were spatially averaged over both sides of the idealized graphene sheets (Figure 3.8b). Again, the two time-averaged profiles closely matched, indicating the system had equilibrated. Similar concentration profiles for VE1 and VE2 monomers were also generated in this fashion.

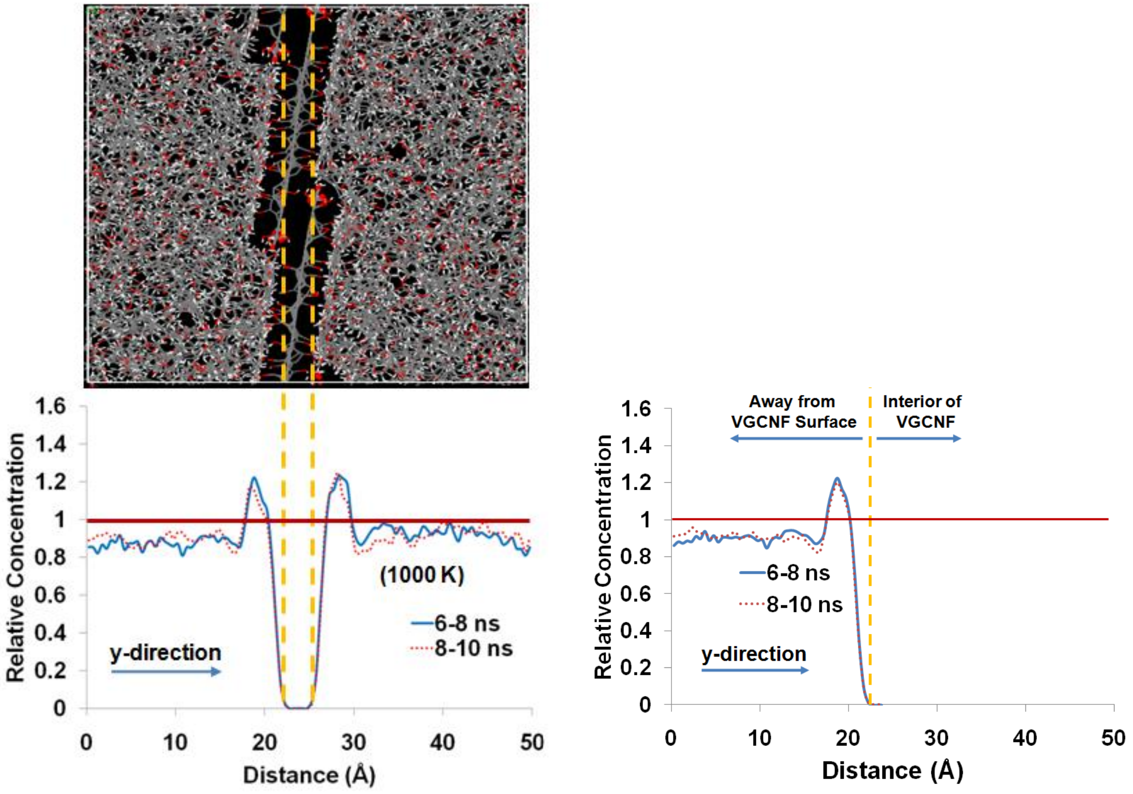

(a) (b)

Figure 3.8 (a) Time-averaged styrene concentration profiles along the y-coordinate of the simulation cell at 1000 K. (b) Temporally and spatially averaged styrene concentration profiles at 1000 K.

Once equilibration was reached at 1000 K, the system was cooled to room temperature (300 K) using cooling procedures C1 (10 K decrements) and C2 (50 K decrements) to investigate the effect of cooling rate on the monomer concentration profiles and system re-equilibration at 300 K. The temporally and spatially averaged monomer concentration profiles were again used to establish the system equilibration. Figure 3.9a shows the styrene concentration profiles obtained over successive 2 ns time intervals during the last 4 ns of the 5 ns simulation at 300 K following cooling procedure C1. The two concentration profiles closely matched, suggesting equilibrium was reestablished at the lower temperature. In order to minimize random fluctuations about the room temperature equilibrium concentration profile, subsequent equilibrium concentration profiles were based upon a temporal average over the entire 5 ns simulation at 300 K. The two cooling procedures only had a minor impact on the equilibrium monomer concentrations at 300 K. For example, Figure 3.9b shows the time-averaged styrene concentrations profiles obtained after following cooling protocols C1 and C2. The essential character of the two profiles was the same. Since the concentration profiles obtained following the two cooling procedures represent two equally valid characterizations of the system's equilibrium state, the two concentration profiles were averaged together. Such an approach is consistent with the ergodic hypothesis. All concentration profiles presented in the remainder of this study were determined in this fashion.

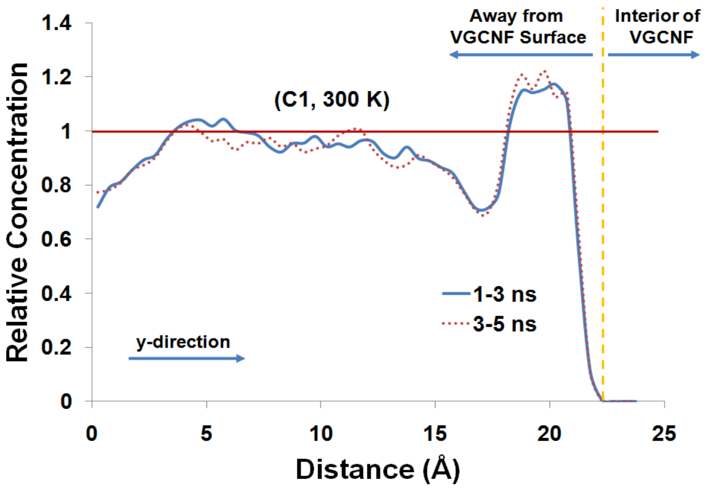

(a)

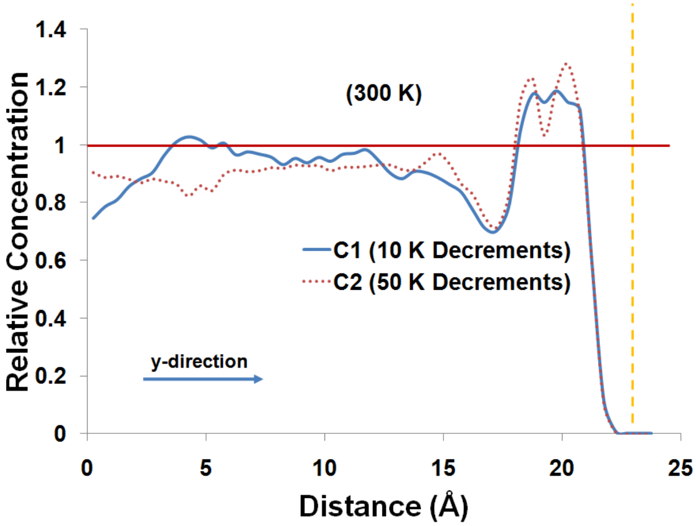

(b)

Figure 3.9 (a) Temporally and spatially averaged styrene concentration profiles over the last 4 ns of 5 ns simulations at 300 K for simulations following cooling procedure C1. (b) Styrene concentration profiles time-averaged over 5 ns simulations at 300 K following cooling procedures C1 and C2.

Figure 3.10a contains the equilibrium concentration profiles for styrene, VE1, and VE2 monomers. At distances far from the VGCNF surface, the relative concentrations for the three monomers were consistent with that of the bulk resin. Near the nanofiber surface, however, the relative concentrations of all three monomers showed significant spatial variations in a ~5-10 Å thick region surrounding the oxidized graphene sheets (Figure 3.10). For example, the styrene concentration was about 1.2 times that of the bulk resin in the near surface region. This is in contrast to a value of 1.4 reported near the surface of a pristine VGCNF [Nouranian *et al.*, 2011]. The VE1 concentration was also slightly greater than 1.2 times its bulk value at about 3 Å from the surface. If these ratios are mostly retained during the radical-initiated addition polymerization of the resin, an interphase region would form. Such a matrix region will have distinct mechanical properties from that of the bulk matrix due to a different network structure.

To better illustrate and interpret the variations in the relative monomer concentrations as a function of distance from the graphene surface, their ratios were calculated, i.e., styrene/VE1, styrene/VE2, and VE1/VE2 (Figure 3.10b). The styrene/VE1 ratio showed an increase near the oxidized graphene surface, which was ~2.4 times that of its bulk value. The relative styrene/VE2 ratio exhibited a peak of ~2.7 near the surface (Figure 3.10b). As a consequence, a surplus of styrene relative to the sum of VE1 and VE2 exists near the surface. The VE1/VE2 ratio was also higher in this region, indicating that more VE1 accumulates near the graphene surface than VE2. Overall, both styrene and VE1 concentrations were enhanced near the oxidized graphene surface. This could have repercussions for interphase formation in the cured composite.

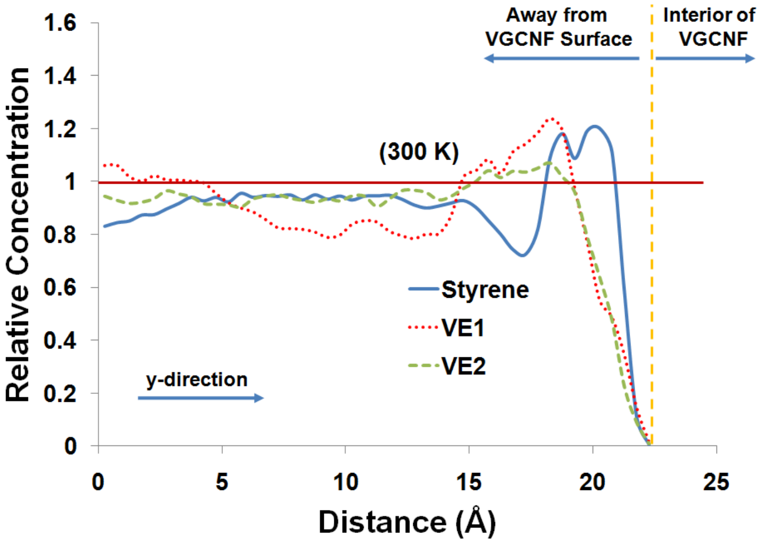

(a)

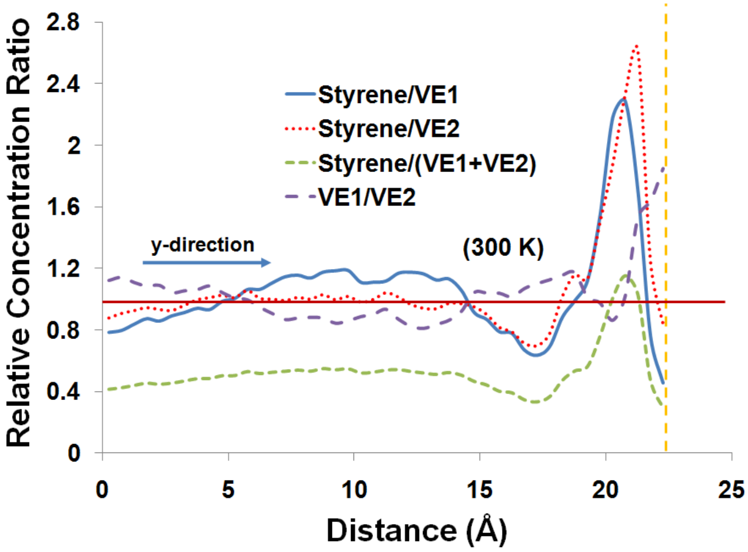

(b)

Figure 3.10 (a) Temporally and spatially averaged monomer concentration profiles at 300 K. These were averaged over the two simulations that used cooling procedures C1 and C2. (b) Relative monomer concentration ratios at 300 K based on averaged relative concentrations in (a).

The relative monomer distributions (concentration profiles) near the oxidized surface were profoundly different than those for a pristine (unoxidized) VGCNF

[Nouranian *et al.*, 2011]. To illustrate these differences, the relative concentration ratios of styrene/VE1, styrene/VE2, and VE1/VE2 were compared for both oxidized and pristine VGCNF surfaces (Figures 3.11-3.13). For example, the styrene/VE1 ratio near the oxidized graphene surface is substantially lower than that for a pristine surface (Figure 3.11). This indicates that less styrene (hydrophobic constituent) and more VE1 (polar constituent) accumulate near the oxidized nanofiber surface. In contrast, the styrene/VE2 ratio near the nanofiber surface is slightly higher for the oxidized case (Figure 3.12). This shows that less VE2 accumulation occurs near the oxidized surface than for a pristine graphene surface since more of the highly polar VE1 molecules are present near the oxidized graphene and compete for polar surface sites. The VE1/VE2 ratio is larger near the oxidized graphene surface than for a pristine surface (Figure 3.13), suggesting again that VE1 is enriched and VE2 is depleted in this region.

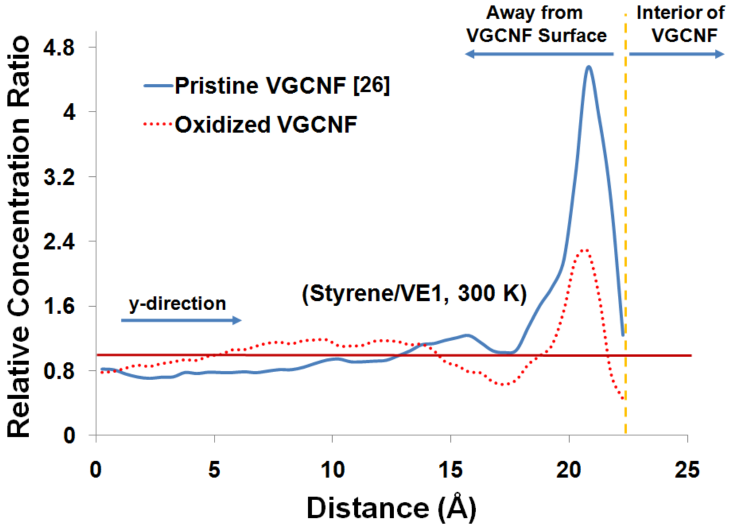

Figure 3.11 Relative styrene/VE1 concentration ratios at 300 K along the y-coordinate of the simulation cell for pristine [Nouranian *et al*., 2011] versus oxidized graphene sheets.

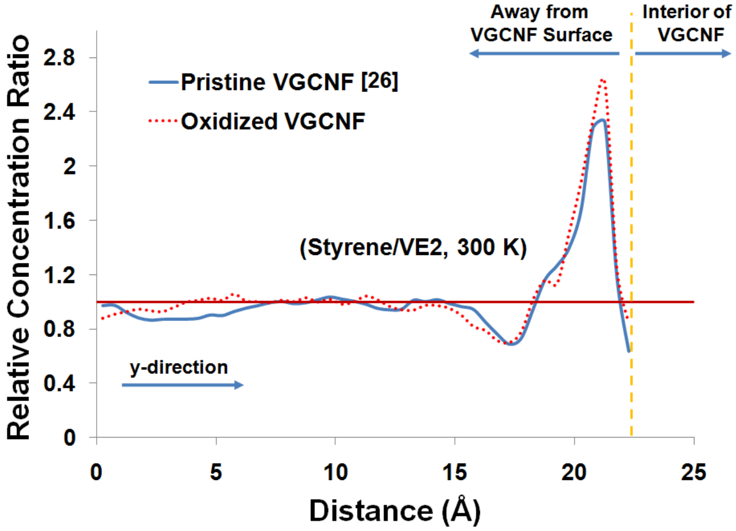

Figure 3.12 Relative styrene/VE2 concentration ratios at 300 K along the y-coordinate of the simulation cell for pristine [Nouranian *et al*., 2011] versus oxidized graphene sheets.

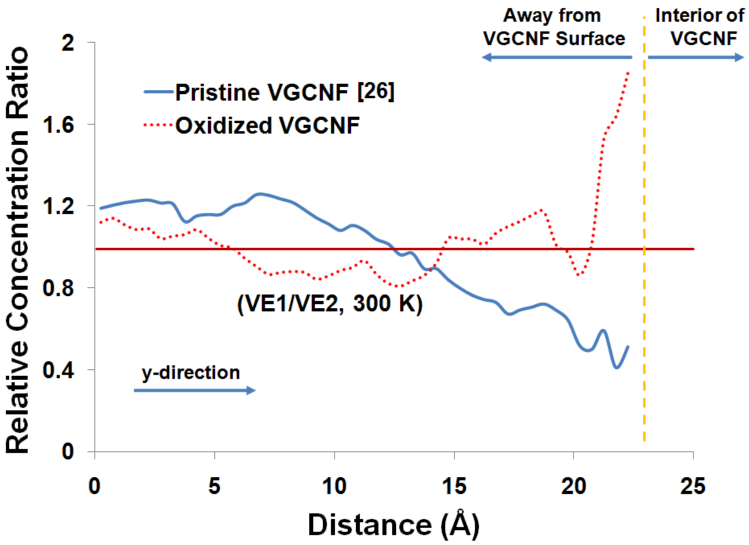

Figure 3.13 Relative VE1/VE2 concentration ratios at 300 K along the y-coordinate of the simulation cell for pristine [Nouranian *et al*., 2011] versus oxidized graphene sheets.

Overall, both styrene and VE1 accumulate, in higher concentrations than their bulk value, near the oxidized graphene surface (Figure 3.10a). This relative styrene concentration (~1.2 in Figure 3.10a) is less than that near the pristine graphene surface (~1.4 in [Nouranian *et al*., 2011]). The styrene accumulation at the oxidized graphene occurs in the unoxidized regions of its basal planes. The VE1 relative concentration is also higher near the oxidized surface than the bulk value (Figure 3.10a), in contrast to its depletion near the pristine surface [Nouranian *et al*., 2011]. Clearly, using oxidation to change the graphene surface chemistry plays a key role in nanofiber-liquid monomer interfacial interactions, leading to different monomer molar ratios and concentrations in the region 5-10 Å from these surfaces. This should have consequences for the cured composites.

More VE1 (Figure 3.13) in the cured network structure in the interphase at the oxidized nanofiber surface would enhance the crosslink density, which implies a stiffer matrix near the VGCNF surface than that of the bulk. Hence, the interphase adjacent to an oxidized graphene surface would be stiffer than that predicted at a pristine surface [Nouranian *et al*., 2011].

Strong polar interactions and hydrogen bonding between the surface oxygen-containing functions and the oxygen functions in VE1 and VE2 promote carbon nanofiber-matrix interfacial adhesion and better interfacial shear strength. Note that only a portion of the oxidized graphene surface displays oxygenated groups. Substantial portions of the surface are non-polar graphene, which interact with styrene and to a smaller degree with the aromatic rings in VE1 and VE2. This mildly oxidized (O/C = 0.020) VGCNF surface has strongly perturbed the styrene/VE1/VE2 amounts adjacent to the surface. If the degree of surface oxidation was increased, the near surface monomers ratios would be further changed. One might expect that substantially higher O/C VGCNF surfaces would attract less styrene and perhaps more of both VE1 and VE2. In the future, graphene (idealized VGCNF) surfaces with various functional groups present at different surface concentrations will be studied in a crosslinked VE matrix using graphene sheet pull-out simulations. These will give estimates of the interfacial shear strength.

Figure 3.14 shows the final distribution of styrene and VE1 monomers in the simulation cell for both oxidized and pristine graphene surfaces. Styrene molecules align their phenyl rings and vinyl group planes with the non-functionalized regions of the oxidized graphene sheets (Figures 3.14a and 3.15a). This was also found for the pristine carbon nanofiber surfaces [Nouranian *et al*., 2011] (Figure 3.14b). The styrene phenyl rings were found stacked both directly eclipsing graphene rings and in off-set (Figure 3.15a) configurations. The alignment of styrene parallel with the graphene ring structure is due to favorable π-π stacking interactions. These interactions could also exist between the phenyl rings of both VE1 and VE2 bisphenol-A backbones and graphene. However the -C(CH_3)$_2$- group between two phenyl rings sterically inhibits these rings from lying flat on the surface (Figure 3.15b). This is a consequence of the tetrahedral (*sp*^{3}-hybridized) carbon geometry connecting the phenyl rings. Furthermore, VE1 interacts with the oxygen-containing functional groups on both the surface and edges of the oxidized graphene sheets through its hydroxyl and ester groups. These interactions result in an increased VE1 concentration near the graphene surface (Figure 3.13). Since the concentration of functional groups on the graphene edges is higher than the graphene surface, more VE1 molecules accumulate in this region (circled parts of the graphene surface in Figure 3.14c). Depletion of VE1 near the pristine graphene surface is evident in Figure 3.14d [Nouranian *et al*., 2011].

VE2 interacts also with the oxidized graphene surface similar to VE1. However, its concentration near the surface is lower than that in the bulk region (Figure 3.13), presumably because VE1 is more polar than VE2. Both VE1 and VE2 have two hydroxyls and two methacrylate ester groups. Oxygen represents a higher weight fraction of VE1 (23%) than that of the VE2 monomer (20%). Thus, polar interactions with the functional groups on the graphene sheets favor a higher VE1 surface concentration than that of VE2 (in the oxygenated surface regions). Of course, it is the difference in the sum of all interactions of each monomer in the bulk liquid that is compared to all interactions of a monomer at the surface, with both the surface and surrounding monomers, that establishes the driving force of the equilibrium. As a result, the VE1 relative concentration at equilibrium is enhanced at the surface of the oxidized graphene sheet.

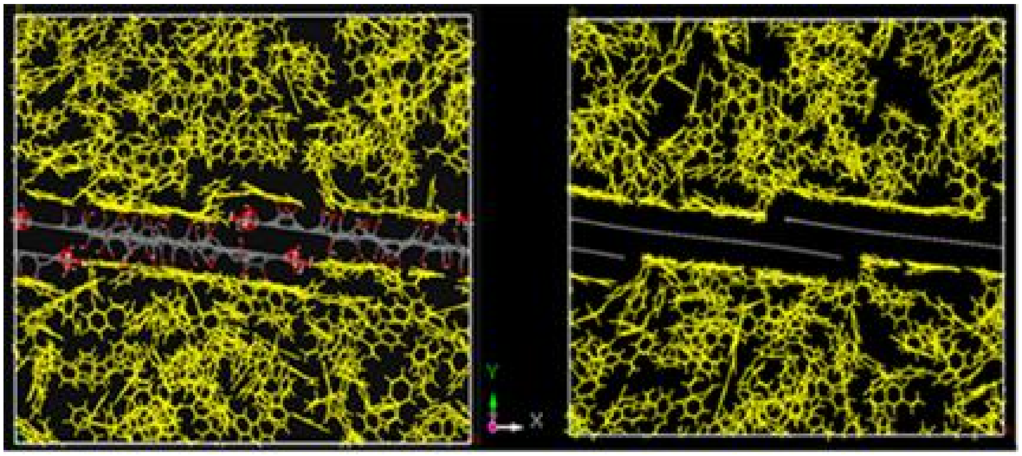

(a) Styrene/oxidized surface (b)Styrene/pristine surface

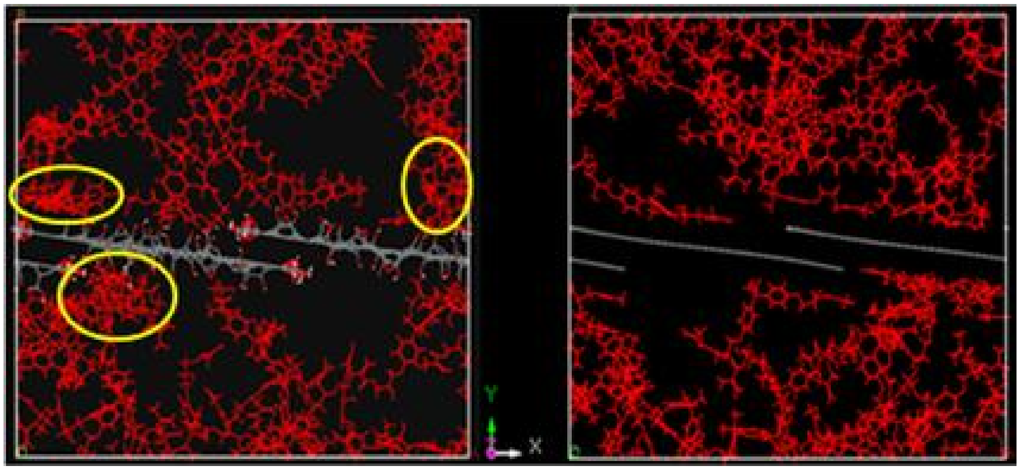

(c) VE1/oxidized surface (d) VE1/pristine surface

Figure 3.14 The final distributions of styrene (a and b) and VE1 (c and d) monomers for oxidized (left) versus pristine [Nouranian *et al.*, 2011] (right) graphene surfaces. Regions of high VE1 concentration near the oxidized graphene surface are marked in (c).

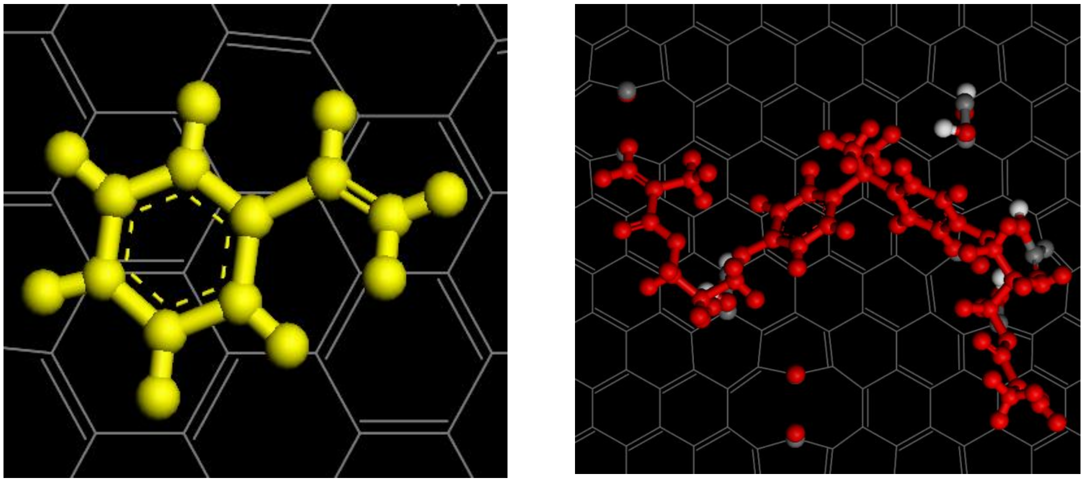
(a) (b)

Figure 3.15 (a) Top view of a styrene molecule aligned parallel to the oxidized graphene surface in an off-set configuration to optimize π-π stacking interactions. (b) A VE1 molecule with its two phenyl rings tilted versus the plane of the oxidized graphene surface due to the presence of two methyl groups on the carbon atom joining these rings and its tetrahedral geometry.

3.6 Conclusions

For the first time, oxidized vapor-grown carbon nanofiber (VGCNF)-liquid vinyl ester (VE) monomer interfacial interactions were studied for a realistic mixture of monomers in contact with a nanofiber surface using molecular dynamics (MD) simulations. The equilibration of a three-component liquid VE resin led to a monomer gradient near the idealized VGCNF surface (shingled graphene sheets). The concentrations of the most hydrophobic constituent (styrene) and the most polar one (VE1) were both enhanced near the oxidized graphene surface giving rise to a ~5−10 Å thick surface layer with different monomer molar ratios than those of the bulk resin. The composition of this layer was different for the oxidized graphene surface than that for a pristine (unoxidized) graphene surface studied previously [Nouranian *et al.*, 2011]. The oxidized graphene surface attracted styrene through monomer interactions with the unoxidized surface regions on the otherwise functionalized surface, but the relative concentration of styrene near the surface was less than that of the pristine graphene [Nouranian *et al*., 2011]. Moreover, VE1 accumulated near the oxidized graphene surface, which did not occur near the pristine surface. Assuming that the local monomer molar ratios will be retained near the oxidized graphene surface during resin curing, this could lead to a very thin interphase region in the cured composite with crosslinked network structure distinct from that near a pristine graphene surface. Hence, a stiffer interphase may be formed for composites made with oxidized VGCNFs.

Moreover, the different monomer compositions of the cured resin at the oxidized and pristine nanofiber surfaces would result in different interfacial adhesive bonding. Increased polar interactions between the matrix and the oxidized VGCNFs promote higher interfacial adhesion, particularly as the number of interactions between VE1 and oxidized surface groups increase. This could increase the interfacial shear strength compared to that for a pristine VGCNF, where only nonpolar matrix-carbon nanofiber interactions are present.

This technique for pre-equilibrating monomer mixtures before resin crosslinking can be extended to any specific surface (functionalized or not). MD simulations utilizing this technique will provide insight into the design of nanoreinforcement/matrix interfaces with improved adhesion. Future MD simulations will reflect monomer molar ratios found near both oxidized and pristine VGCNF surfaces in crosslinked VE network structures formed during curing. A novel crosslinking algorithm will be employed, where monomer regioselectivity (head-to-tail chain growth) and monomer relative reactivity ratios are accounted for in the free radical polymerization. Furthermore, interfacial shear strengths in VGCNF/VE nanocomposites will be calculated by VGCNF pull-out simulations from crosslinked VE matrices containing interphases. These studies may facilitate multiscale materials design by providing insight into molecular level nanofiber-matrix interactions leading to improved macroscale composite properties.

This work strengthens the important concept that liquid structure is sensitive to an interface only very close to that interface. The liquid monomer structure in this work reaches that of the bulk within very short distances (~ 5-10 Å) from the interface [Stiopkin *et al.*, 2011]. This generalization has recently been proved for pure water at the air-water interface, where water's structure reaches that of the bulk within 3 Å of this interface. Thus, the water "memory effect" [Ball 2007, Dayenas *et al.*, 1988] and the notion that long-range order can be induced in water by an interface are now unacceptable [Jungwirth 2011, Zheng *et al.*, 2006]. For our solution of nonpolar styrene and mildly polar VE1 and VE2, changes in the monomer ratio and liquid structure also only persist short distances (<10 Å) from the two interfaces studied. This result is consistent with the prevalent view that interphase formation is minimal in carbon fiber/thermoset resin composites.

3.7 Acknowledgement

This work was sponsored by the U. S. Department of Energy under contract DE-FC26-06NT42755. Special thanks go to William Joost, Department of Energy's technology area development manager.

3.8 References

Ashland Chemical Co., “Derakane 441-400 Vinyl Ester Resin Property Data Sheet.” http://www.ashland.com, 2011.

Ball, P., “Here lies one whose name was writ in water,” *Nature,* 2007, DOI:10.1038/news070806-6.

Bunte, S. W., Sun, H., “Molecular modeling of energetic materials: the parameterization and validation of nitrate esters in the COMPASS force field,” *Journal of Physical Chemistry B,* 2000, 104, 2477-2489.

Carneiro, O. S., Covas, J. A., Bernardo, C. A., Caldeira, G., van Hattum, F. W. J., Ting, J-M., *et al*., “Production and assessment of polycarbonate composites reinforced with vapor grown carbon fibers,” *Composite Science of Technology,* 1998, 58, 401-407.

Chávez-Medellín, R., Sanchez, de Almeida Prado LA., Schulte, K., “Polyamide-12/functionalized carbon nanofiber composites: evaluation of thermal and mechanical properties,” *Macromolecular Materials and Engineering,* 2010, 295(4), 397-405.

Choi, Y-K., Sugimoto, K., Song, S-M., Gotoh, Y., Ohkoshi, Y., and Endo, M., “Mechanical and physical properties of epoxy composites reinforced by vapor grown carbon nanofibers,” *Carbon*, 2005, 43, 2199-2208.

Cho,i Y-K., Sugimoto, K., Song, S-M., and Endo, M., “Production and characterization of polycarbonate composite sheets reinforced with vapor grown carbon fiber,” *Composites Part A: Applied Science and Manufacturing,* 2006, 37(11), 1944-1951.

Ciprari, D., Jacob, K., and Tannenbaum, R., “Characterization of polymer nanocomposite interphase and its impact on mechanical propertie,” *Macromolecules* 2006, 39(19), 6565-6573.

Dayenas, E., Beauvais, F., Amara, J., Oberbaum, M., Robinzon, B., Miadonna, A., *et al*., “Human basophil degranulation triggered by very dilute antiserum against IgE,” *Nature,* 1988, 333, 816-818.

Drzal, L. T., “The interphase in epoxy composites,” *Epoxy Resins and Composites II*, In: Dušek, K, Drzal, LT (eds.), *In Advances in Polymer Science,* Berlin, Germany: Springer; 1986, 75, 1-32.

Endo, M., Kim, Y. A., Hayashi, T., Yanagisawa, T., Muramatsu, H., Ezaka, M., *et al.*, "Microstructural changes induced in "Stacked Cup" carbon nanofibers by heat treatment," *Carbon*, 2003, 41, 1941-1947.

Faraz, M. I., Bhowmik, S., De Ruijter, C., Laoutid, F., Benedictus, R., Dubois, Ph., *et al.*, 'Thermal, morphological, and mechanical characterization of novel carbon nanofiber-filled bismaleimide composites," *Journal of Applied Polymer Science,* 2010, 117(4), 2159-2167.

Gao, W., Alemany, L. B., Ci, L. J., and Ajayan, P. M., 'New insights into the structure and reduction of graphite oxide," *Nature Chemistry,* 2009, 1(5), 403-408.

Hussain, F., Hojjati, M., Okamoto, M., and Gorga, R. E., "Review article: polymer-matrix nanocomposites, processing, manufacturing, and application: an overview," *Journal of Composite Materials,* 2006, 40(17), 1511-75.

Jancar, J., "Review of the role of the interphase in the control of composite performance on micro- and nano-length scales," *Journal of Material Science,* 2008, 43, 6747-6757.

Jancar, J., "Interphase phenomena in polymer micro- and nanocomposites," In: Karger-Kocsis, J, Fakirov, S (eds.). *Nano- and micro-mechanics of polymer blends and composites*. Cincinnati, OH: Hanser Publications; 2009: 241-266.

Jungwirth, P., "Physical chemistry: Water's wafer-thin surface," *Nature*, 2011, 474, 168-169.

Klein, K. L., Melechko, A. V., McKnight, T. E., Retterer, S. T., Rack, P. D., Fowlkes, J. D., *et al.*, Surface characterization and functionalization of carbon nanofibers. *Journal of Applied Physics,* 2008, 103(6), 061301-26.

Lakshminarayanan, P. V., Toghiani, H., and Pittman, Jr., C. U., "Nitric acid oxidation of vapor grown carbon nanofibers," *Carbon*, 2004, 42, 2422-2433.

Lee, S., Kim, M-S., and Ogale, A. A., "Influence of carbon nanofiber structure on properties of linear low density polyethylene composites," *Polymer Engineering and Science,* 2010, 50(1), 93-99.

Li, H., "Synthesis, characterization, and properties of vinyl ester matrix resins," Blacksburg VA USA, Virginia Polytechnic Institute and State Univ, PhD dissertation, 1998.

Li, J., Vergne, M. J., Mowles, E. D., Zhong, W-H., Hercules, D. M., and Lukehart, C. M., "Surface functionalization and characterization of graphitic carbon nanofibers (GCNFs)," *Carbon*, 2005, 43(14), 2883-2893.

McQuaid, M. J., Sun, H., Rigby, D., “Development and validation of COMPASS force field parameters for molecules with aliphatic azide chains,” *Journal of Computational Chemistry,* 2004, 25(1), 61-71.

Nouranian, S., Toghiani, H., Lacy, T. E., Pittman, Jr., CU., Dubien, J., “Dynamic mechanical analysis and optimization of vapor-grown carbon nanofiber/vinyl ester nanocomposites using design of experiments,” *Journal of Composite Materials,* 2010, DOI: 10.1177/0021998310385027.

Nouranian, S., Jang, C. W., Lacy, T. E., Gwaltney, S. R., Toghiani, H., and Pittman, Jr., C. U., “Molecular dynamics simulations of vinyl ester resin monomer interactions with vapor-grown carbon nanofiber and their implications for composite interphase formation,” *Carbon*, 2011, 49(10), 3219-3232.

Palmese, G. R., “Origin and influence of interphase material property gradients in thermosetting composites,” *Dissertation Abstracts International (USA),* 1992, 53(5), 362.

Ramanathan, T., Liu, H., and Brinson, L. C., “Functionalized SWNT/polymer nanocomposites for dramatic property improvement,” *Journal of Polymer Science Part B: Polymer Physics,* 2005, 43(17), 2269-2279.

Ramanathan, T., Abdala, A. A., Stankovich, S., Dikin, D. A., Hererra-Alonso, M., Piner, R.D., Adamson, D. H., *et al.*, “Functionalized graphene sheets for polymer nanocomposites,” *Nature Nanotechnology,* 2008, 3, 327-331.

Rasheed, A., Dadmun, M. D., and Britt, P. F., “Polymer-nanofiber composites: enhancing composite properties by nanofiber oxidation,” *Journal of Polymer Science Part B,* 2006, 44(21), 3053-3061.

Ren, X., Wang, X. Q., Sui, G., Zhong, W. H., Fuqua, M. A., and Ulven, C. A., “Effects of carbon nanofibers on crystalline structures and properties of ultrahigh molecular weight polyethylene blend fabricated using twin-screw extrusion,” *Journal of Applied Polymer Science,* 2008, 107, 2837-2845.

Rigby, D., Sun, H., and Eichinger, B. E., “Computer simulations of poly(ethylene oxide): force field, PVT Diagram and cyclization Behavior,” *Polymer International,* 1997, 44, 311-330.

Ros, T. G., van Dillen, A. J., Geus, J. W., Koningsberger, D. C., “Surface oxidation of Carbon nanofibers,” *Chemistry-A European Journal,* 2002, 8, 1151-1162.

Saber-Samandari, S., Afaghi Khatibi, A., “The effect of interphase on the elastic modulus of polymer based nanocomposites,” *Key Engineering Materials,* 2006, 312, 199-204.

Schadler, L. S., Brinson, L. C., and Sawyer, W. G., "Polymer nanocomposites: a small part of the story," *Nanocomposite Materials*, 2007, 50-58.

Stiopkin, I. V., Weeraman, C., Pieniazek, P. A., Shalhout, F. Y., Skinner, J. L., and Benderskii, A. V., "Hydrogen bonding at the water surface revealed by isotopic dilution spectroscopy," *Nature*, 2011, 474, 192-195.

Sun, H., "COMPASS: an ab initio force-field optimized for condensed-phase applications: overview with details on alkane and benzene compounds," *Journal of Physical Chemistry B,* 1998, 102(38), 7338-7364.

Tibbetts, G. G., Lake, M. L., Strong, K. L., and Rice, B. P., "A review of the fabrication and properties of vapor-grown carbon nanofiber/polymer composites," *Composite Science and Technology,* 2007, 67(7-8), 1709-1718.

Vaia, R. A., and Giannelis, E. P., "Polymer nanocomposites: status and opportunities," *Materials Research Society Bulletin,* 2001, 26(5), 394-401.

Zhao, L., Liu, L., and Sun, H., "Semi-ionic model for metal oxides and their interfaces with organic molecules," *Journal of Physical Chemistry C,* 2007, 111, 10610-10617.

Zheng, J. M., Chin, W-C., Khijniak, E., Khijniak, E. Jr., and Pollack, G. H., "Surfaces and interfacial water: evidence that hydrophilic surfaces have long-range impact," *Advances in Colloid and Interface Science,* 2006, 127, 19-27.

Zhou, Y., Pervin, F., and Jeelani, S., "Effect of vapor grown carbon nanofiber on thermal and mechanical properties of epoxy," *Journal of Material Science,* 2007; 42: 7544-7553.

Zhu, Y. A., Sui, Z. J., Zhao, T. J., Dai, Y. C., Cheng, Z. M., and Yuan, W. K., "Modeling of fishbone-type carbon nanofibers: a theoretical study," *Carbon*, 2005, 43, 1694-1699.

CHAPTER 4

A RELATIVE REACTIVITY VOLUME CRITERION FOR CROSSLINKING: APPLICATION TO VINYL ESTER RESIN MOLECULAR DYNAMICS SIMULATIONS

4.1 Abstract

Molecular dynamics simulations were performed to create a series of crosslinked vinyl ester resins. The crosslink density was varied at constant conversion. Thermodynamic and mechanical properties were calculated as a function of the crosslink density. A new relative reactivity volume (RRV) algorithm was developed to generate the crosslinking network by incorporating the correct regioselectivity (head-to-tail chain propagation) and monomer reactivity ratios. This is the first application of reactivity ratios for free radical addition polymerization in MD simulations. Prior crosslinking simulations were performed on step-growth epoxy resin curing. Vinyl esters studied here cure by free radical addition copolymerization. Crosslinked networks with double bond conversions up to 98% were achieved. Volume shrinkage, glass transition temperatures, and tensile elastic constants were calculated. Predicted Young's moduli were compared with experimental data. This RRV method can generate other thermoset and thermoplastic systems containing different monomers, and provide an approach for handling simultaneous irreversible reactions in MD simulations.

4.2 Introduction

Vinyl ester (VE) resins have costs and mechanical properties intermediate between polyester and epoxy resins. They are widely used in marine and chemical tank applications because of their high corrosion resistance and water barrier properties [Zhu *et al*., 2007, Karbhari 2004]. Fiberglass-reinforced VE materials have been used in airplanes, automobile control rods [Feraboli *et al*., 2011], and wind turbine blades [McConnell 2010]. Nanoreinforced VE polymer composites are increasingly used in structural applications because of the potential for significant mechanical property improvements [Guo *et al*., 2007]. The cure behavior of VE systems, however, can be affected by the presence of nanoreinforcements. A gradient in the monomer concentrations can develop adjacent to these surfaces, suggesting that during curing a very thin interphase region will form, which may influence nanofiber-resin interactions [Nouranian *et al*., 2011, Jang *et al*., 2011].

MD simulations have been reported for epoxy (i.e., EPON-862) resin crosslinking networks [Frankland *et al*., 2003, Qi *et al*., 2005, Doherty *et al*., 1998]. An atomistic simulation of an EPON-862/isophorone diamine network with only 900 atoms gave good mechanical property predictions [Wu and Xu 2006] (Young's modulus, bulk modulus, and Poisson's ratio) when the Condensed-Phase Optimized Molecular Potentials for Atomistic Simulation Studies (COMPASS) force field was used. Two simulations of EPON-862/DETDA with about 20,000 atoms have been reported that predicted thermal (glass transition temperature) [Varshney *et al*., 2008, Bandyopadhyay *et al*., 2011] and mechanical (Young's modulus) properties [Bandyopadhyay *et al*., 2011]. Unlike epoxy resins, VEs cure via a free radical chain addition polymerization mechanism where co-, ter- or tetrapolymerizations of different monomers proceed simultaneously. Free radical chain polymerizations are fundamentally different than step-growth polymerizations [Odian 1981]. Each initiation step in an addition polymerization typically adds hundreds of monomers to the chain (or network), typically in the hundreds, before termination and chain-transfer occurs. VE curing is complex because crosslinking occurs due to the presence of di- and trifunctional monomers. As chain growth and crosslinking progresses to a higher molecular weight, the mobility of the growing radical decreases, but monomer diffusion to the radical site continues at a rapid rate. Then as the crosslink density increases further, gelling begins and the rate of monomer diffusion within this gelling region drops. The relative rates of chain growth, termination and chain transfer begin to change in complex ways. Within a gelling region, termination reactions due to recombination can slow, leading to an increase in growing chain concentrations. This can produce autoacceleration of the rate.

A major complexity not previously handled with MD simulations of copolymerization or resin curing is the fact that growing chain ends react at different rates with different monomers [Brandrup and Immergu 1989]. Also, with different monomers present, different growing chain ends exist. The associated rate constants are functions of the free energies of activation and pre-exponential factors of the respective reactions. When two different monomers are present (for example, the styrene and methacrylate monomers present in VEs), the terminal polymerization model may be used to simulate the incorporation of each monomer into the forming polymer system [Odian 1981, Brandrup and Immergu 1989]. Assuming that the reactivity of a growing chain depends only on the reactivity of the end (terminal) monomer of the chain and not on the penultimate monomer or the chain length, the terminal polymerization model may be expressed as

$$\frac{d\mathrm{M}_1}{d\mathrm{M}_2} = \frac{\mathrm{M}_1\left(r_1\mathrm{M}_1 + \mathrm{M}_2\right)}{\mathrm{M}_2\left(r_2\mathrm{M}_2 + \mathrm{M}_1\right)} \tag{4.1}$$

For a typical VE diluted with styrene, M_1 represents the concentration of styrene molecules, and M_2 represents the concentration of VE dimethacrylate molecules for a styrene-containing VE resin. Here $r_1 = k_{11}/k_{12}$ and $r_2 = k_{22}/k_{21}$, and the rate constants (k_{11}, k_{12}, k_{22}, k_{21}) are for the chain growth step shown in Equations 4.2–4.5. Equation 4.1 can be integrated to predict the amount of each monomer consumed at any selected degree of conversion [Odian 1981, Brandrup and Immergu 1989]. Even when more than one type of dimethacrylate monomer is present, Equation 4.1 can still be applied when no important steric or electronic effects act to differentiate the methacrylate functions. In such cases, the polymerizing methacrylate functions and their reactivities are essentially the same.

$$\sim\!\sim \mathrm{Sty}^{\bullet} + \mathrm{Sty} \xrightarrow{k_{11}} \sim\!\sim \mathrm{Sty}-\mathrm{Sty}^{\bullet} \tag{4.2}$$

$$\sim\!\sim \mathrm{Sty}^{\bullet} + \mathrm{VE} \xrightarrow{k_{12}} \sim\!\sim \mathrm{Sty}-\mathrm{VE}^{\bullet} \tag{4.3}$$

$$\sim\!\sim \mathrm{VE}^{\bullet} + \mathrm{VE} \xrightarrow{k_{22}} \sim\!\sim \mathrm{VE}-\mathrm{VE}^{\bullet} \tag{4.4}$$

$$\sim\!\sim \mathrm{VE}^{\bullet} + \mathrm{Sty} \xrightarrow{k_{21}} \sim\!\sim \mathrm{VE}-\mathrm{Sty}^{\bullet} \tag{4.5}$$

The four reactions (Equations 4.2–4.5) determine the rate of incorporation of the two different monomer types in the terminal polymerization model. In Equations 4.2 and 4.3, ~~Sty• is a growing polymer chain ending in a styrene radical. Likewise, in Equations 4.4 and 4.5, ~~VE• stands for a growing VE radical chain end.

The actual values of the four rate constants (k_{11}, k_{12}, k_{22}, k_{21}) do not need to be known since they appear in Equation 4.1 as the relative reactivity ratios, $r_1 = k_{11}/k_{12}$ and $r_2 = k_{22}/k_{21}$. Only r_1 and r_2 are needed in the copolymerization equation to describe each type of monomer's incorporation into the polymer. An algorithm that reflects these rate constant ratios (r_1, r_2) for polymerizing the styrene and the dimethacrylate VE monomers is required to generate the correct monomer sequence distributions in the polymer at each point during conversion. Incorporating these r_1 and r_2 values is required to account for monomer drift during conversion and its effect on monomer sequence distributions in the polymer. The r_1 and r_2 values used in this work were $r_1 = 0.485$ and $r_2 = 0.504$ [Brandrup and Immergu 1989, Madruga *et al*., 1979]. When the values of r_1 and r_2 differ greatly, adequately accounting for monomer drift becomes increasingly important.

Free radical polymerizations also must be carried out in an MD simulation to give only head-to-tail regioselectivity during chain growth as illustrated in Figure 4.1. Thus, the algorithm used must also enforce this selectivity to achieve the correct molecular structure along the polymer chains. Head-to-head and tail-to-tail structures are found only as rare defects along styrene methacrylate copolymer chains. Thus, head-to-tail selectivity must be enforced in addition to relative reactivity ratios.

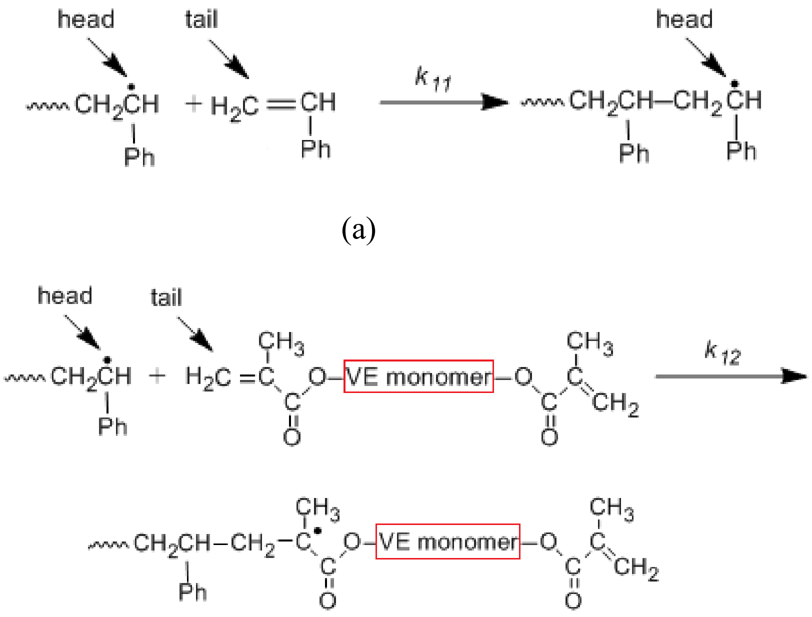

(a)

(b)

Figure 4.1 Head-to-tail regioselectivity during VE curing for a growing styrene radical adding to (a) styrene and (b) VE.

Bonds were formed between growing chain heads and new monomer tails only when found within specific nearby distances (i.e., close contact criteria were imposed). The value of $r_1 = k_{11}/k_{12} = 0.485$ shows that a growing chain ~~Sty$^\bullet$ radical's addition to a VE methacrylate monomer is faster than its addition to styrene. This was accounted for by allowing a larger reactive volume around the active growing chain's styrene head for finding a VE monomer tail than for finding a styrene tail. Such a relative reactivity volume (RRV) criterion defines when a new bond between a growing radical chain's head can be made to a new monomer during chain growth. If a given growing chain head is allowed to react with the tail of a VE or a styrene using the same close contact distance for the two monomer types, then the algorithm would define the reactivities of these two monomer types as identical. However, the reactivity of a VE monomer with the growing chain end ~~Sty• is slightly more than twice that of Sty reacting with a ~~Sty• (e.g., $r_1 = k_{11}/k_{12} = 0.485$). This can be accounted for by allowing a VE tail to react with ~~Sty• at a greater radial distance than for a styrene tail. Un-reacted monomers, hence their tails, exist in the volume surrounding a growing head. Thus, the distance at which a new bond is allowed to form is given as the radius of a sphere about the growing head. The radius of the spherical reactive volume (V_{11}) for ~~Sty• to the Sty tail will be less than that for ~~Sty• to the VE tail (V_{12}). Here the ratio of the two spherical reactive volumes are selected to be proportional to the associated relative reactivity ratio, i.e., $r_1 = k_{11}/k_{12} = V_{11}/V_{12} = 0.485$. This ensures that the *probability* of forming bonds between specific monomers will be consistent with the requisite reactivity ratios; this is a crucial feature of the RRV criterion developed in this work. The same approach was used for imposing $r_2 = k_{22}/k_{21} = V_{22}/V_{21} = 0.504$ on a growing VE head adding to a VE versus a styrene tail. Since a ~~VE• adds to styrene faster than to VE, the spherical volume and radius that defines where a ~~VE• to styrene bond can be formed, will be larger than that for ~~VE• adding to VE, the spherical volume and radius, which defines where a ~~VE• to styrene bond can be formed, will be larger than that for ~~VE• adding to VE. In addition, while using the RRV criterion, the proper regiochemistry was maintained by always requiring initiation to occur by only allowing a head to propagate by adding to a tail.

4.3 Uncrosslinked Molecular Models

The commercial Derakane 441-400 VE resin was used as the model resin in this study. The chemical structure of the two VE monomers used and their molecular models are shown in Figure 4.2. The average number of Bisphenol-A groups (n) in the dimethacrylate backbone of this resin is 1.62 [Li 1998]. Two specific vinyl ester monomers VE1 ($n = 1$) and VE2 ($n = 2$) were used in a mole ratio of 8/13 to account for the value of $n = 1.62$. A total of 89 monomers (3153 atoms) were used in the simulations, including 68 styrene, eight VE1, and 13 VE2 molecules. This ratio is equivalent to 33 wt% of styrene, which is the commercial resin's styrene composition.

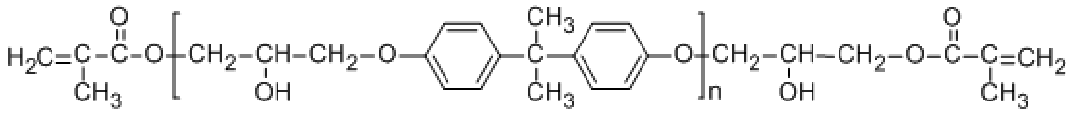

(a)

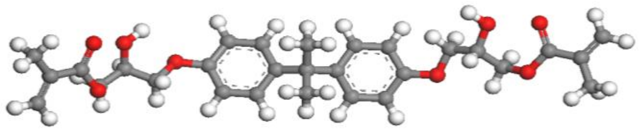

VE1 (*n* = 1)

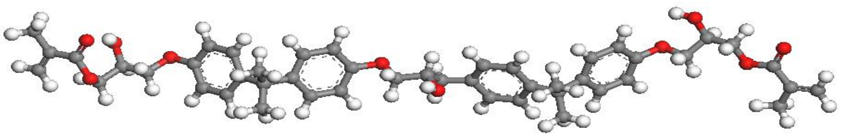

VE2 (*n* = 2)

(b)

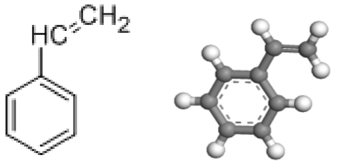

Styrene

(c)

Figure 4.2 (a) Chemical structures and molecular models of Bisphenol-A-based dimethacrylate vinyl ester resin components. (b) VE1 (*n* = 1), VE2 (*n* =2) and (c) styrene were generated with Material Studio v5.0.

4.4 Crosslinking Simulations

The formation of polymer networks has been simulated previously using MD, based on the early work of Leung and Eichinger [Leung and Eichinger 1984], which led to the development of commercial software to study structure and elasticity. In the work reported here, specific molecules are (randomly) packed with a density of 1.07 g/cc into a periodic simulation box as shown in Figure 4.3. The density of Derakane 441-400 liquid resin is 1.07 g/cc at room temperature. However, the curing reactions to form the crosslinked network were not conducted by a standard MD simulation approach, since the cure behavior of free radical polymerization is complex. Instead a reaction model was developed involving probabilistic algorithms. Monomer molecules in the simulated system are static at the points in the process where monomers are added to growing chains or crosslinking bonds are formed. Then after the bond is formed, the system is relaxed with an MD simulation. A capture radius is defined in which polymerization/crosslinking reactions are allowed to occur. This radius can be gradually increased as the curing reaction advances if required to reduce the computational intensity. In this study, MD simulations that generate the crosslinked resin from monomers do not consider reactions as having activation energies and passing over transition state energy barriers. Also, they do not require specific spatial orientations for a reaction to take place.

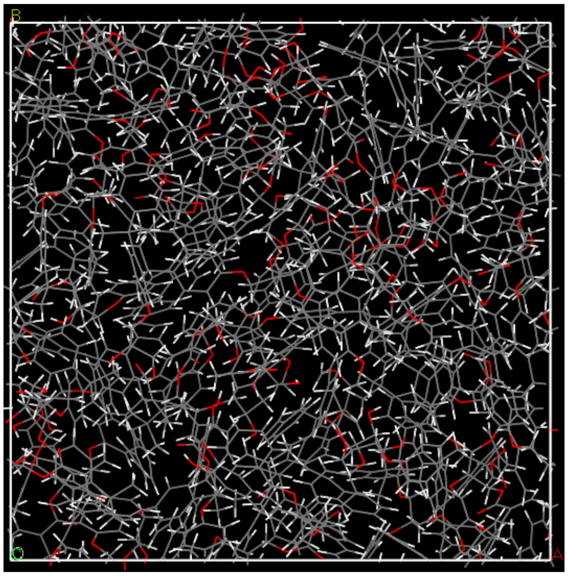

Figure 4.3 An initial 3D periodic unit cell is comprised of randomly packed VE1/VE2/styrene monomers at a 8/13/68 mole ratio with the density of 1.07 g/cc.

The crosslinking simulations considered two components of the real chain propagation reaction: 1) monomer reactivity ratios and 2) regioselectivity (head-to-tail chain growth) as shown in Scheme 4.1. These components were employed using the RRV criterion. In order to apply monomer reactivity ratios as reaction probabilities into the simulations, the relationship between the reactivity ratios and reaction cutoff distances are defined as described in Section 4.4.1.

4.4.1 Reaction Cutoff Distances Used to Enforce the Reactivity Ratios

Relative reactivity rate ratios (e.g., r_1 and r_2) are accounted for in the curing algorithm by enforcing these ratios as probabilities during the process of connecting monomers together during the simulation of resin curing. The reactivity ratios ($r_1 = 0.485$ and $r_2 = 0.504$) were taken from the literature [Madruga *et al.*, 1979]. The probability of a growing chain ~~Sty• reacting with a VE is about twice as large as the probability of ~~Sty• reacting with another styrene. To account for this effect, the volume which is searched for a VE monomer tail nearest to the ~~Sty• head should be about twice the search volume for the nearest styrene monomer's tail. The ratios of the search volumes should equal the reactivity ratios; this is the essential feature of the RRV criterion developed in this work. In practice, the search for a monomer tail to connect to the growing chain's head will seek a tail that is at a distance equal to or less than the radius which defines the search volume for that monomer. This distance is measured as the distance between the growing chain's head carbon and the nearby monomer's tail carbon, because it is these two atoms which will potentially become bonded. The relative radii used are derived from the reactive spherical volumes as described below, where radii are denoted using uppercase (R), and reactivity ratios are denoted using lowercase (r).

Let V_{11} be the spherical search volume for the ~~Sty• + Sty → ~~Sty–Sty• reaction with reactivity k_{11}. Similarly, let V_{12} be the spherical search volume for the ~~Sty• + VE → ~~Sty–VE• reaction with reactivity k_{12}. Noting that the volume of a sphere is given by $V = 4/3(\pi R^3)$ and $r_1 = k_{11}/k_{12} = V_{11}/V_{12} = 0.485$, then the RRV criterion requires that

$$V_{11} = \frac{k_{11}}{k_{12}} V_{12} \tag{4.6}$$

The radii of each search volume are related by

$$R_{11}^{3} = \frac{k_{11}}{k_{12}} R_{12}^{3} \tag{4.7}$$

$$R_{11} = \sqrt[3]{\frac{k_{11}}{k_{12}}} R_{12} = 0.786 \cdot R_{12} \tag{4.8}$$

where R_{11} is the ~~Sty• head to Sty tail reactive radius, and R_{12} is the ~~Sty• to VE tail reactive radius. So, the reaction cutoff distance for a ~~Sty• addition to a styrene monomer's tail is always 0.786 times that of the reaction cutoff distance for the ~~Sty• addition to a VE monomer's tail. The relative reaction cutoff distance for ~~VE• adding to the tail of a styrene versus the tail of a VE was calculated in the same manner. The reaction cutoff distance for ~~VE• adding to a VE tail is always 0.798 times the reaction cutoff distance of ~~VE• adding to styrene to allow for the faster ~~VE• addition to styrene. Such an algorithm forms the basis for the RRV cross-linking algorithm developed in this work.

It should be noted that Farah and Müller-Plathe *et al*[Farah *et al.*, 2010] reported an algorithm that used a characteristic delay time between successive reaction steps and a chain initiation capture radii combination in a homopolymerization modeling of linear polyester formation in a coarse graining approach.

4.4.2 Crosslinking Methods

Two general methods for simulating crosslinking were employed and compared. The first method (Method 1) involved growing several chains and then connecting their chain ends, head-to-tail, after growth. The second method (Method 2) grew a single chain to 98% conversion.

In Method 1, a chain was initiated, and chain growth was continued until growth slowed substantially. Then a new chain was started. When the growth of the second chain slowed, a third chain was initiated. This process was continued until 98% conversion was reached. Every growing chain had two reactive ends (a head and a tail) because the tail of the monomer at which the chain is started was not capped during chain growth. Ultimately, ten chains were grown leaving 20 chain ends (ten heads and ten tails) present at the end of this process. In contrast, only two chain ends would remain using the single chain growth of Method 2. The more chain ends that exist, the lower the crosslink density is. Therefore, in this first method, the chain end heads present after reaching 98% conversion were forced to progressively react with the remaining chain end tails. This was done by directly connecting a given head/tail pair followed by thermal relaxation. Thus, the number of chain ends was reduced stepwise from 20 to two at the end of the simulation. The last two chain ends were not connected in order to avoid excessive distortion of the polymer network associated with unrealistic final bond lengths.

The use of Method 1 (growing several chains) provides an opportunity to generate a series of resins with different crosslink densities at the same total conversion (98%), depending upon how many of the chain ends had been connected. The chain ends remaining after crosslinking was ended were always capped with hydrogen at the end of each crosslinked network formation (Figure 4.4). Mechanical properties were then computed for each cured resin in this series.

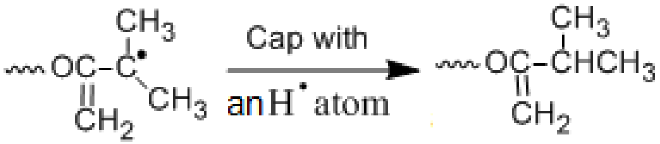

Figure 4.4 Capping an un-reacted chain end with hydrogen.

The second crosslink network formation technique (Method 2) employed the growth of a single chain only. Once chain growth initiation occurred, head-to-tail connections were formed progressively with the available monomers using the RRV criterion. Then the system was thermally equilibrated, allowing both monomer and growing chain diffusion to proceed. This realigned the monomer and growing head locations to permit further bond formation. Thus, further chain growth to the closest monomer tails within the defined spheres occurred. This process was repeated stepwise until 98% conversion was reached. This process will be described in more detail in Section 4.4.3. Method 2 (single chain growth) is computationally intensive because the diffusion process slows with increasing conversion due to the rising crosslinking density. Also, as the monomer concentration drops, the probability drops that a monomer tail will be found within the reactive spherical volumes around the growing heads. The final crosslinking structure at 98% conversion with two chain ends remaining is shown in Figure 4.5. Many chemical bonds are connected to the other neighboring cells (not visualized) across the cell boundaries, thus forming an extended periodic system.

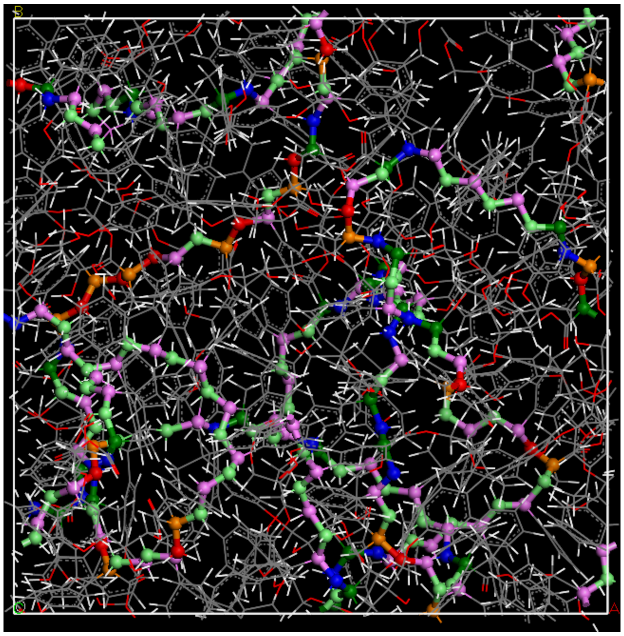

Figure 4.5 A crosslinked model of the VE resin system generated by single chain growth (Method 2) at 98% conversion where the two chain ends that remained were capped by hydrogen. (pink: styrene head, green: styrene tail, orange: VE1 head, red: VE1 tail, dark green: VE2 head, and blue: VE2 tail)

4.4.3 Crosslinking Procedures

The specific steps used to create the cured resin network by either Method 1 or 2 are now described.

4.4.3.1 Step 1

The uncrosslinked molecules (68 styrene, eight VE1, and 13 VE2) were randomly packed with a predefined density of 1.07 g/cc. Two different three dimensional periodic unit cells with 32×32×32 Å^3 (Figure 4.3) and 40.6×40.6×40.6 Å^3 were employed. This larger cell contained twice the number of monomer molecules of the smaller cell. A geometry optimization was performed for 10,000 iterations with the conjugate gradient method to initially relax the molecular structures and minimize the total energy of the system. Since the total of all the polymerizable double bonds was 110, there were a total of 220 carbon atoms to which carbon-carbon single bonds could be formed (at 100% conversion) during curing. Likewise, there were 220 double bonds and 440 carbon atoms in 40.6×40.6×40.6 $Å^3$ unit cell.

4.4.3.2 Step 2

Initiation of the cure was started by attaching a hydrogen atom to one tail atom of either a styrene or a VE in order to create a propagating free radical head. The monomer chosen to initiate chain propagation was randomly selected. The reactive styrene or VE tails within the predefined cutoff distances from the reactive head were then found. If either a styrene or a VE tail was present within their respective cutoff distances, a new bond was formed which also created a new reactive head.

4.4.3.3 Step 3

If more than one reactive tail atom was found within the reaction cutoff distances, the following procedure was followed. Scale factors (R_{11}/R_{12} = 0.786 and R_{22}/R_{21} = 0.798) were employed to adjust the radii of the spherical search volumes used to account for the relative reactivity ratios, as explained in Section 4.4.1. The scale factor was also applied to the calculated distances between the head atom and all the reactive tail atoms found within the adjusted cutoff distances. The smallest value of the *adjusted head to tail distance* was chosen to create a new bond. This chain propagation procedure forced the chemically required head-to-tail regioselectivity. Each time a polymerization reaction occurred, the new bond was analyzed, and all unrealistic bonds were manually eliminated. After breaking such a bond, the system was subjected to NVT and NPT re-equilibrations before new bonding was permitted to occur. One example of an unphysical bond would be a bond made between a head and tail that goes through a phenyl ring (e.g., “ring spearing”).

For an illustration, consider the case of crosslink formation between a ~~Sty$^\bullet$ and the nearest available styrene tail or VE tail located at distances R_{11} and R_{12}, respectively. Which monomer is selected to form the new bond? If R_{11} is greater than $0.786 \cdot R_{12}$, then a ~~Sty$^\bullet$ to VE bond is formed since k_{12} is greater than k_{11}. However, if the styrene tail falls within the VE cutoff radii (i.e., $R_{11} < R_{12}$), then the following criterion is employed (Scheme 3). If R_{11} is less than $0.786 \cdot R_{12}$, then a ~~Sty$^\bullet$ to Sty bond is formed. Conversely, if R_{11} is greater than $0.786 \cdot R_{12}$, then ~~Sty$^\bullet$ to VE bonding occurs. This ensures that the probability of bond formation is consistent with the relative reactivity ratios. A similar strategy was used to establish ~~VE$^\bullet$ to VE and ~~VE$^\bullet$ to Sty bonds using cutoff radii R_{22} and R_{21}, respectively. This is illustrated in Figure 4.6.

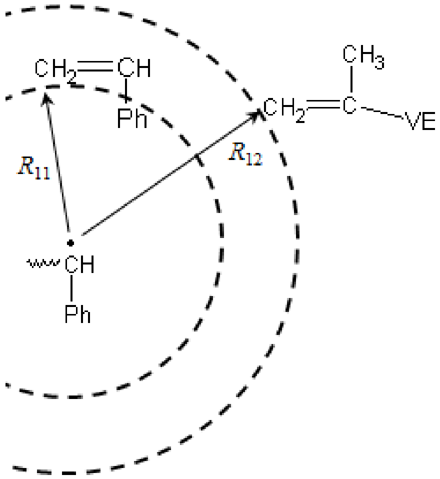

Figure 4.6 Selecting the monomer to react with ~~Sty•. When R_{11} is less than 0.786·R_{12}, a ~~Sty• to Sty bond will form. When R_{11} is greater than 0.786·R_{12}, a ~~Sty• to VE bond will form.

4.4.3.4 Step 4

When no monomer tail carbon atoms existed within the cutoff distances from the growing chain's head, the system was relaxed using 2,000 geometry optimization iterations, followed by NVT (constant number of molecules, volume, and temperature) and NPT (constant number of molecules, pressure, and temperature) simulations at 300 K, each lasting 50 ps and employing 1 fs time steps, for a total of 100,000 iterations. Next, the growing chain head was re-examined to see if a reactive tail was now present within the same cutoff distances used before to generate new bonds. If so, *Steps 2–3* were repeated.

4.4.3.5 Step 5

When no reactive tails appeared within the cutoff distances after the NVT and NPT relaxation cycles, the reaction cutoff distances were increased by 0.25 Å multiplied by the scale factors (0.786 and 0.798). Consider the case of R_{11}= 0.786R_{12}. When the R_{12} cutoff distance was changed from its current value of x to (x+0.25 Å), then the search radius was changed from R_{11} = 0.786x to R_{11} = 0.786(x+0.25 Å) to correctly account to correctly for the reactivity ratios. Next, *Steps 2–4* were repeated. Note that new chain initiation was randomly introduced only in Method 1 (see Section 4.4.2).

4.4.3.6 Step 6

Steps 2–5 were repeated until the system reaches a desired conversion or crosslinking density. Crosslinking was considered to be completed at this point, and all un-reacted growing chain radical heads were then capped with hydrogen atoms. This was shown for a growing VE• head in Figure 4.4.

4.4.4 Comparing crosslinking results using a larger repeating unit cell

A larger repeating unit cell (40.6×40.6×40.6 $Å^3$) was also used, which has exactly twice number of molecules than that of the smaller 32.2×32.2×32.2 $Å^3$ cell size. The single chain growth crosslinking method (Method 2) was employed in all simulations conducted when using this cell. The purpose of these simulations was to compare the volume shrinkage, glass transition temperature (T_g) and Young's modulus values to those predicted from the simulations of crosslinked network structures performed in the smaller cell. If both simulations led to comparable results, then the smaller cell could be reliably used to generate representative predictions.

All simulations were performed using the commercial molecular simulation module, Discover, from Accelrys [Accelrys]. The COMPASS force field [Sun 1998] was employed in this work. This force field is widely used for inorganic and organic materials [Bunte and Sun 2000, McQuaid *et al*., 2004, Rigby *et al*., 1997, Zhao *et al*., 2007]. The cured resins' elastic constants and densities were obtained from the cured equilibrated structures and compared with data supplied in the Derakane 441-400 VE resin experimental data sheet [Ashland Chemical Co. 2011] provided by Ashland Co.

One feature of the RRV algorithm is that the simulation is decoupled from the time scale of the experimental system. So, although MD simulations were done as part of the crosslinking procedure, the simulation time of the MD is not related to the actual time needed for real crosslinking to occur.

4.5 Results and Discussion

A crosslinked VE resin system was successfully generated with 98% of the double bonds consumed. Conversion is defined as the percent of the double bonds present that are consumed. Average chain lengths in styrene or methyl methacrylate free radical-initiated homo and copolymerizations are usually greater than 200 monomer units long. With only 89 monomers present in this study, a high conversion of the available carbon-carbon double bonds from a single initiation event would mimic the pattern of chain growth in real VE curing, where the initiator concentration is low, and the initiator is decomposing into initiating radicals over a period of time. Thus, a 100% or 98% conversion of 89 monomers represents a reasonable chain growth from initiation, although complete or 98% conversion is not obtained experimentally even with extended post curing. However, achieving 98% conversion from a single initiation event is computationally intensive since the simulation's progress slows as fewer monomers remain unreacted as crosslinking increases. Volume shrinkage, glass transition temperature, and tensile elastic constants of the equilibrated structures were analyzed.

4.5.1 Volume Shrinkage

Volume shrinkage occurs as a liquid VE resin is cured to a solid [Cao and Lee 2003]. Volume shrinkage was determined as a function of percentage conversion, as well as a function of crosslink density as chain ends were connected using the multiple growing chain Method 1 (Table 4.1). As monomers were incorporated throughout, the cure volume decreased (entries 1–4, Table 4.1). When conversion reached 98%, the volume continued to decrease as the number of chain ends was decreased by progressively connecting chain end heads to chain end tails at constant conversion (entries 4–10, Table 4.1). Derakane 441-400 VE resin was reported to shrink 7.5% after curing [Ashland Chemical Co. 2011]. The volume shrinkage computed during curing Method 1 curing was about 4.7% when 20 chain ends remained at a 98% conversion. After 18 of the 20 chain ends were connected by bonds (leaving two chain ends), generating a higher crosslink density, the volume shrinkage increased sharply to 7.8%. This value is only slightly higher than the experimental value. These volume contractions are listed in Table 4.1.

Table 4.1 Volume shrinkage during curing using multiple chains for growth (Method 1) as a function of conversion to 98% followed by increasing the crosslink density by progressively combining chain ends.

Conversion (%)	Number of Chain Ends	Volume (Å^3)	Volume Shrinkage (%)
Initial liquid system	—	33732.7	—
78	48	32749.1	2.9
86	30	32357.5	4.1
90	22	32262.5	4.3
98	20	32153.5	4.7
98	16	31959.7	5.2
98	12	31844.5	5.6
98	8	31805.2	5.7
98	4	31517.5	6.5
98	2	31101.5	7.8

The volume shrinkage was 8.8% (Table 4.2) when a single chain was grown to 98% conversion (Method 2) with two chain ends remaining. This difference in volume shrinkage using multiple chains (7.8%, Method 1) for curing followed by connecting chain ends versus using a single chain growth (8.8%, Method 2) is due to several factors. First, each particular crosslinking procedure will lead to a different crosslink pattern. The crosslinking process could be performed many times with different initial random monomer packings with the same density. Also, crosslinking could be repeatedly performed by starting the growing chains at different locations. The crosslink patterns resulting from each such calculation would be somewhat different, even when the conversion and number of chain ends were the same. Ideally, several such calculations could be made and averaged. Another approach would be to employ far more monomers in a larger repeating cell.

The two computed volume shrinkages (7.8, 8.8% listed in Table 4.2) obtained using Methods 1 and 2 at the same conversion (98%) and number of chain ends (two) are both somewhat higher than the experimental value (7.5% given by Ashland Co. for Derakane 441-400 [Ashland Chemical Co. 2011]). Note that the experimental curing will not reach 98% conversion, and real cured samples could contain some voids and defect sites. Furthermore, Method 1 links chain ends somewhat arbitrarily. If that linking were performed differently, small differences in mass density would occur. Finally, the absolute crosslink density of the experimental cure is not known. Hence, it is expected that the calculated volume shrinkages should be higher than the experimental value because (1) the crosslink density in the simulated structure is higher than in experimental resins, (2) the simulated conversion (98%) is greater than that obtained in experiments, and no voids and defects sites are present in this model.

Volume shrinkages obtained from simulations of the large repeating unit cell (6308 atoms) were compared to the simulations of the smaller repeating unit cell (3104 atoms). The crosslinking density of the large VE network structure containing four chain ends in the large unit cell is the same as the VE's crosslinking density with two chain ends in the small unit cell. As shown in Table 4.2, two computed volume shrinkages (8.8% and 8.4%) are very close to each other, suggesting that the smaller simulation box of size 32.2×32.2×32.2 $Å^3$ is sufficient to evaluate a homogeneous VE network structure. With only two chain ends present in the larger cell, which has twice the number of monomer molecules at the start, the crosslinking density at 98% conversion will be greater than that in the smaller cell when two chain ends remain. Thus, a greater shrinkage is expected. This was confirmed in the last entry in Table 4.2, where a 9.8% volume shrinkage was predicted.

Table 4.2 Acomparison of the volume shrinkage between the multiple chain growth (Method 1) and single chain growth (Method 2) at 98% conversion. Two representative unit cells were compared with 3154 and 6308 atoms present, respectively.

Curing Method	Final Number of Chain Ends	Initial Volume (Å^3)	Final Volume (Å^3)	Volume Shrinkage (%)
1	2	33732.7	31101.5	7.8
2	2	33732.7	30758.3	8.8
2[a]	4[b]	66955.7	61299.0	8.4
2[a]	2[b]	66955.7	60342.8	9.8

[a]These simulations were performed with a larger repeating unit cell containing 6308 atoms. [b]Two chain ends gives a higher crosslinking density in the larger repeating unit cell since twice as many monomers were present. Four chain ends result in the same crosslinking density as two chain ends given in the smaller unit cell containing 3154 atoms.

4.5.2 Glass Transition Temperatures

Glass transition temperatures (T_g) were obtained after performing 600 K annealing MD simulations. The crosslinked structures were heated to 600 K and then the constant pressure (NPT ensemble) simulations were performed for 200 ps to relax the structures. These equilibrated structures were cooled to 300 K at rate of 50 K/200 ps at atmospheric pressure by the Berendsen barostat method [Berendsen *et al*., 1984]. MD determinations of polymer glass transition temperatures are well described in the literature [Wu and Xu 2006, Bandyopadhyay *et al*., 2011, Zhang *et al*., 2007, Watt *et al*., 2004]. The polymer density is computed as a function of temperature. A change in the slope of the density versus temperature relationship occurs at T_g, because a series of segmental motions become activated. Density versus temperatures plots for three crosslinked systems, all at 98% conversion, are shown in Figure 4.7. Two plots are shown for resins cured by Method 1 with 20 chain ends and two chain ends. T_g occurs where the slopes intercept at 424 K for the resin cured by Method 1 with 20 chain ends (98% conversion). Increasing the crosslink density by reducing the number of chain ends to two resulted in $T_g = 426$ K. Finally, for the single chain growth cured resin (Method 2) with two chain ends $T_g = 420$ K, which is close to the values obtained using Method 1 (424 K, 426 K). The experimental value for Derakane 441-400 VE resin is $T_g = 410$ K [Ashland Chemical Co. 2011].

The calculated T_g values are not particularly sensitive to the crosslinking densities in these example resins. The glass transition temperatures for resins cured with both 20 and two chain ends structures are very similar at the same 98% conversion values. Ziaee *et al*. [Ziaee and Palmese 1999] showed that T_g values for post-cured VE systems were constant, regardless of which initial isothermal cure temperature was used. However, different initial cure conditions will influence the 3D polymer structure and conformations [Ziaee and Palmese 1999]. This implies that the glass transition temperature was most strongly affected by the final degree of conversion. Therefore, T_g may be more related to the degree of conversion than to the crosslink density.

Simulated final mass densities (at 300 K) for two chain ends computed by Method 1 (1.151 g/cc) and Method 2 (1.163 g/cc) were very close to the experimental value of 1.150 g/cc [Ashland Chemical Co. 2011]. Figure 4.7 illustrates that the more highly crosslinked resins (those with two chain ends) have higher mass densities and that their mass densities decrease more slowly as temperature rises, both above and below T_g. Increasing the crosslink density and decreasing the number of chain ends lowers the amount of free volume in the resin.

T_g values for the larger repeating unit cell were calculated with VE crosslinked structures containing both four chain ends and two chain ends as shown in Figure 4. The T_g value for the VE crosslinked structure with four chain ends (419 K) was very close to that for the cure with two chain ends in the smaller cell (420 K) computed by Method 2. These two structures have the same crosslinking densities. This further indicates that the smaller simulation cell (32×32×32 $Å^3$) was able to generate the properties of the homogeneous VE crosslinked network.

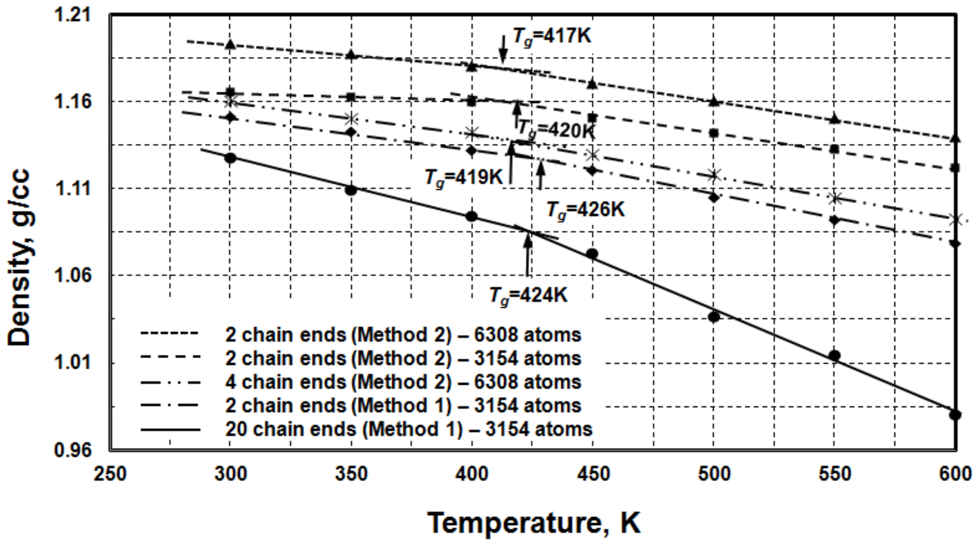

Figure 4.7 Glass transition temperatures (T_g) for cured VE resins simulated by Methods 1 and 2 at 98% conversion. T_g values from Method 1 with different crosslinking densities are very close to each other and also close to that predicted by Method 2. The experimental T_g for Derakane 441-400 VE resin is 410 K [Ashland Chemical Co. 2011]. Glass transition temperature (T_g) for the VE cured to four chain ends in a large repeating unit cell is also close to that of two chain ends in a smaller repeating unit cell simulated by Method 2. The crosslinking density of these two VE resins is the same.

4.5.3 Elastic Moduli for the Crosslinked VE

An energy minimization using the conjugate gradient method was employed with 1000 iterations to reduce the calculation time. The minimum derivative targeted was 0.1 kcal/Å. Then three tensile strains and three pure shear strains of magnitude ±0.0005 were independently applied to the minimized system and then another energy minimization step was performed. Finally, the internal stress tensor was used to obtain the elastic stiffness matrix. A static method [Wu and Xu 2006] based on MD was used to calculate the stiffness matrix using the second derivative of the potential energy (U) with respect to the components of the small strain tensor, i.e.,

$$C_{ij} = \frac{1}{V}\frac{\partial^2 U}{\partial \varepsilon_i \partial \varepsilon_j} \tag{4.9}$$

Here, C_{ij} are the components of the 6×6 elastic stiffness tensor, ε_i are the components of the small strain tensor, ($i, j = 1, ...6$), and Voigt notation is employed. From the calculated stiffness matrix, the Lame constants (λ, μ) for the cured VE structure can be determined, i.e,

$$\lambda = \frac{1}{3}\left(C_{11} + C_{22} + C_{33}\right) - \frac{2}{3}\left(C_{44} + C_{55} + C_{66}\right) \tag{4.10}$$

$$\mu = \frac{1}{3}\left(C_{44} + C_{55} + C_{66}\right) \tag{4.11}$$

The isotropic Young's modulus (E) for the crosslinked VE may be determined from the Lame constants [Wu and Xu 2006, Liu et al., 2011],

$$E = \mu \frac{3\lambda + 2\mu}{\lambda + \mu} \tag{4.12}$$

For illustration purposes, the stiffness matrix for a conversion of 98% crosslinked system with 20 chain ends developed by Method 1 is shown below.

$$[C] = \begin{bmatrix} 5.2710 & 2.6370 & 2.5260 & 0.2811 & 0.1181 & 0.0264 \\ 2.9300 & 6.8950 & 3.1980 & 0.3448 & 0.0699 & 0.2796 \\ 2.8190 & 2.9590 & 5.8940 & 0.2010 & -0.3511 & 0.0516 \\ 0.4690 & 0.5159 & 0.3425 & 1.4340 & -0.1230 & 0.0516 \\ 0.0359 & 0.2205 & -0.0527 & -0.1431 & 1.6170 & -0.0520 \\ -0.0659 & 0.1328 & -0.1691 & -0.0539 & -0.0646 & 1.3880 \end{bmatrix} \tag{4.13}$$

Using standard continuum mechanics arguments, the elastic stiffness matrix averaged over a representative volume element (RVE) will be both positive definite and symmetric. Here the RVE is defined as the minimum material volume necessary to provide a statistically homogeneous representation of the microstructure [Hill 1963]. This suggests that all continuum field quantities of interest (stress, strain, temperature, etc.) can be expressed as smoothly varying functions of spatial position. The RVE-averaged elastic stiffness matrix for cured VE should arguably be positive definite, symmetric ($C_{ij} = C_{ji}$), and isotropic ($C_{11} = C_{22} = C_{33}$; $C_{44} = C_{55} = C_{66}$; $C_{14} = C_{15} = C_{16} = C_{24} = C_{25} = C_{26} = C_{34} = C_{35} = C_{36} = C_{45} = C_{46} = C_{56} = 0$). Given the discrete character of MD simulations and practical limitations on the maximum number of monomer atoms leading to a tractable solution, the periodic repeating unit cell (RUC) used in MD does not correspond to an RVE. Hence, the calculated stiffness matrix will only loosely approximate isotropic bulk material behavior. For example, in Equation 4.13, C_{11}= 5.271 GPa $\neq C_{22}$, C_{25} = -0.05201 GPa $\neq C_{52} \neq 0$, etc. Interestingly, this slight lack of symmetry in [C] suggests a micropolar RUC-averaged constitutive response. In such a case, small distributed torques are induced throughout the RUC due to uniform displacements applied to the RUC boundaries. However, if the elastic stiffness matrices resulting from multiple crosslinking simulations (each with different initial realizations of monomers) were averaged together, the effective stiffness matrix should display the expected continuum-level material symmetry properties; this is the basis of the ergodic hypothesis.

For comparison purposes, the isotropic Young's modulus was calculated for each of the final cured crosslinked VE structures simulated in this study. For example, the Young's moduli for the series of VE resins at a constant 98% conversion cured by multiple chain growth (Method 1) in the smaller repeating unit cell are shown in Table 4.3 for increasing crosslink density. Note that increasing crosslinking density occurred as chain ends were progressively connected. Increasing the matrix's connectivity with more crosslinks enhances its stiffness, with the Young's modulus increasing from 3.95 GPa to 5.79 GPa as 20 chain ends were reduced to two (Figure 4.8). The modulus is still higher (8.98 GPa) at the highest crosslinking density that was simulated (larger unit cell, 98% conversion and two chain ends). The simulated resin with four chain ends, in the larger cell, gave a modulus of 6.90 GPa. This is in close agreement with the modulus of 7.05 GPa predicted for two chain ends in the smaller unit cell, where these two resins have the same density of crosslinks. The simulation cannot mimic the real heterogeneous crosslinked structure of a VE resin, because micron-sized or larger RUCs dimensions or larger would be needed. Computational limitations place this number of atoms/molecules far beyond current MD and computational limitations. However, this study's approach can be used to model various homogeneous microstructure features and properties.

Table 4.3 Young’s modulus of VE resins cured by Methods 1 and 2 to 98% conversion. Effect of crosslink density[a].

Repeating Unit Cell	Curing Method	Chain Ends Present	Young’s Modulus (GPa)
[32.2 Å]^3	1	20	3.95
[32.2 Å]^3	1	16	4.11
[32.2 Å]^3	1	8	4.94
[32.2 Å]^3	1	2	5.79
[32.2 Å]^3	2	2	7.05
[40.6 Å]^3	2[b]	4	6.90
[40.6 Å]^3	2[b]	2	8.98
—	Experiment[b]	—	3.40

[a] The VE resins in this work mimicked those in Derakane 441-400 VE resin. The multiple chain (Method 1) and single chain (Method 2) growth methods used here were performed to the point where the number of chain ends was two. [b]Ashland Co. http://www.derakane.com/derakaneControllerAction.do?methme=showTechnicalsDataSheets (date accessed : October 26, 2011). The lower experimental value is due to the fact that a 98% conversion to equivalent crosslink densities, particularly those represented by two and four chain ends, are not, in general, experimentally achieved.

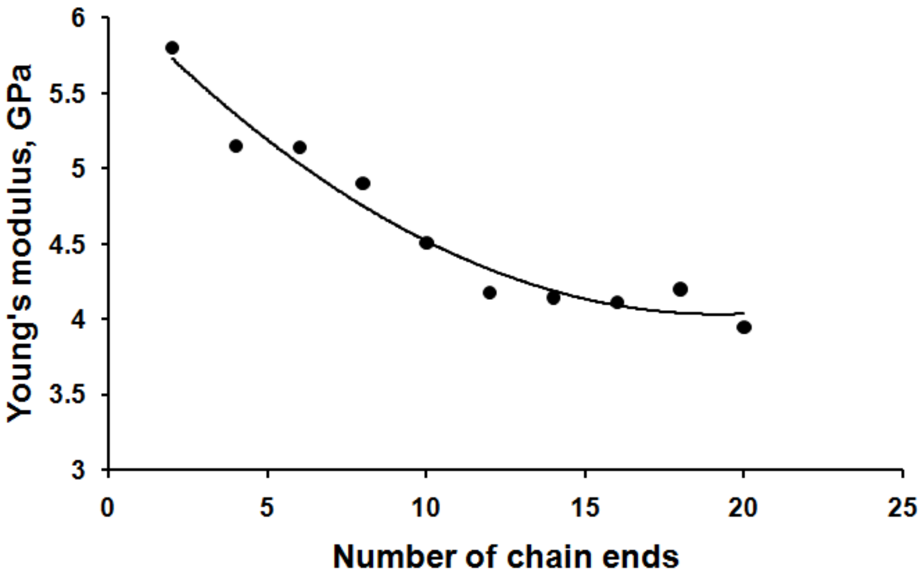

Figure 4.8 Young’s modulus (as function of remaining chain ends from network formation by Method 1.

The Young’s modulus given by the single chain curing method (Method 2) at 98% conversion (7.05 GPa) is about twice as high as the corresponding experimental value in Table 4.3. This single chain cure more closely corresponds to the way a real chain grows during VE curing. This simulation may better represent the formation of a microgel region which has a higher crosslink density, hence modulus, than the average of the entire cured material. The experimental value represents the mechanical response of an entire heterogeneously structured experimental resin. Additionally, the degree of conversion of the experimental resin [Ashland Chemical Co. 2011] was not mentioned. It is very likely less than 98%. Most literature reports [Zhang *et al*., 2007, Yang and Lee 2001, Dua *et al*., 1999] do not give the percentage conversions of the monomers, making comparisons difficult. The degree of the double bond conversion of VE and styrene was reported to be over 90% when a high initial isothermal temperature was used [Yang and

Lee 2001]. Monomer conversions of 90–95% are unlikely to be as highly crosslinked as 98% conversion specimens will be.

The RRV approach to crosslinking improves the predicted chemical structure of the crosslinking network of VEs (or other polymerizing networks where different reactivites and specific regioselectivities should be accounted for). However, while actual cured VE resins appear homogeneous at the macroscale, they are highly heterogeneous when viewed at the nano- or microscale level. VE resin curing mechanisms are complex and usually involve microphase separation during curing.[30] Tiny microgel regions become more highly crosslinked and phase separate. This leads to complex internal diffusion and chemical kinetics that depend on the monomer composition, initiator concentration, and the cure temperature protocol [Ziaee and Palmese 1999, Ganem *et al.*, 1993]. The absolute size of these microphase regions will vary with curing conditions. Whether such regions have dimensions on the order of 10 nm^3 or 1 μm^3, they are large compared to the size of typical periodic cells of MD simulations.

The isothermal cure temperature is known to affect the makeup of both VE microgel regions and the continuous crosslinked matrix in which the more highly crosslinked microgelled regions are bonded. Rey *et al*. [Rey *et al.*, 2000] showed that higher isothermal cure temperatures created smaller microgel structures. Furthermore, Ganglani *et al*. [Ganglani *et al.*, 2002] showed theoretically that networks formed by high temperature initiation had more highly crosslinked matrices between the microgel domains, leading to the greater tensile strength. Finally, all structural features depend on the stoichiometry and structure of the monomers used.

4.6 Conclusions

The relative reactivity volume (RRV) chain growth algorithm was developed for simulating polymerization and resin curing. It accounts for regioselectivity and differences in relative reactivity ratios when more than one monomer is present. This was applied to MD simulations of the curing of the Derakane 441-400 vinyl ester (VE) resin to build up the crosslinked resin network with a chemically realistic microstructure. The networks generated represent a chemically realistic VE homogeneous network structure. It is important to note that this algorithm can be employed for other thermoplastic or thermoset systems and can even be applied to any set of competitive, non-reversible chemical reactions.

The VE networks were constructed by the less computationally intensive use of employing several growing chains followed by progressively linking head-to-tail chain after a desired conversion was reached (Method 1). The more computationally intensive use of a single growing chain (Method 2) was also employed. Glass transition temperatures (T_g) were calculated for resin networks prepared by both methods. T_g values were not sensitive to the crosslink densities over the range studied here. The lack of sensitivity of T_g to crosslink density was consistent with experimental observations of Ziaee *et al*. [Ziaee and Palmese 1999] on VE samples post-cured at the same temperature from two different crosslink densities.

The predicted Young's moduli increased sharply with higher crosslink densities at constant (98%) conversion. The predicted resin density increased with crosslink density at constant conversion. Resin density dropped with increasing temperature but this decrease was less pronounced at high crosslink densities. Young's moduli in these simulations were computed by a static method [Wu and Xu 2006] Young's moduli calculated at 98% conversion and high crosslinking densities were substantially higher (5.79-7.05 GPa) than the reported experimental value of 3.4 GPa and values obtained in our labs (3.76 GPa). This makes sense since the MD simulated structures did not include voids or other defects that would serve to reduce the effective moduli. Furthermore, the 98% conversion and the crosslinking density in our simulated structures are likely higher than those of the experimental samples. Finally, real VE resins are heterogeneous with more highly crosslinked regions formed during initial microgelling, which are dispersed and continuously bonded into a lower crosslink density continuous phase.

Repeating cells containing several hundred or several thousand monomers are likely to generate crosslinked structures which more closely resemble early phase microgelling than simulations of the type performed here. During the MD simulation, the growing chain ~~Sty$^{\bullet}$ or ~~VE$^{\bullet}$ heads are more likely to encounter and react with methacrylate functions of VE monomers that have already been incorporated into the macromolecular network by their other methacrylate function as crosslinking proceeds. This likehood increases as the styrene and VE monomers are increasingly depleted from the MD cell. In an experimental cure, monomers can rapidly diffuse into a very small microgelling region, but this diffusional resistance will grow as the microgel dimensions and crosslinking density increase. Therefore, future VE curing MD simulations should explore larger repeating cells with further increased single chain growth. For example, a 500 or 1000 monomer cell with single chain growth to 70% and 90% could be followed by then initiating a second chain to try for a 95% conversion. The properties of resins simulated by these and related procedures would be of interest to generate a more detailed knowledge of how homogeneous VE crosslinked network structures will affect resin properties. Other simulations of VE cures with different VE monomers and different styrene (or other comonomer) weight fractions will shed further light on VE resin structure versus property relationships now that regiochemistry and reactivity ratios can be accounted for. However, such simulations are presently beyond the capabilities of current computer simulations.

Eventually, chain growth/network formation algorithms will need to account for chain transfer and chain termination events. This is an extremely challenging task since experimental information on these topics inside gelled (and gelling) domains is not available. An immediate application of this chain growth algorithm is to study the copolymerization of two monofunctional monomers with quite different relative reactivity ratios. In such copolymerizations, the initially formed copolymers have a significantly different M_1/M_2 ratio and different triad and tetrad microstructural features due to monomer drift during conversion.

It is currently beyond the capability of MD simulations to capture the effects of discrete domains of different crosslink densities present in experimental VE cured resins at the macroscale. MD simulation can, however, be a tool to study the properties of homogeneous regions of cured VE resins. Once a variety of cured VE phases with both specified crosslink densities and monomer mole ratios have been simulated and their properties predicted, larger scale mechanics calculations can then be made on heterogeneous VE systems by imbedding higher crosslink density microgelled regions into lower crosslinked density continuous regions. However, chemically reasonable MD simulations of each homogeneous region are needed first.

4.7 Acknowledgement

This work was sponsored by the U. S. Department of Energy under contract DE-FC26-06NT42755. We wish to acknowledge William Joost, Department of Energy's technology area development manager, and the Center for Advanced Vehicular Systems (CAVS) at Mississippi State University for their support.

4.8 References

Accelrys Inc, San Diego, CA, USA (Discover module).

Ashland Chemical Co., "Derakane 441-400 Vinyl Ester Resin Property Data Sheet." http://www.ashland.com, 2011.

Bandyopadhyay, A., Valavala, P. K., Clancy, T. C., Wise, K. E., and Odegard, G. M., "Molecular modeling of crosslinked epoxy polymers: The effect of crosslink density on thermomechanical properties", *Polymer*, DOI:10.1016/j.polymer. 2011.03.052

Berendsen, H. J. C., Postma, J. P. M., van Gunsteren, W. F., DiNola, A., and Haak, J. R., "Molecular dynamics with coupling to an external bath", *Journal of Chemical Physics*, 1984, 81, 3684-3690.

Brandrup, J., and Immergu, E. H., Polymer Handbook, 3rd ed., Wiley, New York, 1989, 30-33.

Bunte, S. W., and Sun, H., "Molecular modeling of energetic materials: The parameterization and validation of nitrate esters in the COMPASS force field", *Journal of Physical Chemistry B*, 2000, 104, 2477-2489.

Cao, X., and Lee, L. J., "Control of shrinkage and final conversion of vinyl ester resins cured in low-temperature molding processes", *Journal of Applied Polymer Science*, 2003, 90, 1486-1496.

Doherty, D. C., Holmes, B. N., Leung, P., and Ross, R. B., "Polymerization molecular dynamics simulations. I. Cross-linked atomistic models for poly(methacrylate) networks", *Computational and Theoretical Polymer Science*, 1998, 8, 169-178.

Dua, A., McCullough, R. L., and Palmese, G. R., "Copolymerization kinetics of styrene/vinyl-ester systems: Low temperature reactions", *Polymer Composites*, 1999, 20, 379-391.

Farah, K., Karimi-Varaneh, H. A., Müller-Plathe, F., and Böhm, M. C., "Reactivity molecular dynamics with material-specific coarse-graining potentials: growth of polystyrene chains form styrene monomers", *The Journal of Physical Chemistry B*, 2010, 114, 13656-13666.

Feraboli, P., Gasco, F., Wade, B., Maier, S., Kwan, R., Masini, A., Deoto, L., and Reggiani, M., "Lamborgini "Forged Composite" technology", ASC 26th Technical Conference/Second Joint US-Canada Conference on Composites (Montreal, Canada) 2011; 1012.

Frankland, S. J. V., Harik, V. M., Odegard, G. M., Brenner, D. W., and Gates, T. S., "The stress-strain behavior of polymer-nanotube composites from molecular dynamics simulation", *Composite Science and Technology*, 2003, 63, 1655-1661.

Ganem, M., Mortaigne, B., Bellenger, V., and Verdu, J., "Influence of the styrene ratio on the copolymerization kinetics of dimethacrylate of diglycidyl ether of bisphenol a vinylester resins crosslinked with styrene", *Journal of Macromolecular Science: Pure Applied Chemistry A*, 1993, 30, 829-848.

Ganglani, M., Carr, S. H., and Torkelson, J. M., "Influence of cure via network structure on mechanical properties of a free-radical polymerizing thermoset", *Polymer*, 2002, 43, 2747-2760.

Guo, Z., Liang, S. X., Pereira, T., Scaffaro, R., and Hahn, H. T., "CuO nanoparticle reinforced vinyl-ster resin nanocomposites: Fabrication, characterization and property analysis", *Composite Science and Technology*, 2007, 67, 2036-2044.

Hill, R., "Elastic properties of reinforced solids: Some theoretical principles", *Journal of the Mechanics and Physics of Solids*, 1963, 11, 357-372.

Jang, C., Nouranian, S., Lacy, T. E., Gwaltney, S. R., Toghiani, Hossein., and Pittman Jr C. U., "Molecular dynamics simulations of oxidized vapor-grown carbon nanofiber surface interactions with vinyl ester resin monomers", *Carbon*, DOI:10.1016/j.carbon.2011.09.013.

Leung, Y. –K., and Eichinger, B. E., "Computer simulation of end-linked elastomers, Parts 1 and 2", *Journal of Chemical Physics*, 1984, 80, 3877-3884.

Li, H. "Synthesis, characterization and properties of vinyl ester matrix resins", PhD dissertation. Blacksburg, VA, USA: Virginia Polytechnic Institute and State Univ.; 1998.

Liu, H., Li, M., Lu, Z. –Y., Zhang, Z. –G., Sun, C. –C., and Cui, T., "Multiscale simulation study on the curing reaction and the network structure in a typical epoxy system", *Macromolecules*, 2011;DOI:dx.doi.org/10.1021/ma201390k.

Karbhari, V. M., "E-glass/vinylester composites in aqueous environments: Effects on short-beam shear strength", *Journal of Composites for Construction*, 2004, 8, 148-156.

Madruga, E. L., San Roman, J., and Del Puerto, M. A., "Radical copolymerization of acrylic monomers. II. Effect of solvent on radical copolymerization of methyl methacrylate and styrene", *Journal of Macromolecular Science: Chemistry*, 1979, 13, 1105-1115.

McConnell, V. P., *Reinforced Plastics*, "Vinyl esters get radical in composite markets", 2010, 54, 34-38.

McQuaid, M. J., Sun, H., and Rigby, D., "Development and validation of COMPASS force field parameters for molecules with aliphatic azide chains", *Journal of Computational Chemistry*, 2004, 25, 61-71.

Nouranian, S., Jang, C., Lacy, T. E., Gwaltney, S. R., Toghiani, Hossein., and Pittman Jr C. U.," Molecular dynamics simulations of vinyl ester resin monomer interactions with a pristine vapor-grown carbon nanofiber and their implications for composite interphase formation", *Carbon*, 2011, 49, 3219-3232.

Odian, G., Principles of Polymerization, 2nd ed., John Wiley & Sons, New York, 1981, 181-195.

Qi, D., Hinkley, J., and He, G., "Molecular dynamics simulation of thermal and mechanical properties of polyimide-carbon-nanotube composites", *Modelling and Simulation in Materials Science and Engineering*, 2005, 13, 493-507.

Rey, L., Galy, J., and Sautereau, H., "Reaction kinetics and morphological changes during isothermal cure of vinyl/dimethacrylate networks", *Macromolecules*, 2000, 33, 6780-6786.

Rigby, D., Sun, H., and Eichinger, B. E., "Computer simulations of poly(ethylene oxide): Forcefield, PVT diagram and cyclization behavior", *Polymer International*, 1997, 44, 311-330.

Sun, H., "An ab initio forcefield optimized for condensed-phase application-overview with details on alkane and benzene compounds", *The Journal of Physical Chemistry B*, 1998, 102, 7338-7364.

Varshney, V., Patnaik, S. S., Roy, A. K., and Farmer, B. L., "A molecular dynamics study of epoxy-based networks: Cross-linking procedure and prediction of molecular and material properties", *Macromolecules*, 2008, 41, 6837-6842.

Watt, S. W., Chisholm, J. A., Jones, W., and Motherwell, S., "A molecular dynamics simulation of the melting points and glass transition temperature of myo- and neo-inositol", *Journal of Chemical Physics*, 2004, 121, 9565-9573.

Wu, C. F., and Xu, W. J., "Atomistic molecular modeling of crosslinked epoxy resin", *Polymer*, 2006, 47, 6004-6009.

Yang, H., and Lee, J., "A kinetic model for free-radical crosslinking co-polymerization of styrene/vinylester resin", *Polymer Composites*, 2001, 22, 668-679.

Zhang, J., Liang, Y., Yan, J., Lou, J., “Study of the molecular weight dependence of glass transition temperature for amorphous poly(L-lactide) by molecular dynamics simulation”, *Polymer*, 2007, 48, 4900-4905.

Zhao, L., Liu, J., and Sun, H., “Semi-ionic model for metal oxides and their interfaces with organic molecules”, *Journal of Physical Chemistry C*, 2007, 111, 10610-10617.

Zhu, J., Imam, A., Crane, R., Lozano, K., Khabashesku, V. N., and Barrera, E. V., “Processing a glass fiber reinforced vinyl ester composite with nanotube enhancement of interlaminar shear strength”, C*omposite Science of Technology*, 2007, 67, 1509-1571.

Ziaee, S., and Palmese, G. R., “Effects of temperature on cure kinetics and mechanical properties of vinyl-ester resins”, *Journal of Polymer Science Part B: Polymer Physics*, 1999,37, 752-744.

CHAPTER 5

CONCLUSIONS AND RECOMMENDATIONS FOR FUTURE WORK

5.1 Conclusions

A series of molecular dynamics simulations were performed to investigate the liquid vinyl ester (VE) resin monomer interactions with the surface of pristine and oxidized vapor-grown carbon nanofiber (VGCNFs). These interactions may influence the formation of an interphase region during resin curing. At system equilibrium, the styrene/VE monomer ratio was higher in about a 5 Å thick region adjacent to the pristine nanofiber surface than in the remaining liquid volume. The elevated concentration of styrene near the nanofiber surface suggests that a very thin styrene-rich interphase region could be formed upon curing with a different crosslink density than the bulk matrix. Furthermore, styrene accumulation in the immediate vicinity of the nanofiber surface might, after curing, improve the nanofiber-matrix interfacial adhesion compared to the case where the monomers were uniformly distributed throughout the matrix.

For oxidized VGCNF-liquid VE monomer interfacial interactions, the concentrations of the most hydrophobic constituent (styrene) and the most polar one (VE1) were both enhanced near the oxidized graphene surface. The monomer compositions near the oxidized VGCNF surfaces were different than for the pristine (unoxidized) graphene surface. This suggests that the oxidized VGCNF surfaces would result in different interfacial adhesive bonding for the cured resin than for pristine nanofiber surfaces. Increased polar interactions promote higher interfacial adhesion between the matrix and the oxidized VGCNF surfaces than for the pristine VGCNF surfaces. This could increase the interfacial shear strength compared to that for a pristine VGCNF, where only nonpolar matrix-carbon nanofiber interactions are present.

The VE crosslinking MD simulations were performed to investigate the thermal and mechanical properties at the neat resin. The real VE free radical curing mechanism for monomer mixtures is very complex because it forms microgelled regions leading to a resin that is inhomogeneous at the microscale while appearing homogeneous at the macroscale. It is currently beyond the capability of MD simulations to capture the effects of discrete material structures in cured VE resins due to computational limitations on the tractable system size. The reactive volume chain growth algorithm developed in this study included the key features accounting for regioselectivity (head-to-tail chain growth) and differences in the relative reactivity ratios when more than one monomer is present. This allows one to investigate fundamental aspects of homogeneous regions of a cured VE resin.

The technique for pre-equilibrating monomer mixtures before resin crosslinking can be extended to any specific surface (functionalized or not). MD simulations utilizing this technique will provide insight into the design of nanoreinforcement/matrix interfaces with improved adhesion. This work emphasizes the important concept that liquid structure is sensitive to an interface only very close to that interface.

Two crosslinking methods were introduced and compared. The first method is intentionally initiated several growing chains whereas the second method used a growing single chain. Crosslinking simulations using both techniques were performed until 98% conversion was reached. Highly crosslinked VE networks with conversions up to 98% were successfully achieved. When crosslinked structures were created, the volume shrinkage, glass transition temperatures, and Young's moduli were determined.

Volume shrinkage occurs during the resin curing. The volume shrinkages calculated here for the Method1 (7.8%) and the Method2 (8.8%) were each higher than the experimental value for Derakane 441-400 vinyl ester resin (7.5%) [Ashland Chemical Co. 2011]. This difference is likely because the real cured samples contain some voids and defect sites. In addition, the experimental curing will not reach 98% conversion. Furthermore, the absolute crosslink density of the experimental cure is not known. Note that only 3500 atoms cannot mimic the overall VE heterogeneous scale size of the cured regions with different properties as exists in real VE systems. The computed crosslinked structure here may represent homogeneous regions within the real cured system. Such microgelled regions can be highly crosslinked since only two chain ends remained in the computed structures. The author suggests other approaches for further studies. The crosslinking process could be performed many times with different initial random monomer packings with the same density, by starting the growing chains at different locations, and employing far more monomers in the repeating cell.

The calculated glass transition temperatures (420-426K), while not sensitive to the range of crosslink densities studied here, were clearly dependent on the degree of the conversion. This is consistent with the experimental observations of Ziaee et al. [Ziaee and Palmese, 1999] in which the glass transition temperatures are more related to the degree of conversion than the crosslinked densities. The desired degree of the conversion can be obtained and controlled by the post-curing temperature but the actual crosslink densities of the cured VE resin are not known.

The Young's moduli were obtained using a static method based on MD [Wu and Xu, 2006]. The obtained micropolar elastic stiffness matrix was neither positive definite nor symmetric. The periodic repeating unit cell (RUC) used in MD does not correspond to a representative volume element (RVE) used in the standard continuum mechanics. Hence, the calculated stiffness matrix will only loosely approximate isotropic bulk material behavior.

5.2 Recommendations for Future Work

In the future, a number of MD simulations will be performed to better understand the interactions between VGCNFs (pristine and oxidized) and liquid VE resins before curing and to investigate the crosslinked network formation and the mechanical properties of the VGCNFs/VE system after curing. Furthermore, the graphene sheet pullout simulations will be performed to investigate the interfacial shear strength of graphene/VE system. Several of these are described below.

5.2.1 Idealized Carbon Nanofiber Surface – 1

A group of two graphene layers may be created to separate the liquid monomer molecules on either side of these graphene sheets by a distance that is great enough such that no cross-sheet monomer-monomer interactions can occur. The separation distance between the graphene layers is selected to exceed the Van der Waals cutoff distance of 9.5Å. This geometry eliminates the liquid resin monomer interactions through the idealized nanofiber surface, i.e., the monomer-monomer interaction only occur on one side of the carbon nanofiber surface. The layers can still be constructed in shingled form in a 60×80×60 Å^3 RUC as shown in Figure 5.1.

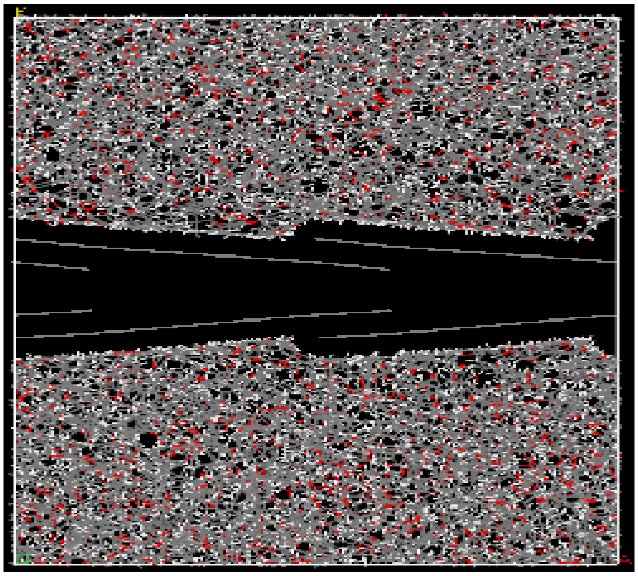

Figure 5.1 Two group graphene layers are created to avoid the interactions of monomers through the graphene layers. Monomers can only interact with the side of VGCNF surfaces.

5.2.2 Idealized Carbon Nanofiber Surface – 2

The three parallel graphene layers may also be modeled in a 60×100×60 Å^3 RUC as shown in the Figure 5.2. This simulation also avoids the cross interaction of monomers through the graphene layers. Furthermore, it allows the underlying (middle) graphene sheet to interact with the monomers and the surface sheet. Such interactions are secondary but experimentally they are known to exist. Monomers can only interact with the side of graphene layers where they are located. The total number of atoms is about 35,000 as shown in the Figure 5.2.

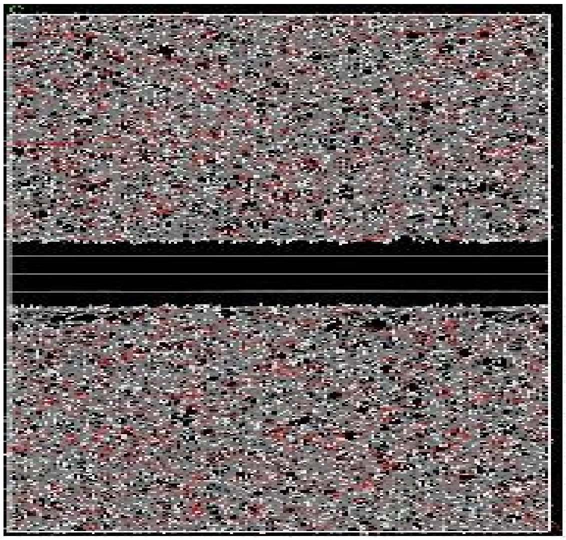

Figure 5.2 The infinite three graphene layers in 3-dimensions are created. The closest distance of monomers through the graphene layers is ~10 Å to avoid the cross monomer interactions through the graphene layers.

5.2.3 Nanofiber Pullout Simulations

After crosslinking these VE resins using the new algorithm, both pristine and oxidized carbon nanofiber graphene sheet pull-out simulations will be performed to assess interfacial shear strength (IFSS). Since VEs have both polar and nonpolar interactions, it is not clear if the IFSS will be higher with pristine or oxidized surfaces. By constructing crosslinked resins reflecting the monomer mole ratios found in the liquid resins after equilibration with the graphene surfaces, we expect each of these two surfaces to have favorable adhesive interactions (π-π stacking and classic van der Waals interactions with more styrene at the pristine surfaces but more H-bonding, dipole-dipole and instantaneous dipole-induced dipole attractions with oxidized sheets).

5.2.4 Final Comments

In future simulations, the morphology and structure of VGCNFs/liquid VE resin systems can be understood by using more realistic equilibrated models involving significantly larger numbers of degrees-of-freedom (more molecules, liquid/liquid and liquid/solid). In addition, by accounting for regionselectivity (head-to-tail chain reaction), monomer reactivity ratios, and other key aspects of polymer chemistry, more physically realistic simulation of the real resin curing process will be obtained. The predicted interphases and IFSS developed in this work can be used to determine material manufacturing process that lead to better mechanical properties of VGCNF/VE composites. Calculated VGCNF/VE interphase properties can feed directly into higher length scale calculations within a multiscale analysis framework. In essence, some fine-scale experiments can be replaced by carefully formulated MD simulations. Establishment of the crosslink network and interphase formation in VGCNF/VE composite systems using MD simulations has not been previously addressed. Moreover, most studies of nanoreinforced thermoset composite systems do not consider the monomer-monomer and nanoreinforcements-monomer interactions prior to curing. Such interactions can lead to a gradient in the different monomer mole ratios. If these gradients are captured during curing, they can arguably affect both fiber-matrix interfacial properties and composite strengths. Therefore, this work represents an important first step in the establishment of a multiscale analysis framework that accounts for the effect of realistic morphologies, relating reactivities and region-chemistry at the molecular level on nanocomposite behavior.

5.3 References

Ashland Chemical Co., “Derakane 441-400 Vinyl Ester Resin Property Data Sheet.” http://www.ashland.com, 2011.

Wu, C. F., and Xu, W. J., “Atomistic molecular modeling of crosslinked epoxy resin”, *Polymer*, 2006, 47, 6004-6009.

Ziaee, S., and Palmese, G. R., “Effects of temperature on cure kinetics and mechanical properties of vinyl-ester resins”, *Journal of Polymer Science Part B: Polymer Physics*, 1999, 37, 752-744.